BUILDING THEORETICAL FRAMEWORKS TO INTERPRET THE DYNAMICS OF LOW-MASS AND HIGH-MASS GALAXY PAIRS ACROSS COSMIC TIME

by

Katherine N. Chamberlain

A Dissertation Submitted to the Faculty of the

DEPARTMENT OF ASTRONOMY

In Partial Fulfillment of the Requirements

For the Degree of

DOCTOR OF PHILOSOPHY

WITH A MAJOR IN ASTRONOMY AND ASTROPHYSICS

In the Graduate College

THE UNIVERSITY OF ARIZONA

2024

THE UNIVERSITY OF ARIZONA
GRADUATE COLLEGE

As members of the Dissertation Committee, we certify that we have read the dissertation prepared by: Katherine N. Chamberlain

titled: Building Theoretical Frameworks to Interpret the Dynamics of Low-mass and High-mass Galaxy Pairs Across Cosmic Time

and recommend that it be accepted as fulfilling the dissertation requirement for the Degree of Doctor of Philosophy.

_____
Gurtina Besla (Apr 16, 2024 17:47 PDT)
Gurtina Besla   Date: Apr 16, 2024

_____
Daniel Stark (Apr 25, 2024 14:43 PDT)
Daniel Stark   Date: Apr 25, 2024

_____
Peter Behroozi (Apr 17, 2024 09:50 GMT+9)
Peter Behroozi   Date: Apr 17, 2024

_____
Kathryne Daniel   Date: Apr 16, 2024

_____
Benjamin Weiner   Date: Apr 17, 2024

Final approval and acceptance of this dissertation is contingent upon the candidate's submission of the final copies of the dissertation to the Graduate College.

I hereby certify that I have read this dissertation prepared under my direction and recommend that it be accepted as fulfilling the dissertation requirement.

_____
Gurtina Besla (Apr 16, 2024 17:47 PDT)
Gurtina Besla   Date: Apr 16, 2024
Astronomy

ACKNOWLEDGMENTS

They say it takes a village to raise a child. In my case, it took a village to raise this PhD Dissertation. This was a challenging journey that I truly could not have succeeded in without the tremendous support of many of my loved ones.

To start, I'd like to thank my family, who have supported me since before I was born. Mom, your unyielding, unrelenting, sometimes overwhelming support and belief in me carried me through many moments of self-doubt and struggle. I will always remember your words: "You've been through more challenging things before, you'll get through this too." You wouldn't believe how often I return to these words when I need help remembering that I am strong and capable. Dad, your quiet but sturdy and foundational support has never wavered, and I have always felt like you fully believed in me to follow through on my pursuits and dreams. Thank you for giving me a sense of wonder and for spending so much time with me surrounded by nature. Some of my most formative memories, from childhood through adulthood, were formed during our backpacking trek and yearly Yellowstone visits, and I'll cherish them forever. Jace, thank you too for always believing in me, and for, on occasion, nailing my feet back down to the ground and giving me a sense of perspective again. I love you bunches.

To my love, Daniel Truong. One hundred, no, one thousand "thank you"s wouldn't feel like enough. Your patience, guidance, and compassion have been invaluable to me over the last three years, and I will be eternally grateful for you, forever and ever. Thank you for literally keeping me fed and clean-clothed while I finished this arduous journey. Thank you even more for being the person I share so much of my life with. I can't wait to explore the world with you by my side, and to share our futures and find happiness together. I love you more.

To the friends I've made in Tucson, thank you for being the shining stars in my desert sky. Thank you over and over and over and over again to Rachael Amaro for being the cwaziest,

most predictable, most ride-or-die, most fun and bubbly best friend I could have asked for to go through grad school together. I do not exaggerate when I say I could not have done this without you. You helped haul me over the finish line in every race when I tripped and stumbled. Your faith in me was often stronger than my own faith in myself, and I will owe you for that forever. Literally don't know how to compress all of my feelings for our most memorable memories, funnest facts, and audacious adventures into a document that's shorter than the remainder of this dissertation, and I'm getting weepy, so instead I'll say this: 가 자! Charity Woodrum, you are power incarnate and just like the wind, only with a terrible sense of direction. Thank you for your late night thoughts, your undeniable love and support, and for sharing your truly non-inspiring totally normal life with me. I feel honored to know someone like you, and literally still wonder how you can come this far and still want to go even further. I can't wait to stand with you on your next journey wherever it goes, and to see how much you change the world. Raphael Hviding, thanks for being the most chaotic roommate I've ever had, and for being the #1 party-hoster at Steward. You are probably the reason I got through the first few years of the pandemic without forgetting how to converse with other people. Hope you thrive forever. Maria Pudoka, you showed up late in my grad school game, but I wouldn't trade our friendship for anything. Thanks for doing art with me on nights when I couldn't even brush my hair and couldn't talk about anything other than my most current gaming obsessions. You inspire me to cry more :). Samantha Scibelli, thank you for being you, for being so glittery and poppy and pink and YOU and for being such a good friend. I've missed you so much this last year. Tucson felt a lot more lonely without you and your infectious laugh.

I'd also like to shout loud and unapologetic thank you's to a bunch of people I met during my grad school career who mean the entire world to me: Lily Whitler (my wonderful creative friend, I love you oodles), Jasmin Washington (thank you for being my tattoo sibling!!), Haowen Zhang (photographer extraordinaire), Fengwu Sun, Matthew Murphy, Spencer Scott, Collin Christy, Fuda Nguyen, and to the BADS students (shout out to Elise Darragh-Ford, Maddie Lucey, Micah Oeur, Anna Parul, and Alex Riley for being the bestest funnest friends a girl alone in NYC could ever have). Finally, thank you to all my Tucson animal friends: OG Bug (RIP), On-Bon, Tabitha, Pepper, Kota, and to Daniel's and my precious boys Yang

and Dang, who step on me 13 times each morning to make sure I'm not still sleeping before my alarm even goes off.

To my non-academic-affiliated friends all over the country, thank you all so much for your endless support and for being my hype squad in a way I didn't know was possible. Katelyn Farrier (Owolabi? omg!), my long lost big sister (sorry Amelia, you're gonna have to share), you were the best roommate I could have possibly asked for in undergrad. Thank you so so much for all of the fun we had, and for being my #1. If I could relive our year together again, I'd do it 100 times over. You're truly a ray of sunshine. I miss you every day of the year! To Sara Lewis, thank god I have a friend like you. Someone so nurturing, caring, encouraging, and sympathetic like you deserves the whole wide world, and I've been aiming to give that to you for years. I hope I get to follow through on that some day! Alex Terrio, my precious gemstone. Thank you so much for your friendship. Truly, you are such a wonderful person and I could not be happier or prouder to call you my friend. I can't wait to visit you again, and to go on adventures together when we both have the budget some day!! Thank you for always making me feel special and loved.

I'd also like to thank my research group and the people who have guided me and provided their incredible mentorship that helped me learn and grow more than I was probably comfortable with at first, but am now extremely grateful for. Gurtina Besla, thank you for giving me a space in your group to develop, learn, and grow over the past six years. I have learned unforgettable lessons through conversations about justice and equity with you and the rest of our group, and I couldn't be more grateful all of the opportunities that you sent my way and helped me achieve. Thank you as well for putting together a research group that is truly compassionate, kind, and supportive of one another, and for involving me in the transformative space of the Astronomical Intelligence community. Finally, thank you for supporting me through my transition out of astronomy. You have taught me so much about how to champion my knowledge and experience and to not be afraid to just try. To Ekta Patel, my graduate big sister, I'm eternally grateful for your hands-on guidance and support through the years, and also for your friendship which has helped me through more challenging times than I care to count. It was an honor to follow in your footsteps in the Besla Group, and I couldn't be prouder of what you've achieved. I truly believe you are a

superstar, even when you don't feel it. Thank you for being my sounding board, the wind in my sails, and my dear dear friend. Nico Garavito-Camargo, my graduate big brother, thank you for your friendship and mentorship throughout the last six years. You were a daunting act to follow in our research group, with your epic thesis and groundbreaking work, but it was amazing getting to see you grow and become such an influential researcher and prominent name in our subfield. Thank you for always checking in to see how I'm doing, and for being such a wonderful friend and person. Hayden Foote and Himansh Rathore, thank you for being wonderful additions to the Besla team during my time here. You both helped me learn how to fill the role of a mentor, and how much mentors can also learn from their mentees. It was a joy getting to experience your tremendous growth as researchers and people these past few years! Finally, thank you also to my formal and informal mentors. Adrian Price-Whelan, you taught me more about coding than I thought a person could learn in two months. Your mentorship style left me feeling extremely capable and prepared for my future endeavors, and revived a sense of curiosity for astronomy in me that I thought I'd irrecoverably lost. Thank you also to the other mentors at the BADS summer school, particularly to Emily Cunningham, Sarah Pearson, Jason Hunt, and Robyn Sanderson, and to my collaborators for your kind words, feedback, support, and mentorship, particularly to Vicente Rodriguez-Gomez, Paul Torrey, Garreth Martin, Sabrina Stierwalt, and Kelsey Johnson.

Finally, to some people I've never met but that have recently had a profound impact on my life. Thank you to Furudate Haruichi for writing the world's best manga. Haikyuu will undoubtedly stay in my heart forever. To Stray Kids, thank you for pouring your hearts and souls into your music and performances. You've deeply touched my life with your sound and endless pursuit of your dreams. You have been a source of inspiration for me in times that would have otherwise been colorless and dim. #stay

LAND ACKNOWLEDGMENT

We respectfully acknowledge the University of Arizona is on the land and territories of Indigenous peoples. Today, Arizona is home to 22 federally recognized tribes, with Tucson being home to the O'odham and the Yaqui. Committed to diversity and inclusion, the University strives to build sustainable relationships with sovereign Native Nations and Indigenous communities through education offerings, partnerships, and community service.

DEDICATION

To my friends, my family, and my love for supporting me during this journey, and to myself for never giving up.

TABLE OF CONTENTS

LIST OF FIGURES

LIST OF TABLES

ABSTRACT

Galaxy interactions and mergers help drive galaxy evolution by triggering starbursts, AGN activity, and morphological changes. Understanding the frequency and dynamics of interacting galaxy pairs across cosmic time is thus necessary to quantify their importance for galaxy evolution and for testing predictions of hierarchical assembly in a ΛCDM paradigm. At low redshift, the Local Group (LG) is a great testbed for galaxy dynamics studies as it hosts several galaxy pairs, including major pairs (mass ratio $> 1 : 4$, e.g., Milky Way (MW)–M31) and minor pairs ($1 : 4 >$ mass ratio $> 1 : 10$, e.g., MW–LMC, M31–M33, and LMC–SMC). High-precision observational data have facilitated tight constraints on measurements of the 6D phase-space information (distance, line of sight velocity, and proper motions) for several LG pairs, which in turn has permitted detailed studies of their orbital histories and dynamics. However, it is still unclear how to place LG pairs in a cosmological context in terms of their mass and dynamics and how to connect the evolution of LG pairs across redshift with expectations from ΛCDM.

In this dissertation, I study the dynamics of galaxy pairs to develop a deeper understanding of the LG and how observations and simulations can be integrated to study these types of systems at redshifts $z = 0 - 4$. First, I study the impact of the disequilibrium state of the MW on dynamical mass measurements of the Local Group, and use the first measurements of the MW disk travel velocity to show that perturbations to the MW lead to inflated mass estimations in frameworks that do not account for perturbations. With updated mass measurements of the LG, I then use the Illustris TNG100 simulation to study the evolution of LG pairs in a cosmological context in terms of their mass and dynamics as a function of redshift. I start by studying the redshift evolution of pair fractions of isolated low-mass ($10^8 < M_* < 5 \times 10^9 \, \mathrm{M_\odot}$) and high-mass ($5 \times 10^9 < M_* < 10^{11} \, \mathrm{M_\odot}$) pairs between $z = 0 - 4$, and find that the frequency of low-mass major and minor pairs is considerably lower than

high-mass major and minor pairs at low redshift. I also show that MW–LMC-mass analogs are most common at $z = 0$, but that MW–LMC-mass analogs that also match the observed kinematic properties of the real MW–LMC system (i.e. have small separations and high velocities) are 2-3 times more common at redshift $z \sim 2$. Additionally, LMC–SMC-mass pairs are 3 times more common at $z > 2$ than at $z = 0$. Further, I develop a framework for pair selection criteria that permits self-consistent studies of pair fractions across mass scales and cosmic time. I show that traditional physical-separation selection criteria yield biased measurements of the pair fraction evolution of galaxy pairs. I then extend this framework by calculating the orbits of these low-mass and high-mass pairs out to $z = 6$, and show that low-mass and high-mass major pairs have identical merger timescales only when pairs are selected via separation criteria that vary with mass and redshift. These frameworks will help facilitate interpretations of the dynamics of low-mass and high-mass galaxy pairs, both in the Local Group and across cosmic time, in the coming era of more precise, deeper, and wider observational programs permitted by *Gaia*, *JWST*, *Roman Space Telescope*, and the Rubin Observatory.

Chapter 1

Introduction

Galaxy interactions and mergers help drive galaxy evolution by triggering starbursts, AGN activity, and morphological changes. Understanding the frequency and dynamics of interacting galaxy pairs across cosmic time is thus necessary to quantify their importance for galaxy evolution and for testing predictions of hierarchical assembly in a ΛCDM paradigm.

1.1 The Local Group

The Local Group (LG) is a galaxy group consisting of two massive galaxies, the Milky Way (MW) and Andromeda Galaxy (M31), and a number of smaller satellite galaxies that orbit them. The MW and M31 have stellar masses of $5 \times 10^{10} \, \mathrm{M_\odot}$ (Flynn et al., 2006; Licquia and Newman, 2015; Bland-Hawthorn and Gerhard, 2016) and $1 \times 10^{11} \, \mathrm{M_\odot}$ (Barmby et al., 2006; Geehan et al., 2006; Tamm et al., 2012; Sick et al., 2015) respectively. The two largest satellites of the MW are the dwarf galaxies Nubecula Major (LMC) and Nubecula Minor (SMC), which have stellar masses of $\sim 3 \times 10^9 \, \mathrm{M_\odot}$ and $\sim 3 \times 10^8 \, \mathrm{M_\odot}$ (Besla, 2015), and are jointly called the MCs. Similarly, M31 has an accompanying large satellite galaxy named M33, with stellar mass $\sim 3 \times 10^9 \, \mathrm{M_\odot}$ (van der Marel et al., 2012b).

1.1.1 Dynamical Studies in the Local Group

The proximity of galaxies in the LG ($\lesssim 1 \, \mathrm{Mpc}$) makes it an excellent test bed for cosmological and galaxy studies. For example, modelling the dynamical history of a galaxy requires the use of 6D phase-space information (i.e., position, line of sight velocity, and proper motions) to construct accurate orbital models. Recent high-precision studies have transformed LG science, with observations from HST and Gaia providing unparalleled precision on the distances and

proper motions of many LG galaxies, including the LMC and SMC, M31, and M33 (Kallivayalil et al., 2006a,b; Sohn et al., 2012; van der Marel et al., 2012b,a; Kallivayalil et al., 2013; Sohn et al., 2017; van der Marel et al., 2019; Sohn et al., 2020). These high-precision observational data have since enabled detailed studies of the dynamics of galaxies in the LG.

High-precision constraints on the proper motions of the LMC and SMC from Kallivayalil et al. (2006a,b) enabled the first high-fidelity orbital reconstruction of the interaction of the MCs, revealing that they were likely on their first infall into the halo of the MW (Besla et al., 2007; Besla et al., 2010). The first proper motion measurements of M31 from HST (Sohn et al., 2012) showed that the MW—M31 orbit is almost entirely radial. Additionally, M33 has been shown to likely be on first infall into the halo of M31 (see e.g., Patel et al., 2017a).

Orbital studies have also facilitated improvements on constraints of the masses of many LG members, and on the mass of the LG itself. For example, Patel et al. (2017a,b) place constraints on the orbits of the LMC and M33, and use information about the orbits (including positions, velocities, and orbital angular momenta) to constrain the masses of the MW and M31. In Patel and Mandel (2023), they extend these methods to utilize the updated proper motions, distances, and line-of-sight velocities of four M31 satellites to place tighter constraints on the virial mass of M31, finding that M31 is likely to have a much higher total mass ($\sim 3 \times 10^{12} \, M_\odot$) than previously expected.

The mass of the LG can also be estimated using the relative dynamics of the MW and M31. One such technique, called the Timing Argument, assumes that the MW–M31 orbit is approximately Newtonian and calibrates the mass of the LG necessary to maintain a bound orbit (see Ch. 2 for more specific details). The first Timing Argument calculation of the LG mass was presented in Kahn and Woltjer (1959), decades prior to the first measurement of M31's proper motion (Sohn et al., 2012). In Kahn and Woltjer (1959), the relative motion of M31 was taken to be the line-of-sight radial velocity only, and assumed that satellite galaxies contributed insignificantly to the mass budget of the LG. They found a LG mass that far exceeded the combined mass of the MW and M31, which they attributed to undetected intergalactic hydrogen gas.

After the first proper motion measurements of M31 with HST, van der Marel et al. (2012b) placed updated constraints on the LG mass by including M31 proper motion measurements

in the Timing Argument calculation. Peñarrubia et al. (2016) took the Timing Argument a step further, showing that the inferred mass of the LG changes if you consider a massive LMC ($\sim 10\%$ of the total mass of the MW; this will be discussed further in the following subsection), and that M31 is orbiting about the MW–LMC barycenter rather than the center of the MW halo. They find that the LG mass inferred via the Timing Argument decreases when the LMC is included in the model. In Ch. 2, I extend upon these studies and introduce a framework to account for the dynamical impact of the LMC on the MW halo (also discussed in further detail in the following subsection) in Timing Argument studies.

As a whole, studies that have so far been permitted by advances in high-precision, long-baseline observations of the LG with HST, GAIA, and soon JWST, illuminate the importance of studying the LG from a dynamical perspective. With these robust dynamical studies of the LG, we can unveil the masses and merger histories of the MW and M31, and determine the role of their massive satellites in shaping these galaxies into what we observe today. Without this dynamical perspective, interpretations of the accretion history, evolution, and fate of LG galaxies would be incomplete.

1.1.2 Dynamical Influence of Low-mass Systems

Despite having been neglected in early LG studies, low-mass galaxies ($M_* \lesssim 10^{10}\,\mathrm{M_\odot}$) of the LG significantly impact dynamical studies of their more massive companions the MW and M31. A massive LMC is likely (abundance matching ascribes a halo mass of $\sim 1-2 \times 10^{11}\,\mathrm{M_\odot}$ for a stellar mass of $3 \times 10^9\,\mathrm{M_\odot}$ at $z = 0$; see e.g. Moster et al., 2013; Behroozi et al., 2013), with many studies showing a massive LMC is even *necessary* for a bound SMC (Kallivayalil et al., 2013) and to match cosmological expectations (Patel et al., 2017b). M33 has also been found to have a total mass exceeding $1 \times 10^{11}\,\mathrm{M_\odot}$ (van der Marel et al., 2012b; Patel et al., 2017a).

Dynamical consequences of a large LMC are reflected in the motions of stellar streams in the MW halo (see e.g., Vera-Ciro and Helmi, 2013; Shipp et al., 2019; Lilleengen et al., 2023). In fact, some studies have used the proper motions of stars in distant stellar streams to constrain the mass of the LMC (Erkal et al., 2018, 2019; Shipp et al., 2021; Koposov et al., 2023).

Perhaps even more interestingly, high-resolution n-body and hydrodynamic simulations have found that interactions with the LMC have caused perturbations in the MW's dark matter halo and stellar disk (Laporte et al., 2018a,b; Garavito-Camargo et al., 2019). These effects have been confirmed observationally via observations of stars in the outer halo ($r_{\rm sep} > 30$ kpc) (Conroy et al., 2021; Erkal et al., 2021). Studies have also shown that the passage of the LMC about the MW should induce a reflex motion of the MW's stellar disk (Gómez et al., 2015; Cunningham et al., 2020; Petersen and Peñarrubia, 2020; Garavito-Camargo et al., 2021). In particular, the velocity displacement of the MW stellar disk from the center of mass of the MW halo was first measured in Petersen and Peñarrubia (2021). They found that the stellar disk of the MW is moving with a 'travel velocity' of ~ 32km s^{-1} with respect to stellar tracers in the outer halo ($40 - 120$ kpc). The direction of this velocity boost is consistent with the orbital trajectory of the LMC, in particular pointing to a location along the path where the LMC was at some point in the past, and is also roughly in the direction of M31.

A MW disk travel velocity has important implications for dynamical studies of the LG. For example, the relative kinematics of M31 have been used to place constraints on the mass of the LG, but such studies have not accounted for the motion of the MW disk in dynamical measurements of M31 as it is being displaced from the center of motion of its dark matter halo. In Chapter 2, I explore the impact of the now measured travel velocity on the assumed MW–M31 orbit, and show that our model points to a less eccentric MW–M31 than in models that do not include a MW travel velocity (van der Marel et al., 2012b; Salomon et al., 2021). This may be good news for those who hope to show that the LG is in fact cosmologically typical in a ΛCDM cosmology, since studies of LG analogs in n-body cosmological simulations find that LG analogs are not likely to have completely radial orbits (Forero-Romero et al., 2013).

1.1.3 LG Analogs in Observations

Our understanding of the LG has been revolutionized by the abundance of high-precision observations of its constituent galaxies and lays the foundation for extending our models to galaxy groups beyond the Local Volume (> 10 Mpc). Tollerud et al. (2011) studied the frequency and distribution of LMC-like satellites around MW-luminosity (L_*) hosts

in SDSS. They found that 12% of L_* hosts have an LMC analog ($M_r \lesssim -18.3$) within 75 projected kpc, and 42% have one within 250 projected kpc. They also show that these results are consistent with cosmological simulations that employ a ΛCDM cosmology, specifically that their observational sample matches the frequency of finding MW–LMC analogs at low redshift, as well as the radial and velocity distributions and luminosity functions of their satellite sample. Similar studies with SDSS and GAMA have found that approximately 11% of MW-like hosts in both surveys have a massive satellite, though only $\sim 3.5\%$ have two companions that are at least as massive as the SMC (Liu et al., 2011; Robotham et al., 2012).

More recently, the SAGA survey has observed 36 MW-mass analogs at $z \sim 0.01$, finding a total of 127 satellite galaxies (complete to $M_{r,o} < -12.3$, Geha et al., 2017; Mao et al., 2021). They find that approximately 30% of their MW-mass analogs host at least one satellite that is similar in stellar mass to the LMC, and 25% of MW-mass analogs have at least two satellites that are more massive than $M_* = 3 \times 10^8 \, \mathrm{M_\odot}$.[1] Additionally, they find that the quenched fraction of satellite galaxies around MW-mass hosts is below $\sim 30\%$ for satellites with stellar mass $M_* = 10^{6.8} - 10^9 \, \mathrm{M_\odot}$. This is at extreme odds with the satellite population of the MW and M31, which have a total quenched satellite fraction of $\sim 50\%$, and more than $\sim 80\%$ for satellites with stellar mass $M_* < 10^{7.5} \, \mathrm{M_\odot}$. While the SAGA survey results do not point to a discrepancy with ΛCDM, they imply that the population of satellites around the LG, particularly those that are quenched, are rare compared to similar low-redshift systems in observations.

While these studies show that it is not extremely surprising to find MW-like galaxies with massive satellite companions at low redshift, such studies have yet to be extended to higher redshift ($z > 0.1$) to understand the LG in the context of galaxy evolution and dynamics over cosmic time. Additionally, these observational samples have not yet extended their findings to MW–M31–M33-analogs, or to MW–M31–M33–LMC analogs, and as such provide a limited picture about the rarity of galaxy groups with *multiple* massive galaxies, each with their own massive satellite population. To supplement our understanding of the LG in the context of ΛCDM cosmology, we can turn to cosmological simulations.

---

[1]This type of system would be analogous to a MW–LMC–SMC system in mass, though may not necessarily have a dynamically bound LMC–SMC pair.

1.2 Modern Cosmological Simulations: The Illustris Suite

Advancements in computation, particularly investments in high-performance computing and improvements in state-of-the-art numerical algorithms such as AREPO (Springel, 2010), have completely revolutionized our ability to construct models that permit meaningful comparisons with observations. There are broadly two methods that are employed to connect the ΛCDM paradigm with predictive statistical studies of the Universe. The first is a class of "post-processing models" known as semi-analytic models, which use observational data to constrain the physical prescriptions employed to assign galaxy properties to n-body dark-matter cosmological simulations. The second method is via cosmological simulations, which use n-body and hydrodynamic simulations to employ galaxy formation models that self-consistently evolve dark matter and baryonic matter simultaneously. One such cosmological simulation is Illustris, which is utilized in Chapters 3 and 4 to study low-mass and high-mass galaxy pair properties across cosmic time.

The Illustris Project (Vogelsberger et al., 2014a,b; Nelson et al., 2015; Genel et al., 2014; Sijacki et al., 2015), first completed in 2013, is a suite of large volume simulations that model the evolution of dark matter and baryonic matter from $z = 127$ to $z = 0$ in a $(106.5\,\mathrm{Mpc})^3$ volume, and follow a ΛCDM cosmology consistent with measurements from *WMAP-9* (Hinshaw et al., 2013). The simulation suite consists of runs with three different resolutions, each of which include a full hydrodynamic run and an n-body dark-matter-only run, and were created to study galaxy formation and evolution throughout cosmic time.

The Illustris simulation evolves dark matter and star particles, as well as stellar wind particles, gas cells, and supermassive black holes (except in the dark-matter-only runs, which contain only dark matter particles). Each hydrodynamic run includes a variety of astrophysical processes that impact galaxy formation, such as star formation and evolution, gas cooling, and feedback from galactic winds, AGN and SNe. Despite the complexity of the galaxy formation models, and though it is not tuned to match all observations explicitly, Illustris does an excellent job at reproducing a variety of observational data, such as the distribution of neutral hydrogen over large-scales, the distribution of satellite galaxies about their host galaxies, and galaxy morphologies (Vogelsberger et al., 2014a). However, Illustris

produces low-mass galaxies that are a factor of a few too large and have stellar mass fractions that are higher than those observed in the real universe (Nelson et al., 2015). Despite these and a few additional shortcomings, Illustris shows that the ΛCDM paradigm is generally capable of reproducing many of the physical features of our Universe.

The next generation of simulations, IllustrisTNG (also known simply as TNG), build upon the framework set forth by the original Illustris simulation (Springel et al., 2018; Marinacci et al., 2018; Nelson et al., 2018; Naiman et al., 2018; Pillepich et al., 2018a), and employ a few revised galaxy formation models, such as those for galactic winds and kinetic feedback from black holes. The revised galaxy formation models were developed in part to target regimes where the Illustris simulation failed to reproduce observable galaxy features. For example, changing the galactic wind prescription decreased the sizes of galaxies with $M_* < 10^{10.7}\,\mathrm{M_\odot}$, and resulted in galaxy mass functions at $z = 0$ that were more consistent with observations at high-mass ($M_* > 10^{11.5}\,\mathrm{M_\odot}$) and low-mass ($M_* < 10^{10}$) $\mathrm{M_\odot}$ (Pillepich et al., 2018b). The stellar masses of the LMC, SMC, and M33 are all $< 10^{10}\,\mathrm{M_\odot}$, which means they are all firmly in the low-mass regime impacted by changes in the TNG galaxy formation model.

The TNG simulations were created with three different volumes, each of which has a different resolution, and follow a cosmology consistent with measurements from the 2015 Planck Data Release (Planck Collaboration et al., 2016). The smallest volume is $(50\,\mathrm{Mpc})^3$ and named TNG50. TNG50 boasts the highest resolution of any TNG simulation, with dark matter particles of mass $m_{\mathrm{DM}} = 4.5 \times 10^5\,\mathrm{M_\odot}$ and baryon mass $m_{\mathrm{bary}} = 8.5 \times 10^4\,\mathrm{M_\odot}$, and is able to resolve down to a physical scale of 70pc in star forming regions within galaxies. For unprecedented high-resolution studies of MW-mass and low-mass galaxies in a cosmological volume, TNG50 is unbeatable. However, the TNG50 volume only contains ~ 100 MW-mass analogs at $z = 0$ (Pillepich et al., 2019). For the purposes of studying a large statistical sample of galaxy pairs in both the low-mass and high-mass regime (as done in Chapters 3 and 4 of this dissertation), TNG50 simply doesn't have a large enough volume to allow a robust statistical analysis of high-mass pairs as a function of time.[2]

The largest volume simulation in the TNG suite is TNG300, with volume $(300\,\mathrm{Mpc})^3$ and

---

[2]This is addressed in more detail in Ch.3, where we specify that we require a sample of at least 100 high-mass pairs, so that we can avoid uncertainties due to low number statistics.

dark matter and baryonic particle masses of $m_{\mathrm{DM}} = 5.9 \times 10^7 \, \mathrm{M}_\odot$ and $m_{\mathrm{bary}} = 1.1 \times 10^7 \, \mathrm{M}_\odot$. As a much larger cosmological volume with $\sim 130\times$ lower resolution than the TNG50 simulation, TNG300 is ideal for statistical studies of MW-mass analogs and MW–M31 pairs, and for studies of very high mass ($> 10^{13-14} \, \mathrm{M}_\odot$) galaxy clusters. However, an analog of the SMC in TNG300 would resolve into only ~ 25 stellar particles. At close separations to a host with $10\times$ more mass, subhalo finding algorithms and merger trees will have trouble distinguishing the host and satellite subhalos.

The middle volume simulation, TNG100, combines a large volume $(100 \, \mathrm{Mpc})^3$ with high resolution ($m_{\mathrm{DM}} = 7.5 \times 10^6 \, \mathrm{M}_\odot$ and $m_{\mathrm{bary}} = 1.4 \times 10^6 \, \mathrm{M}_\odot$). In TNG100, there are over 300 MW–M31-mass analog pairs at $z = 0$, which provides a statistically significant sample of high-mass pairs. Additionally, low-mass pairs will be resolved into well over 150 stellar particles, meaning that the subhalo finders should robustly distinguish low-mass pairs even at relatively close separations ($\sim 15 \, \mathrm{kpc}$). I use the TNG100 simulation to study low-mass and high-mass pairs as a function of redshift due to this balance of volume and resolution (see Ch. 3 and Ch. 4 for more detail).

In addition, the n-body dark-matter-only analog simulation to TNG100 is TNG100-Dark. Having access to the full physics hydrodynamic simulation, and being able to compare 1:1 with the dark-matter-only simulation means that we can tease apart the impact of baryonic physics on the resulting evolution of galaxies, and on galaxy pair frequency and dynamics. In Ch. 3, I leverage the TNG100-Dark simulation to provide a complimentary comparison of the pair fractions of low- and high-mass pairs in a simulation without the effect of the subgrid baryonic physics.

1.3 Utilizing Simulations to Connect Local Group Dynamics and Dynamical Expectations from ΛCDM

While observational studies have found a variety of MW–LMC and M31–M33 mass analogs at low redshift, it is unclear whether these types of systems are common at higher redshift ($z > 0.1$). This is complicated in turn since the LMC and M33 are likely on their first infall (Besla et al., 2007; Besla et al., 2010; Kallivayalil et al., 2013; Patel et al., 2017a,b), implying that the MW–M31 system looked much different a few Gyr ago, before the infall

of these massive satellites and their accompanying satellite systems. Additionally, it is challenging to infer whether or not the dynamics of the observed LG analogs are similar to those of the massive satellites in the LG, in large part because proper motion measurements of galaxies outside of the Local Volume are not currently feasible. Thus, we must turn to cosmological simulations to deeply understand our LG and its formation history.

1.3.1 LG Analogs in Cosmological Simulations

Searches for analogs of LG galaxies in cosmological studies have revealed a complex picture of the rarity of such systems at low redshift. Cosmological simulations allow employing additional selection criteria to select LG analogs, beyond the typical separation and mass (or luminosity) criteria that are used in observational selections. Such studies of LG analogs can go an additional step further, utilizing observed kinematic data of LG galaxies to find *dynamical* analogs of the LG at low redshift.

Boylan-Kolchin et al. (2011) shows that 35% of MW and M31-mass analogs in the n-body cosmological simulation Millenium-II have a massive satellite analog (mass ratio $> 1 : 10$, similar to the mass ratio of the MW–LMC and M31–M33 systems) at $z = 0$. This is in agreement with the observational studies of LG analogs discussed in 1.1.3, which found that between $11 - 42\%$ of low redshift ($z \lesssim 0.1$) MW-mass analogs in SDSS, GAMA, and the SAGA survey have at least one massive satellite. Boylan-Kolchin et al. (2011) employed additional selection criteria to find MW-mass analogs with a LMC–SMC-mass pair with $r_{\rm sep} < 50\,{\rm kpc}$ and $v_{\rm rel} < 150{\rm km\ s}^{-1}$ (the present day separation and relative velocity of the LMC and SMC are $23\,{\rm kpc}$ and $128 \pm 32{\rm km\ s}^{-1}$, Besla et al., 2007; Besla, 2015), and find that a mere 2.5% of present day MW hosts have a bound MC analog. This picture of the relative rarity of the MW–LMC–SMC system is markedly different than that revealed by studies of mass analogs alone.

Similar studies of the frequency of LG analogs have been conducted in the Illustris simulations. Patel et al. (2017a) finds that 24.4% of MW/M31-mass halos in Illustris-Dark have a massive satellite analog (mass ratio $> 1 : 10$) at $z = 0$ which is consistent with observational mass-selected studies. However, Pillepich et al. (2023) finds that, out of 42 MW–LMC-mass analogs in TNG50 at $z = 0$, only 4 systems have a similar relative velocity

and separation to the MW–LMC.

The challenge of finding such specific matches to the LG is further complicated by the requirement that there are two massive hosts, each of which have a massive satellite (therefore a MW-M31-M33-LMC analog), although studies have found that a larger number of massive satellites is more common in groups with more than one massive host (Pillepich et al., 2023).

On one hand, it may not be particularly surprising to find very few massive satellites with kinematic properties similar to the MCs at a given redshift. The MC system is at a point of its orbit just past its first pericenter passage of the MW, where an orbiting system will spend the least amount of elapsed time. It is more common to find satellites at larger distances from their hosts, particularly at apocenter, where they spend more time. On the other hand, the LG may be dynamically rare at low z, but studies have not yet extended this conclusion to higher redshifts. For example, the infall of massive satellite systems might be much more common at high redshift, which would make the chance of finding dynamical LG analogs larger at higher redshift.

To be succinct, it is not yet entirely clear whether the LG is fully consistent with a ΛCDM model. Due to the rarity of dynamical LG analogs at $z = 0$, it's difficult to use cosmological simulations to test whether LG properties, such as the mass and spatial distribution of MW satellites, are in line with cosmological expectations of galaxy groups of similar total mass. Gaining clarity into how exactly the LG fits into this picture thus requires studies of galaxy pairs more broadly, especially at $z > 0$.

1.4 The Challenge of Connecting Observations and Theory: Why Theoretically Motivated Frameworks are of Critical Importance

Dynamical studies of galaxy pairs in cosmological simulations help put the LG into a cosmological perspective, deepening our understanding of the merger and accretion history of LG-like halos in ΛCDM cosmologies, but they are also more broadly useful for non-LG studies, as they are critical to facilitate the connection between observations and theoretical predictions. Here, I will explain the importance of constructing robust frameworks, or self-consistent schemes that permit equitable comparisons between observations and theory, for both LG studies and future cosmological simulation comparisons to observations, and how

they are addressed in this dissertation.

1.4.1 Frameworks for Future LG Studies

High-precision measurements of proper motions in the LG are improved with each subsequent epoch of data, as longer baselines enable tighter constraints (smaller errors) on proper motions. Additionally, as constraints on the motions of stars in the outer halo of the MW improve, so too will measurements of the travel velocity of the MW disk with respect to its dark matter halo. Garavito-Camargo et al. (2021) also showed that more distant stellar tracers will yield larger measured values of the travel velocity (up to the true velocity of the MW disk due to the reflex motion imparted by the LMC). However, it is unclear how a larger or more precise travel velocity measurement might translate to LG dynamical studies. I address this problem directly in Ch. 2, by providing a framework to account for the MW travel velocity in Timing Argument studies. This work additionally addresses questions such as: How might future high-precision measurements improve constraints on the mass of the LG? Can the implementation of a travel velocity of the MW disk resolve tensions between the MW–M31 orbit and cosmological expectations? How will future travel velocity measurements change LG mass estimates and the inferred orbital parameters of the MW–M31 interaction?

At higher redshifts, pair fraction studies will allow us to interpret how common MW–M31 or LMC–SMC pairs are at redshifts from $z = 0 - 4$, and will lead to a broader understanding of low-mass systems that might become infalling LMC–SMC analogs at late times. In Chapters 3 and 4 of this dissertation, I take the approach of studying low-mass and high-mass pairs (primary stellar masses of $10^8 < M_{*1} < 5 \times 10^9 \, \mathrm{M}_\odot$ and $5 \times 10^9 < M_{*1} < 10^{11} \, \mathrm{M}_\odot$ respectively) as a function of redshift, considering both their frequency and dynamics, to see if the behavior of these systems at earlier times can help explain why dynamical LG analogs are so challenging to find at $z = 0$.

Studying the merger timescales of pairs in the low-mass and high-mass regime (such as MW–M31 or LMC–SMC pairs) can help begin to answer questions such as: can low-mass systems have long enough merger timescales such that they can be bound for many Gyr, then enter the halo of a more massive system, all before merging? What are the typical merger timescales of MW–M31 pairs at low $z \sim 0$ and high redshift $z > 2$, and do they change over

those timescales compared to their low-mass counterparts?

1.4.2 Frameworks for Future Low-mass and High-mass Pair Studies

In addition to providing more context for the formation history of the LG, creating frameworks to interpret observations of low-mass and high-mass galaxy pairs will be crucial in an era of deeper and wider observations with JWST, Roman, Rubin, and the next generation ELTs, which will provide an unprecedented view into low-mass systems. These frameworks are necessary because it is unclear if the standard techniques used to study the pair fractions, merger timescales, and merger rates of high-mass systems in observations can be applied to galaxy pairs in the low-mass regime. Further, it is unclear if pair samples chosen with the same selection criteria over a variety of redshifts, which is standard for searches of LG-analogs and for pair fraction and merger rate studies, can be used to discern the true redshift evolution of these quantities from observations for comparison to theoretically predicted values. These subjects are tackled in detail in Chapters 3 and 4.

Frameworks that enable robust and meaningful interpretations of the relationship between low-mass and high-mass pairs are critical for future studies of the LG and for future observational efforts that seek to compare low-mass and high-mass galaxy populations over cosmic time.

1.5 Outline of Thesis

This dissertation is organized as follows. In Chapter 2, I construct a new framework to utilize the first measurements of the reflex motion of the MW stellar disk (imparted by the recent pericentric passage of the MCs) to improve our models of the LG mass and orbit of MW–M31. I also show that, by accounting for the travel velocity of the MW, improved constraints on the MW-M31 orbital parameters make the LG more cosmologically "expected". In Chapter 3, I utilize the highest resolution run of the $(100\,\mathrm{Mpc})^3$ IllustrisTNG volume to study the pair fractions of isolated low-mass and high-mass pairs as a function of redshift from $z = 0 - 4$. By employing separation criteria that select pairs via physical static separation and by separation cuts that vary as a function of mass and redshift, I construct a physically

motivated framework to permit pair fraction studies of low- and high-mass pairs in future observational samples. I also show that LMC–SMC analogs are more common at higher redshift, and place the observed properties of the LG in a cosmological context as a function of redshift. I extend this framework in Chapter 4, where I analyze the orbits of isolated low-mass and high-mass subhalo pairs in the TNG100 simulation to quantify their merger timescales as a function of redshift. I also study how the two sets of pair selection criteria from Ch. 3 affect the resulting merger timescales, and make recommendations of considerations for observers who seek to perform self-consistent merger rate studies at all masses and redshifts. Finally, I present a summary of the key results of this body of work in Chapter 5, and conclude with a number of future directions motivated by this dissertation. In particular, I discuss ways that these frameworks can be extended to further enable interpretations of observations in the coming era of Big Data and pioneering observatories.

Chapter 2

Implications of the Milky Way Travel Velocity for Dynamical Mass Estimates of the Local Group

Abstract

The total mass of the Local Group (LG) is a fundamental quantity that enables interpreting the orbits of its constituent galaxies and placing the LG in a cosmological context. One of the few methods that allows inferring the total mass directly is the "Timing Argument," which models the relative orbit of the Milky Way (MW) and M31 in equilibrium. The MW itself is not in equilibrium, a byproduct of its merger history including the recent pericentric passage of the LMC, and recent work has found that the MW disk is moving with a lower bound "travel velocity" of ~ 32 km s^{-1} with respect to the outer stellar halo. Previous Timing Argument measurements attempt to account for this non-equilibrium state, but have been restricted to theoretical predictions for the impact of the LMC specifically. In this paper, we quantify the impact of a travel velocity on recovered LG mass estimates using several different compilations of recent kinematic measurements of M31. We find that incorporating the measured value of the travel velocity lowers the inferred LG mass by 10–12% compared to a static MW halo. Measurements of the travel velocity with more distant tracers could yield even larger values, which would further decrease the inferred LG mass. Therefore, the newly measured travel velocity directly implies a lower LG mass than from a model with a static MW halo and must be considered in future dynamical studies of the Local Volume.

2.1   Introduction

The total mass of the Local Group (LG) is an important quantity in many local cosmological and Milky Way (MW) applications. For example, it is used to identify analogous halos in

cosmological simulations and thus allows comparing host galaxy and satellite galaxy number counts and properties (e.g., Marinacci et al., 2017; Dooley et al., 2017; Patel et al., 2017a; Besla et al., 2018; Patel et al., 2018; Garrison-Kimmel et al., 2019a,b; Sawala et al., 2022). It is also used to turn the kinematics of LG galaxies into orbital histories (e.g., Peebles, 2017), which is used to interpret their gas content (e.g., Fillingham et al., 2018; Putman et al., 2021) and star formation histories (e.g., Tolstoy et al., 2009). However, as most of the mass in the LG is in dark matter distributed over megaparsec scales, it is difficult to directly measure its total mass.

Given its utility in studies of the local universe, several methods have been used to dynamically infer the mass of the LG. Many of these techniques determine the individual masses of the MW and M31 independently (e.g. Watkins et al., 2010; Fardal et al., 2013; Diaz et al., 2014; Carlesi et al., 2017; Patel et al., 2018; Eadie and Jurić, 2019; Fritz et al., 2020; Deason et al., 2021; Villanueva-Domingo et al., 2021; Wang et al., 2022), often via the dynamics of their satellites and stellar streams, then combine them to get an estimate of the total LG mass. However, these methods generally only measure the enclosed mass of the MW or M31 within some internal radius (i.e., much smaller than LG scales) and then extrapolate, leading to mass-profile-dependent estimates of the total LG mass. Other techniques aim to more directly measure the mass of the LG en masse, for example looking for Local Group analogs in cosmological simulations based on stellar mass and kinematic criteria (e.g., Li and White, 2008; González et al., 2014; Zhai et al., 2020; Hartl and Strigari, 2022), by studying the kinematics of Local Volume (LV) galaxies (e.g., Diaz et al., 2014; Peñarrubia et al., 2014), or by applying machine learning (ML) techniques to hydrodynamic simulation data (e.g., McLeod et al., 2017; Villanueva-Domingo et al., 2021). One of the earliest methods utilized in this vein is the "Timing Argument," which uses the fact that the LG galaxies (most often the MW and M31) are bound and approaching pericenter in their relative orbit, but must have been close enough over cosmic time to not be pulled apart by the Hubble flow. The Timing Argument can be generalized to simultaneously model the orbits of LV galaxies around the LG (Peñarrubia et al., 2016; Peñarrubia and Fattahi, 2017), but here we restrict our analysis to the "classic" Timing Argument using only the MW and M31. We summarize the relevant details of the Timing Argument method in Section 2.2.1.

The Timing Argument (using the MW and M31) uses the observed kinematics of M31 to model the relative orbit of the two galaxies as a Keplerian orbit. Assuming Keplerian dynamics enables dynamically measuring the total mass of the MW and M31 with analytic expressions for all relevant kinematic quantities because of the simplicity of the two-body equations of motion. The inferred mass from the Timing Argument thus directly depends on the observationally-measured kinematics of the M31 center.

However, the LG is not in equilibrium. In the past decade, a number of studies have begun to consider of the impact of the Large Magellanic Cloud (LMC) on the mass and inferred dynamics of the LG. Peñarrubia et al. (2016) studied the effect of the presence of the LMC on the total mass estimates of the LG via the Timing Argument by modelling the motion of M31 about the MW-LMC barycenter, and using the kinematics of 35 LV Galaxies to simultaneously measure a MW mass of $M_{MW} = 1.04^{+0.26}_{-0.23} \times 10^{12} M_{\odot}$, M31 mass of $M_{M31} = 1.33^{+0.39}_{-0.33} \times 10^{12} M_{\odot}$, LMC mass of $M_{LMC} = 0.25^{+0.09}_{-0.08} \times 10^{12} M_{\odot}$, and LG mass of $M_{LG} = 2.64^{+0.42}_{-0.38} \times 10^{12} M_{\odot}$. Another recent Timing Argument work by Benisty et al. (2022) modelled the orbital history of M31 and the MW, with and without a mass and orbital model of the LMC, to estimate the contribution of the LMC-induced shift in the MW barycenter on the measured tangential and radial velocities of M31, then applied these corrections to their model to remove the impact of the LMC in their analysis, and found that the inferred LG mass decreased by 10%.

Recent studies of the dynamics of the MW and its satellites have revealed that the infall of the Magellanic Clouds (MCs) is causing significant distortions to the dark matter and stellar distribution in the MW halo (Laporte et al., 2018a,b; Garavito-Camargo et al., 2019; Conroy et al., 2021; Erkal et al., 2021). In addition, numerous studies of the interaction between the MW and LMC (using simulated analogs) have quantified the expected LMC-induced reflex motion of the MW disk and inner halo, which are likely being accelerated away from the center-of-mass reference frame of a static MW halo (Gómez et al., 2015; Cunningham et al., 2020; Petersen and Peñarrubia, 2020; Garavito-Camargo et al., 2021). The induced systematic shift in the measurements of the M31 kinematics may have created a bias in previous mass measurements via the Timing Argument, thus impacting interpretations of LG dynamics, orbital histories, cosmological context, etc.

Previous Timing Argument studies have accounted for the impact of an LMC-induced reflex motion on the orbital histories of the other galaxies in the LG. However, other satellite mergers such as the ongoing merger with the Sagittarius dwarf galaxy, as well as the past merger with the progenitor of the Gaia–Enceladus–Sausage, have likely also imparted their own reflex motion to the inner MW halo. A signature of the reflex motion of the MW is imprinted as a velocity dipole in the radial velocities of stars in the outer stellar halo Garavito-Camargo et al. (2021). Recently, the instantaneous velocity offset of the inner MW with respect to the outer halo was directly measured using tracer stars in the stellar halo of the MW (the "travel velocity"; Petersen and Peñarrubia 2021). Thus, the newly measured travel velocity can be used in Timing Argument studies in place of orbital modeling to account for the expected perturbations of the inner MW halo without having to make assumptions about the mass or dynamical history of the LMC or other satellites.

Studies have considered variations to the standard Timing Argument model. For example, one such model considered the effect of dark energy, and finds that the addition of a cosmological constant to the energy equations yields a $\sim 13\%$ increase in the recovered mass (Partridge et al., 2013). Similarly, the travel velocity of the MW disk, which has only recently been first measured, introduces its own complication to the standard Timing Argument model.

In this Article, we quantify the impact of this newly measured MW disk motion on LG mass measurements using the Timing Argument, thus accounting for observational misinterpretations in a model-independent way for the first time. We also show that improvements in the measurements of the MW travel velocity may lead to even larger discrepancies between TA schemes with and without a MW travel velocity. We also explore a combination of recent measurements of the distance and proper motions of M31 to infer the effect of the travel velocity in a data-set-independent way. As a result, we find that the travel velocity significantly impacts the inferred mass of the LG in Timing Argument studies, and thus must be accounted for in further dynamical studies of the LV.

2.2 Methods and Data

2.2.1 Dynamical Model: The Timing Argument

Following past work that utilizes the "Timing Argument," we assume that the orbital trajectories of the MW and M31 — the Local Group system — over cosmic history are well described by Keplerian orbits (e.g., Kahn and Woltjer, 1959; Lynden-Bell, 1981; Kroeker and Carlberg, 1991; Li and White, 2008; van der Marel et al., 2012a; Peñarrubia et al., 2016). By assuming that M31 and the MW are gravitationally bound and were last at closest approach in the early universe (i.e., the two galaxies have not yet strongly interacted), we can then use the present-day kinematics of M31 relative to the MW to estimate the total mass of the LG (i.e., using the Timing Argument).

In this work, we largely follow the methodology and notation defined in Peñarrubia et al. (2016). Briefly recapping the classical Timing Argument method, we assume that the dynamics of the MW and M31 pair is dominated by the local gravitational potential of the LG, and therefore the Hubble flow can be neglected for computing the relative orbits of the galaxies (see, e.g., Peñarrubia et al., 2014). Since we observe the relative position and motion between M31 and the MW, we reduce the dynamics of the galaxies in the LG system to a single Keplerian orbit that specifies the relative orbit between the galaxies and is completely determined by four model parameters: the total mass of the LG, $M_{\rm LG}$, the semimajor axis, a, the eccentricity, e, and the present value of the eccentric anomaly, η.

In terms of these four model parameters, the closed-form equations for relevant two-body quantities that are closer to observables, like the separation between the masses, r, the elapsed time since last pericenter, t, and the radial and tangential velocity components, $v_{\rm rad}$ and $v_{\rm tan}$,

are given by

$$r = a\left(1 - e\,\cos\eta\right) \tag{2.1}$$

$$t = \left(\frac{a^3}{GM}\right)^{1/2}\left(\eta - e\,\sin\eta\right) \tag{2.2}$$

$$v_{\mathrm{rad}} = \left(\frac{GM}{a}\right)^{1/2}\frac{e\,\sin\eta}{1 - e\,\cos\eta} \tag{2.3}$$

$$v_{\mathrm{tan}} = \left(\frac{GM}{a}\right)^{1/2}\frac{\sqrt{1 - e^2}}{1 - e\,\cos\eta} \quad . \tag{2.4}$$

In the expressions above, r is the separation between the centers of the MW and M31 halos, the time since last pericenter, t, is the age of the Universe, and the velocity components, $(v_{\mathrm{rad}}, v_{\mathrm{tan}})$, express the radial and tangential velocity components of M31 relative to the center of the MW halo.

In a simpler universe where the MW and M31 are point masses and there are no other massive bodies in the LG system, we could transform the observed heliocentric sky position, distance, and velocity of M31 to a MW Galactocentric reference frame and combine these with an estimate of the Hubble time to obtain the four "observables" $(r, t, v_{\mathrm{rad}}, v_{\mathrm{tan}})$. These observables would be enough to infer the four model parameters $(M_{\mathrm{LG}}, a, e, \eta)$ using Equations 2.1–2.4.

To describe this "classical" Timing Argument approach in more detail and set the stage for extending it, we adopt the notation of Peñarrubia et al. (2016) in which $\boldsymbol{v}_{\mathrm{A}\to\mathrm{B}}$ represents the velocity vector of A as measured in the reference frame of B and $\boldsymbol{x}_{\mathrm{A}\to\mathrm{B}}$ represents the position vector of A as measured from B. With this notation, $\boldsymbol{v}_{\mathrm{A}\to\mathrm{B}} = -\boldsymbol{v}_{\mathrm{B}\to\mathrm{A}}$ and $\boldsymbol{v}_{\mathrm{A}\to\mathrm{C}} = \boldsymbol{v}_{\mathrm{A}\to\mathrm{B}} + \boldsymbol{v}_{\mathrm{B}\to\mathrm{C}}$.

In the classical Timing Argument, the MW disk and M31 are assumed to occupy the center of the potential well of their dark matter halos and have zero velocity with respect to the halos. We refer to this reference frame in the MW dark matter halo as 'MW$_{\mathrm{halo}}$'. Thus, the position and velocity of M31 with respect to the MW can be represented by $\boldsymbol{x}_{\mathrm{M31}\to\mathrm{MW_{halo}}}$ and $\boldsymbol{v}_{\mathrm{M31}\to\mathrm{MW_{halo}}}$, which are assumed to be equivalent to the position and velocity of M31 with respect to the center of the MW disk. Then, the *observed* position and velocity of M31,

measured in a heliocentric reference frame, are given by

$$\boldsymbol{x}_{\mathrm{M31}\to\odot} = \boldsymbol{x}_{\mathrm{M31}\to\mathrm{MW}_{\mathrm{halo}}} + \boldsymbol{x}_{\mathrm{MW}_{\mathrm{halo}}\to\odot} \tag{2.5}$$

$$\boldsymbol{v}_{\mathrm{M31}\to\odot} = \boldsymbol{v}_{\mathrm{M31}\to\mathrm{MW}_{\mathrm{halo}}} + \boldsymbol{v}_{\mathrm{MW}_{\mathrm{halo}}\to\odot} \quad . \tag{2.6}$$

Here $|\boldsymbol{x}_{\mathrm{M31}\to\mathrm{MW}_{\mathrm{halo}}}| = r$ as determined from Equation 2.1, $\boldsymbol{v}_{\mathrm{M31}\to\mathrm{MW}_{\mathrm{halo}}}$ is determined completely by the Keplerian model parameters (through v_{rad} and v_{tan}), and the position and velocity of the center of the MW halo as measured from the sun are $\boldsymbol{x}_{\mathrm{MW}_{\mathrm{halo}}\to\odot}$ and $\boldsymbol{v}_{\mathrm{MW}_{\mathrm{halo}}\to\odot}$.

However, the true dynamics of the MW–M31 system are not so simple. Perturbations introduced by interactions and mergers between the MW and its satellite galaxies, such as the merger of the Sagittarius dwarf galaxy or the recent pericentric passage of the LMC, break the assumption that the MW disk is stationary in the center of its dark matter halo. In fact, these interactions will introduce an additional reflex motion component in observations from the MW disk compared to the $\mathrm{MW}_{\mathrm{halo}}$ reference frame. The LMC's impact on the dynamics of the MW disk and inner halo have been studied in detail by (e.g., Gómez et al., 2015; Garavito-Camargo et al., 2019; Petersen and Peñarrubia, 2020; Garavito-Camargo et al., 2021). These works imply that we must include additional terms in Equations 2.5 and 2.6 to account for the travel velocity of the MW disk with respect to the center of the halo in its unperturbed state. Thus, the observed position and velocity vectors of M31 from the solar reference frame become

$$\boldsymbol{x}_{\mathrm{M31}\to\odot} = \boldsymbol{x}_{\mathrm{M31}\to\mathrm{MW}_{\mathrm{halo}}} + \boldsymbol{x}_{\mathrm{MW}_{\mathrm{halo}}\to\mathrm{MW}_{\mathrm{disk}}} + \boldsymbol{x}_{\mathrm{MW}_{\mathrm{disk}}\to\odot} \tag{2.7}$$

$$\boldsymbol{v}_{\mathrm{M31}\to\odot} = \boldsymbol{v}_{\mathrm{M31}\to\mathrm{MW}_{\mathrm{halo}}} + \boldsymbol{v}_{\mathrm{MW}_{\mathrm{halo}}\to\mathrm{MW}_{\mathrm{disk}}} + \boldsymbol{v}_{\mathrm{MW}_{\mathrm{disk}}\to\odot} \tag{2.8}$$

where "$\mathrm{MW}_{\mathrm{halo}}$" refers to a reference frame centered at and moving with the center of mass of the outer MW halo, "$\mathrm{MW}_{\mathrm{disk}}$" refers to a reference frame centered at and moving with the center of the MW disk, and $\boldsymbol{x}_{\mathrm{MW}_{\mathrm{disk}}\to\odot}$ and $\boldsymbol{v}_{\mathrm{MW}_{\mathrm{disk}}\to\odot}$, respectively, are the adopted solar position and velocity in the Galaxy. The values we adopt for $\boldsymbol{x}_{\mathrm{MW}_{\mathrm{disk}}\to\odot}$ and $\boldsymbol{v}_{\mathrm{MW}_{\mathrm{disk}}\to\odot}$ (shortened to $\boldsymbol{x}_{\odot}$ and $\boldsymbol{v}_{\odot}$) are given in Table 2.1 below.[1]

---

[1]Note that in principle, there is also a term $\boldsymbol{v}_{\mathrm{M31}_{\mathrm{halo}}\to\mathrm{M31}_{\mathrm{disk}}}$; however, there are not yet measurements of the differential motion of the M31 disk with respect to the M31 halo, so we neglect this term. See further

Observationally, the reflex motion of the disk imprints itself on velocity measurements as an instantaneous velocity shift. Recently, Petersen and Peñarrubia (2021) used tracers in the outer MW stellar halo to measure this instantaneous travel velocity $\boldsymbol{v}_{\text{travel}} = \boldsymbol{v}_{\text{MW}_{\text{halo}} \to \text{MW}_{\text{disk}}}$. They find $\left|\boldsymbol{v}_{\text{travel}}\right| = 32 \pm 4 \text{km s}^{-1}$ with a highest likelihood apex direction in Galactocentric coordinates of $(\ell, b)_{\text{apex}} = (56^{+9}_{-9}, -34^{+10}_{-9})$ degrees. We assume that $\boldsymbol{x}_{\text{MW}_{\text{halo}} \to \text{MW}_{\text{disk}}} \approx 0$ motivated by the fact that this displacement is likely much smaller than the distance between the MW and M31 $\boldsymbol{x}_{\text{MW}_{\text{halo}} \to \text{MW}_{\text{disk}}} \ll r$ (as expected from simulations; e.g., Garavito-Camargo et al., 2021). However, it is important to note that this displacement is still significant on scales relevant for many other MW studies (see Section 2.4.3 for more details).

Figure 2.1 shows a schematic of these different vectors — all drawn in a frame that is comoving with the MW_{halo} frame — and a rough illustration of the geometry we assume. For clarity, we show $\boldsymbol{x}_{\text{MW}_{\text{halo}} \to \text{MW}_{\text{disk}}} = \boldsymbol{x}_{\text{travel}}$, $\boldsymbol{v}_{\text{MW}_{\text{halo}} \to \text{MW}_{\text{disk}}} = \boldsymbol{v}_{\text{travel}}$, and $\boldsymbol{v}_{\text{M31} \to \odot} = \boldsymbol{v}_{\text{obs}}$.
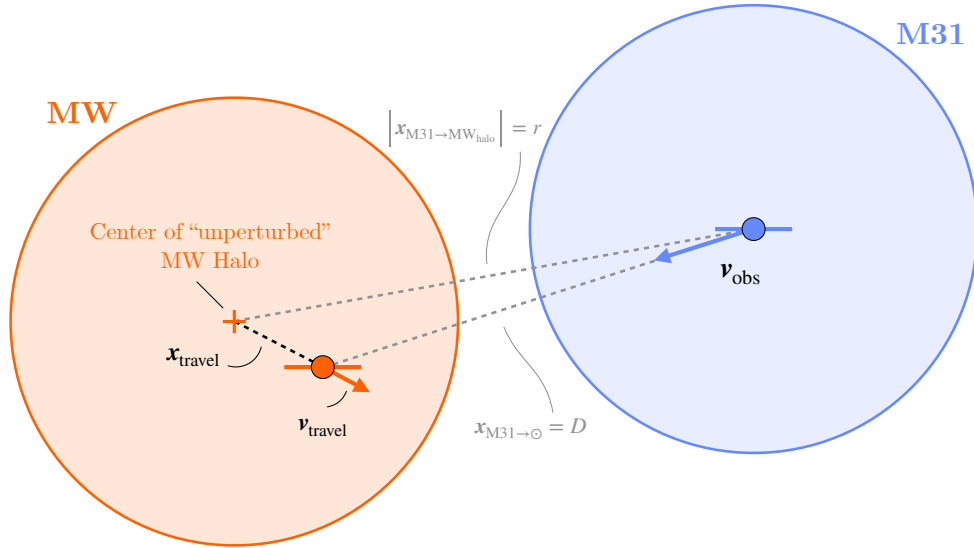
Figure 2.1: Schematic of the Milky Way (MW) and M31 system, not to scale. The shaded regions represent the halos of both galaxies. Shown are an artistic representation of the velocity and position vectors that are relevant in our model, including $D = \boldsymbol{x}_{\text{M31} \to \odot}$, the measured distance to M31; $\boldsymbol{x}_{\text{M31} \to \text{MW}_{\text{halo}}}$, the distance between the centers of both halos; and $\boldsymbol{v}_{\text{obs}}$, the measured 3D velocity of M31. Finally, $\boldsymbol{x}_{\text{travel}}$ and $\boldsymbol{v}_{\text{travel}}$ are the present distance and velocity between the center of the MW halo and the center of the MW disk. For this study, we assume $\boldsymbol{x}_{\text{travel}} \ll r, D$, and $|\boldsymbol{v}_{\text{travel}}| = 32 \pm 4 \text{km s}^{-1}$ from Petersen and Peñarrubia (2021).

---

discussion in Section 2.4.5.

The present distance and relative velocity of M31, as well as the age of the universe (used in Equation 2.2), are key observables that are used to constrain our Timing Argument model. In this paper, we consider three different compilations of data to understand how different measurements might affect the Timing Argument model with the addition of the travel velocity. In particular, we consider two different M31 distance measures: an approximated distance measure from van der Marel and Guhathakurta (2008), and a more accurate Cepheid-based distance measure from Li et al. (2021). We also consider two different M31 proper-motion measurements: Hubble Space Telescope (*HST*)-based proper motions from van der Marel et al. (2012a), and a more recent *Gaia* early Data Release 3 (eDR3)-based proper-motion measure from Salomon et al. (2021).

We have split these measurements into three compiled data sets:

vdMG08 Dist. + HST PM: the M31 distance measure from van der Marel and Guhathakurta (2008) and *HST* proper motions from van der Marel et al. (2012a), the same data set as used to constrain the LG mass via the Timing Argument in van der Marel et al. (2012a)

Cepheid Dist. + Gaia PM: a compilation of more recent M31 kinematic measurements, including a more precise Cepheid-based distance measure to M31 (Li et al., 2021) and updated *Gaia* eDR3 proper motions from (Salomon et al., 2021).

Cepheid Dist. + HST PM: a hybrid data set with the Cepheid-based distance measure to M31 and the *HST*-based proper-motion measurement (Li et al., 2021; van der Marel et al., 2012a).

The *HST*-based proper motions were originally presented in Sohn et al. (2012), and were then corrected for the internal kinematics and space motion of M31 in van der Marel et al. (2012a), from which we used the "Weighted Average" heliocentric velocities in Table 3.[2] The *Gaia*-based M31 proper-motion measurement is slightly larger than the *HST* proper motion

---

[2]Note that the referenced papers actually report velocity components and uncertainties: To transform from velocity back to proper motions, we divide out the adopted distance and deconvolve the distance uncertainty to obtain proper motions and uncertainties of $\mu_{\alpha^*} = 34.30 \pm 8.25$ mas yr^{-1} and $\mu_\delta = -20.22 \pm 7.71$ mas yr^{-1}.

Table 2.1: Observational data sets used for comparison throughout analysis and their references. Each value is measured for M31 with respect to the sun. D is the distance, v_{rad} is the radial velocity, and $(\mu_\alpha^*, \mu_\delta)$ are proper motions in RA cosdec and Decl. $\boldsymbol{x}_\odot = (x, y, z)$ and $\boldsymbol{v}_\odot = (\mathrm{U_{pec}}, \mathrm{V_{pec}} + \mathrm{V_0}, \mathrm{W_{pec}})$ are the position of the Sun and the solar motion with respect to the Galactic center, with the x-axis pointing from the projection of the Sun on the disk towards the Galactic center, and the z-axis pointing in the direction of the North Galactic Pole. t_{peri} is the time elapsed since the last pericenter of the M31 Keplerian orbit, which in this case is the age of the Universe.

	vdMG08 Dist. + HST PM	Cepheid Dist. + Gaia PM	Cepheid Dist. + HST PM
D [kpc]	770 ± 40[a]	761 ± 11 kpc[f]	761 ± 11[f]
v_{rad} [km s^{-1}]	-301 ± 1[b]	-301 ± 1[b]	-301 ± 1[b]
μ_{α^*} [μas yr^{-1}]	34.30 ± 8.25[c]	48.98 ± 10.47[g]	34.30 ± 8.25[c]
μ_δ [μas yr^{-1}]	-20.22 ± 7.71[c]	-36.85 ± 8.03[g]	-20.22 ± 7.71[c]
$\boldsymbol{x}_\odot$ [kpc]	$(-8.29, 0, 0)$[d]	$(-8.122, 0, 20.8)$[h]	$(-8.122, 0, 20.8)$[h]
$\boldsymbol{v}_\odot$ [km s^{-1}]	$(11.1, 251.54, 7.25)$[d]	$(12.9, 245.6, 7.78)$[i]	$(12.9, 245.6, 7.78)$[i]
t_{peri} [Gyr]	13.75 ± 0.11[e]	13.801 ± 0.024[j]	13.801 ± 0.024[j]

a. van der Marel and Guhathakurta (2008), b. Courteau and van den Bergh (1999), c. van der Marel et al. (2012a), d. Schönrich et al. (2010); McMillan (2011), e. Jarosik et al. (2011), f. Li et al. (2021), g. Salomon et al. (2021), h. Gravity Collaboration et al. (2018); Bennett and Bovy (2019), i. Drimmel and Poggio (2018), j. Planck Collaboration et al. (2020)

of M31, leading to an increased implied transverse velocity that, a priori, should lead to a higher inferred LG mass compared to the more radial orbit implied by the *HST* proper motions. See Table 2.1 for numerical values used in each of these data sets.

2.2.3 Bayesian Inference

We construct a likelihood function, $\mathcal{L}$, to quantify the probability of measuring the observed quantities $\boldsymbol{y} = \{D, v_{\mathrm{rad}}, \mu_\alpha^*, \mu_\delta, t_{\mathrm{peri}}\}$ given a Timing Argument model with parameters $\boldsymbol{\theta} = (M_{\mathrm{LG}}, a, e, \eta, \alpha)$. Here, D the distance to M31, v_{rad} the radial velocity of M31, μ_α^* and μ_δ the proper-motion components, and t_{peri} the time since last pericenter. The parameter vector $\boldsymbol{\theta}$ contains M_{LG} the total mass of the LG, a the semimajor-axis, e the eccentricity, η the present value of the eccentric anomaly, and α a nuisance parameter discussed in detail later in this section. We assume that the measurements are independent and have Gaussian uncertainties such that the likelihood function is a product:

$$\mathcal{L} = p(\boldsymbol{y}|\boldsymbol{\theta}) = \prod^n \frac{1}{\sqrt{2\pi}\sigma_n} \exp\left[-\frac{1}{2}\frac{(y_n - \tilde{y}_n(\boldsymbol{\theta}))^2}{2\sigma_n^2}\right] \tag{2.9}$$

where n indexes the elements of the data vector, σ_n is the corresponding uncertainty for the nth data element, and $\tilde{y}_n(\boldsymbol{\theta})$ is the model-predicted value for a given data component.

We then adopt prior probability distribution functions (pdfs) for the parameters and use these pdfs to compute the posterior pdf over the parameters given the data in order to generate samples from the posterior pdf using a Markov Chain Monte Carlo (MCMC) method. In order to recover the estimated mass distribution, we marginalize over all other model parameters.

In detail, we first use the four Timing Argument parameters to compute the present-day separation between the MW and M31 halos and their relative radial and tangential velocities as defined in Equations 2.1–2.4. These velocity components represent the relative velocity M31 would have as observed from the center of an unperturbed MW halo. We then use the measured "travel velocity" of the MW disk, $\boldsymbol{v}_{\mathrm{travel}}$, to find the relative velocity of M31 with respect to the center of the moving MW disk (i.e., a moving MW Galactocentric frame). We finally transform from this Galactocentric frame to a heliocentric reference frame moving with the solar system barycenter (i.e., ICRS coordinates). At this final stage, we must introduce an additional nuisance parameter α that represents the orientation of the MW–M31 orbital plane as it intersects the tangent plane located at the sky position of M31 as viewed from the MW disk center. This parameter is needed to convert from the two-dimensional velocity components given by Equations 2.3–2.4 to the three-dimensional velocity components represented by the two proper-motion components and the radial velocity of M31. However, we stress that this position angle has no impact on the fundamental dynamical parameters and is only used for coordinate transformations.

We specify this model using the `Python` probabilistic programming package `pymc3` (Salvatier et al., 2016) and use the No-U-Turn Sampler (NUTS) (Homan and Gelman, 2014) implemented in `pymc3` to generate samples from this posterior pdf, given data from each of the data sets defined in Table 2.1. We sample over the parameters LG mass M_{LG}, the present-day MW–M31 halo separation r, log eccentricity $\ln(1 - e)$, eccentric anomaly η, and the orbital plane orientation nuisance parameter α. Our adopted prior pdfs are defined in Table 2.2. For each data set, we run the sampler with four chains for 4000 tuning steps and 40,000 draws.

Table 2.2: A description of our adopted prior probability distribution functions over the Timing Argument model parameters. Here, $\mathcal{U}(a, b)$ represents a uniform distribution over the domain (a, b), and $\mathcal{N}_T(\mu, \sigma)$ represents a truncated Normal distribution with mean μ and standard-deviation σ. We truncate the mass prior pdf to the range $(0.5, 20) \times 10^{12} \, \mathrm{M_\odot}$ and the distance prior pdf to the range $(100, 10^4)$ kpc.

Prior	Description
M_{LG}: $\mathcal{N}_T(4.5, 3) \times 10^{12} \, \mathrm{M_\odot}$	Mass of the Local Group
r: $\mathcal{N}_T(700, 100)$kpc	Distance from M31 to $\mathrm{MW_{disk}}$
$\ln(1 - e)$: $\mathcal{U}(-10, 0)$	Eccentricity (close to 1)
η: $\mathcal{U}(-\pi, \pi)$	Eccentric anomaly
α: $\mathcal{U}(-\pi, \pi)$	Position angle of M31 orbital plane from MW disk center

2.3   Results: Local Group Mass Estimates

We use a Bayesian implementation of a Timing Argument model to quantify the impact of the measured travel velocity of the MW disk from Petersen and Peñarrubia (2021) on the estimated mass of the LG, as well as other orbital parameters such as the distance between M31 and the MW. We compute convergence statistics using ArviZ (Kumar et al., 2019) for all MCMC runs and find that the maximum Gelman–Rubin convergence statistic is ≤ 1.01 for all parameters and each data set (Gelman and Rubin, 1992). The mean inferred parameter values and their 68% credible regions from the sampled posterior pdfs for each data set are presented in Table 2.3. These results are also shown in Figure 2.2, again displaying the 68% credible regions of the LG mass, M_{LG} and eccentricity, e (lower left panel). The upper-left panel shows the marginal posterior pdfs over LG mass for each of the data sets (histogram curves) and with 68% credible regions plotted for two prior LG mass measurements (gray shaded bands). We note that these values are for reference only, as we currently do not account for other known sources of bias in the TA model – such as a cosmological constant or cosmic bias – that may yield more accurate values.

We find that the addition of the travel velocity of the MW disk systematically decreases the inferred LG mass and eccentricity of the orbit compared to models that do not include the travel velocity of the MW disk. We also find that the inferred mass is larger and the LG orbit is less eccentric when using the (larger) *Gaia* proper-motion of M31. For all data sets, the eccentricity of the decreases by $\sim 3 - 5\%$. However, we find that the inferred orbital

Table 2.3: Mean inferred parameter values and the 68% credible region of the sampled posterior region for each data set. Here, M_{LG} is the mass of the Local Group, e is the eccentricity of the MW–M31 orbit, r is the distance between the centers of the MW and M31 halos, η is the eccentric anomaly (a proxy for the phase of the orbit), and α is a nuisance parameter representing the angle between the orbital plane of MW–M31 and the tangent plane located at the sky position of M31 as seen from the center of the MW disk.

Parameter	vdMG08 Dist. + HST PM	Cepheid Dist. + Gaia PM	Cepheid Dist. + HST PM
M_{LG}	$3.98^{+0.6}_{-0.5}$	$4.54^{+0.8}_{-0.6}$	$4.05^{+0.5}_{-0.3}$
e	$0.92^{+0.1}_{-0.1}$	$0.84^{+0.1}_{-0.1}$	$0.92^{+0.1}_{-0.1}$
r	$777.72^{+36.6}_{-36.0}$	$765.17^{+10.9}_{-10.9}$	$765.44^{+10.8}_{-10.9}$
η	$-2.14^{+0.05}_{-0.04}$	$-2.08^{+0.04}_{-0.04}$	$-2.11^{+0.03}_{-0.03}$
α	$2.97^{+0.8}_{-0.8}$	$1.42^{+0.6}_{-0.5}$	$2.96^{+0.8}_{-0.8}$

eccentricity is consistent with a radial orbit.

Figure 2.3 gives a summary of our key results, showing the behavior of the inferred LG mass and eccentricity as a function of the travel velocity. As the travel velocity increases from $\boldsymbol{v}_{\mathrm{travel}} = 0$ to $\boldsymbol{v}_{\mathrm{travel}} = 32 \pm 4$ km s^{-1}, shown by the vertical black line and gray shaded regions, the mass and eccentricity both decrease, with the effect on the mass drastically changing by up to $\sim 0.5 \times 10^{12}\,\mathrm{M}_\odot$ and the MW–M31 orbit becoming more circular.

2.4 Discussion

2.4.1 Comparing Recent Measurements of the Local Group Mass

There have been two primary pathways toward measuring the mass of the LG: measure the masses of MW and M31 individually and add them, or go after the total mass directly with LV dynamics, the Timing Argument, or cosmological simulations.

Historically, the total mass estimates have been much larger than the sum of the individual MW and M31 masses: typical total LG masses are upwards of $4 \times 10^{12}\,\mathrm{M}_\odot$, while the sum of independent MW+M31 mass measures result in a total mass closer to $2 - 2.5 \times 10^{12}\,\mathrm{M}_\odot$, as can be seen in the collection of previous mass estimates for the LG, M31, and the MW in Table 2.4. It is not surprising that there are many discrepancies between the total and summed values of the LG mass, since MW+M31 (i.e., individual summed) mass estimates often cannot measure the full extent of the distribution of dark matter within each galaxy, let alone in the LG, and thus must extrapolate in regions where there may be large uncertainties.

There have been a few exceptions in the trend of high total mass measurements, namely in Diaz et al. (2014) and Peñarrubia et al. (2016). Diaz et al. (2014) utilize the fact that the LG momentum should balance to zero in the frame of the LG barycenter to determine the total mass of the LG, as well as the mass ratio between M31 and the MW. Using the LG barycenter, indicated by a set of 17 LG satellites at $> 350\,\mathrm{kpc}$ from the MW and M31, and the velocities of M31 and the MW with respect to the barycenter, they found a LG mass of $2.5 \pm 0.4 \times 10^{12}\,\mathrm{M_\odot}$, and a mass ratio $\mathrm{M_{M31}/M_{MW}} > 2.29$. The impact of the LMC and M33 are absorbed by assuming they contribute to the masses of their host galaxies. However, the recent measurement of the MW travel velocity will change the measured barycenter and velocities of the MW, M31, and the LG satellites, though it is unclear how this would affect the total mass in their analysis.

Additionally, Peñarrubia et al. (2016) found a Local Group mass of $\sim 2.64 \pm 0.4 \times 10^{12}\,\mathrm{M_\odot}$, which is significantly lower than our findings, although this constraint combines the Timing Argument dynamics of the M31–MW system in addition to the observed kinematics of 35 LV galaxies. They parameterize the offset of the LMC+MW barycenter from a MW-only barycenter as a function of the mass ratio between the LMC and MW, and find that the LMC likely has $\sim 25\%$ of the mass of the MW halo, resulting in a large shift in the barycenter of the LMC+MW. The recovered mass using only the dynamics of the LV galaxies was quite low ($\sim 2 \times 10^{12}\,\mathrm{M_\odot}$), though including the Timing Argument dynamics of the MW–M31 system increased their recovered total mass to $\sim 2.64 \pm 0.4 \times 10^{12}\,\mathrm{M_\odot}$.

Our TA+$\boldsymbol{v}_{\mathrm{travel}}$ LG mass estimates are consistent with a number of other recent studies that estimate the mass of the LG through dynamical methods. For example, we find agreement with the previous Timing Argument model of van der Marel et al. (2012a) which found a total mass of $4.27 \pm 0.45 \times 10^{12}\,\mathrm{M_\odot}$ (neglecting for cosmic bias and scatter) using the same values for the distance and velocity of M31 as in our *vdMG08 Dist. + HST PM* data set.

In two N-body cosmological simulations, Millenium-WMAP7 and MilleniumII, Zhai et al. (2020) identified pairs of stellar analogs to the MW and M31, then applied a series of kinematic cuts on the separation, isolation, and velocities of the pair to determine LG analogs. They find stellar and dynamical LG analogs on mostly radial orbits have total masses of $4.4^{+2.4}_{-1.5} \times 10^{12}\,\mathrm{M_\odot}$, which is consistent with our findings for each data set. They also find

that low-ellipticity orbits (where $v_{\rm rad} \sim v_{\rm tan}$), result in a higher LG mass, M31 mass, and MW mass, reporting $6.6^{+2.7}_{-1.5} \times 10^{12}\,\mathrm{M}_\odot$, $3.8^{+2.8}_{-1.8} \times 10^{12}\,\mathrm{M}_\odot$, and $2.5^{+2.2}_{-1.4} \times 10^{12}\,\mathrm{M}_\odot$, respectively. We find that the ellipticity of the orbit decreases dramatically with larger travel velocities; however, in contradiction to Zhai et al. (2020), we find that this leads to a lower total LG mass.

Additionally, Benisty et al. (2022) recently modeled the contribution of the LMC-induced shift in the barycenter of the MW and used the Timing Argument to place constraints on the LG mass while removing the impact of the LMC. More specifically, they estimate the contribution of the reflex motion of the MW disk to the observed velocity vector of M31 by modeling the orbital history of the MW–M31 system and the MW+LMC–M31 system. The impact of the LMC on the mass measurements of the LG thus depend on the orbital and mass models of the LMC about the MW. This is in contrast to our work, which need make no assumption about the mass of the LMC, its orbital history, or the merger history of the MW. Upon implementing the Timing Argument, including a cosmological constant, and removing the LMC-induced reflex motion, they find a LG mass of $5.6^{+1.6}_{-1.2} \times 10^{12}\,\mathrm{M}_\odot$, which is roughly 25% larger than our findings, and that accounting for cosmic bias & scatter lowers the mass by an additional 40% to $3.4^{+1.4}_{-1.1} \times 10^{12}\,\mathrm{M}_\odot$, 25% lower than our findings. However, they find that, in general, inclusion of the motion of the MW disk due to the interaction with the LMC lowers the LG mass by $\sim 10\%$, which is consistent with our finding of a reduction in the total LG mass by $\sim 10 - 12\%$.

A notable difference between this study and Benisty et al. (2022) is the method by which the reflex motion of the MW disk is accounted for. Rather than relying on accurately simulating the reflex motion of the disk, we let the travel velocity of the MW disk introduce a coordinate transformation (boost) of the measured velocity vectors of M31, and fit for the model parameters given the observable data. This method allows us to avoid model uncertainties in the mass profiles of each galaxy in the orbital models of the interaction between the MW, M31, and the LMC. Additionally, using the measured travel velocity also allows us to innately account for possible additional contributions to the present-day, instantaneous travel velocity induced by the extensive merger history of the MW in a robust way, without the need to simulate the entire interaction history.

Table 2.4: A collection of previous mass measurements from LG dynamics discussed in the text focusing on previous Timing Argument results.

Mass	Method	Result (10^{12} $M_\odot$)	Citation
	TA	3.6	Lynden-Bell 1981
	TA (radial + cosmo sim calibration)	5.27	Li and White 2008
	TA only	4.27±0.45	van der Marel et al. 2012a
	TA (3D + cosmic bias and scatter)	4.93±1.63	van der Marel et al. 2012a
	LG Dynamics	2.5 ± 0.4	Diaz et al. 2014
	LV Galaxies + TA + Λ	2.64±0.4	Peñarrubia et al. 2016
	Machine Learning	4.9 ± 0.8	McLeod et al. 2017
M_{LG}	Machine Learning (+large M31 transverse motion)	3.6 ± 0.3	McLeod et al. 2017
	Cosmological Sims	$4.4^{+2.4}_{-1.5}$	Zhai et al. 2020
	Cosmological Sims (likelihood-free inference)	$4.6^{+2.3}_{-1.8}$	Lemos et al. 2021
	TA + Λ + Cosmological Sims	$4.75^{+2.22}_{-2.41}$	Hartl and Strigari 2022
	TA + Λ + LMC	$5.6^{+1.6}_{-1.2}$	Benisty et al. 2022
	TA + Λ + cosmic biad + LMC	$3.4^{+1.4}_{-1.1}$	Benisty et al. 2022
	TA + $v_{\mathbf{travel}}$ (Cepheid + HST)	$\mathbf{4.0^{+0.5}_{-0.3}}$	**Chamberlain et al. 2023 (this work)**
	TA + $v_{\mathbf{travel}}$ (Cepheid + Gaia)	$\mathbf{4.5^{+0.8}_{-0.6}}$	**Chamberlain et al. 2023 (this work)**
	Kinematics of M31 Sats	1.4 ± 0.4 (<300 kpc)	Watkins et al. 2010
	Giant Stellar Stream	$2.00^{+0.52}_{-0.41}$	Fardal et al. 2013
	LG Dynamics	1.7 ± 0.3	Diaz et al. 2014
	Local Hubble Flow	1.33 ± 0.4	Peñarrubia et al. 2016
M_{M31}	M31 Orbital Ang. Mom.	$1.37^{+1.39}_{-0.75}$	Patel et al. 2017b
	Cosmological Sims	$1.0 - 2.0$	Carlesi et al. 2017
	Cosmological Sims	$2.5^{+1.3}_{-1.1}$	Zhai et al. 2020
	Machine Learning	$2.3 - 2.5$	Villanueva-Domingo et al. 2021
	Machine Learning (+velocity information)	$2.2 - 2.5$	Villanueva-Domingo et al. 2021
	Kinematics of LG sats	1.4 ± 0.3 (<300 kpc)	Watkins et al. 2010
	LG Dynamics	0.8 ± 0.5	Diaz et al. 2014
	Local Hubble Flow	1.04 ± 0.26	Peñarrubia et al. 2016
	LMC Orbital Ang. Mom.	$1.02^{+0.77}_{-0.55}$	Patel et al. 2017b
M_{MW}	Cosmological Sims	$0.6 - 0.8$	Carlesi et al. 2017
	MW Sats	$0.96^{+0.29}_{-0.28}$	Patel et al. 2018
	Cosmological Sims	$1.5^{+1.4}_{-0.7}$	Zhai et al. 2020
	Machine Learning	$1.0 - 1.3$	Villanueva-Domingo et al. 2021
	Machine Learning (+velocity information)	$2.3 - 2.6$	Villanueva-Domingo et al. 2021

2.4.2 Additional Sources of Bias to the Timing Argument

Given the simplicity of the Timing Argument dynamical model — in particular, the assumption that the MW and M31 are point masses with constant masses — it is reasonable to wonder whether this methodology provides unbiased estimates of the true LG mass. An early study of a dark-matter-only cosmological simulation found that the Timing Argument applied to pairs of galaxies did provide unbiased estimates of the sum of masses of the pairs (Li and White, 2008). However, more recently it was found that conditioning on LG analogs with similar radial and tangential velocities to the MW and M31 leads to slightly biased (overestimated) inferred total masses of those systems (González et al., 2014; Hartl and Strigari, 2022). In this work, we do not attempt to "correct" our inferred LG masses for this cosmic bias effect, because it is unclear whether cosmological simulations accurately reproduce the detailed properties of LG systems. Accounting for this effect would likely lower our reported LG mass measurements. However, as we have shown, the existence of a reflex motion of the MW disk as a response to the MW's interaction with its satellite population decreases is an additional perturbation to the TA that must be considered in future studies alongside cosmic bias and a cosmological constant.

2.4.3 Impact of Travel Velocity on Inferred Dynamics of the Local Group

The existence of the travel velocity of the MW disk results in measurable differences in the estimated mass of the LG through the Timing argument. These results are consistent with Erkal et al. (2020), who find that neglecting the LMC-induced reflex motion of the MW can result in masses that are overestimated by up to 50%. As shown in our results above, neglecting this motion at its currently measured value of $\boldsymbol{v}_{\text{travel}} = 32 \pm 4\text{km s}^{-1}$ (Petersen and Peñarrubia, 2021) leads to LG masses that are overestimated by $\sim 30\%$. However, both the magnitude and *direction* of the travel velocity are directly tied to the inferred mass of the LG. As it is currently measured, the (highest likelihood) direction of $\boldsymbol{v}_{\text{travel}}$ is $\sim 60°$ from the sky position of M31, meaning that the travel velocity impacts the conversion of both M31's observed proper motion and radial velocity from a Heliocentric reference frame to the "outer halo" reference frame used above. At fixed magnitude, if the true apex of the travel velocity

motion is closer (farther) to M31's sky position, it would primarily affect the radial velocity (proper motions).

There is reason to believe that the recently measured MW disk travel velocity could be a lower bound on the true value, which could be up to a factor of ∼2–3 higher than the currently measured value. Using an idealized simulation of an equilibrium dark matter halo that has a recent merger with an LMC-like halo, Garavito-Camargo et al. (2021) showed that stellar halo tracers at different distances from the MW disk center may result in different measured travel velocities. While this simulation does not span previous mergers in the MW's history, it gives a good first-order approximation of what we may expect to observe. At fixed apex direction, a larger travel velocity would correspond to a lower inferred LG mass. Figure 2.3 shows the effect of increasing the measured travel velocity magnitude up to these predicted values and the impact on the inferred mass of the LG for each of the data sets used in this work (see Section 2.2.2). The vertical lines in this figure show the LMC-induced travel velocities that are predicted for three tracer distances in simulations from Garavito-Camargo et al. (2021). Thus, future measurements of the travel velocity of the disk that use tracers at larger distance around the MW stellar halo will likely lead to a lower inferred LG mass. We note again that the value of the eccentricity is derived assuming a matter-only universe (i.e., we neglect other cosmological effects in the orbit computation, as discussed above).

2.4.4   Improved M_{LG} Constraints from Future Observations

The biggest source of uncertainty in our empirically inferred LG mass M_{LG}, currently comes from the proper-motion measurements, which have signal-to-noise ratios of just 3–4. Future data releases from the *Gaia* Mission (Gaia Collaboration et al., 2016) will lead to more precise mean proper motions of M31 and thus more precise Timing Argument constraints on the LG mass. For example, between *Gaia* eDR3 and the end of the extended (10 yr) mission, the expected individual-source proper-motion precision improvement for a $G = 20$ source (i.e. an upper giant-branch star in M31) is a factor of ∼6. Naïvely scaling the proper-motion uncertainties of M31 as measured with *Gaia* (Salomon et al., 2021) by a factor of 6 leads to a ∼ 2× improvement in the M_{LG} precision. Of course, the true improvement of the mean M31 proper motion with improved individual source kinematics could be even better than linear

because more sources will be detected and usable in the measurement.

2.4.5 Reflex Motion of M31

While M31 has a massive satellite (M33) of comparable mass ratio to the MW–LMC system, we do not expect there to be a significant reflex velocity of M31's disk relative to its equivalent outer halo reference frame. Recent work predicts that M33 is likely on first infall into the M31 halo and has a much larger orbital pericenter than the MCs (e.g., Patel et al., 2017a). Additionally, M31 has likely experienced other significant mergers, as evidenced by the double nucleus and Giant Southern Stream (e.g. Ibata et al., 2001; Font et al., 2006), but these were likely lower mass-ratio mergers (e.g. Gilbert et al., 2019; Milošević et al., 2022) and thus will have less of an impact on the bulk motion of the M31 disk. Given current knowledge of the M31 system and uncertainties in the orbital histories of its most massive satellites, here we neglect the reflex motion of the M31 disk. However, a measurement or upper limit on the M31 disk travel velocity would enable further unbiased constraints on the LG mass.

2.4.6 MW & M31 Individual Masses

Reconciling techniques that compute the LG mass from the summed MW+M31 mass and from the Timing Argument is not straightforward, but the two approaches are complimentary. Future measurements of the travel velocity at large Galactocentric distances will likely exceed current measurements (see Section 2.4.3), which directly implies a lower LG mass and may improve agreement between these two general methods for estimating the LG mass. Since constraints on the MW mass consistently find a mass of $\sim 10^{12}\,\mathrm{M_\odot}$, if not slightly higher (see for reference Table 2.4), our mass limits from the Timing Argument may begin to place meaningful upper limits on the mass of the M31 system.

2.4.7 The Circularity of the MW–M31 Orbit

The Timing Argument is highly sensitive to the tangential motion of M31, and larger proper motions will generically lead to lower eccentricities and higher inferred LG masses. Recent *Gaia* proper motions of M31 suggest the orbit of MW–M31 is less radial than previously

believed (van der Marel et al., 2019; Salomon et al., 2021). Neglecting the travel velocity ($\boldsymbol{v}_{\text{travel}} = 0$ in above plots), we find that proper motions from *HST* (van der Marel et al., 2012a) are consistent with a highly radial orbit $e \sim 0.96$, while proper motions from *Gaia* (Salomon et al., 2021) result in a slightly lower eccentricity of $e \sim 0.88$. As seen in Figure 2.3, we find that as the travel velocity increases, the inferred eccentricity of the MW–M31 orbit decreases. However, contrary to expectations, we find that the inferred LG mass *also* decreases. This implies that the velocity contribution to the relative and transverse velocity of M31 is dominant to the change in eccentricity.

Additionally, studies of the Bolshoi *N*-body cosmological simulation by Forero-Romero et al. (2013) find that typical LG analogs, when selected via mass and isolation criteria, do not have completely radial orbits. As with studies that measure a higher transverse velocity for M31, and thus a slightly less-radial orbit (van der Marel et al., 2019; Salomon et al., 2021), we find that the decrease in the eccentricity due to the measured travel velocity makes the LG less eccentric and, thus, more cosmologically typical.

2.5 Summary and Conclusions

Recent measurements of tracers in the outer MW stellar halo ($40 < r < 120\,\text{kpc}$) by Petersen and Peñarrubia (2021) measure an instantaneous differential "travel velocity" of the MW disk compared to the outer stellar halo. The travel velocity has been inferred as primarily due to the response of the MW halo to the recent infall of the LMC (as shown in e.g. Gómez et al., 2015; Garavito-Camargo et al., 2019; Erkal et al., 2019; Cunningham et al., 2020; Petersen and Peñarrubia, 2020; Garavito-Camargo et al., 2021). In this work, we study the effect of the travel velocity on the inferred LG mass from the Timing Argument empirically for the first time. This allows us to avoid modeling uncertainties in the LMC orbital history and mass profile as well as uncertainties in the MW merger history.

We also consider three compilations of kinematic data for the distance and proper motion of M31, and find a decrease in the inferred mass compared to non-travel-velocity TA models. For each data set, as follows: [3]

---

[3] Errors correspond to the 68% credible regions about the median LG mass from the MCMC sampled posterior pdfs of our model parameters.

- For the "*vdMG08 Dist. + HST PM*" data set – the van der Marel and Guhathakurta (2008) distance and *HST* proper-motion measurements (Sohn et al., 2012; van der Marel et al., 2012a) – we find a LG mass of $M_{\rm LG} = 3.98^{+0.63}_{-0.47} \times 10^{12}$ $M_\odot$ (including the measured travel velocity), and of $M_{\rm LG} = 4.49^{+0.47}_{-0.42} \times 10^{12}$ $M_\odot$ when $\boldsymbol{v}_{\rm travel}{=}0$. Thus, the inclusion of the that the travel velocity decreases the inferred LG mass by 11.36%.

- For the "*Cepheid Dist. + HST PM*" data set – an updated Cepheid distance measurement from Li et al. (2021) and the same *HST* PMs from above – we find a LG mass of $M_{\rm LG} = 4.05^{+0.51}_{-0.34} \times 10^{12}$ $M_\odot$ (including the measured travel velocity), and of $M_{\rm LG} = 4.61^{+0.42}_{-0.22} \times 10^{12}$ $M_\odot$ when $\boldsymbol{v}_{\rm travel}{=}0$. Thus, the inclusion of the that the travel velocity decreases the inferred LG mass by 12.01%.

- For the "*Cepheid Dist. + Gaia PM*" data set – a combination of the more recent Cepheid distance and latest *Gaia* proper motion measurements of M31 (Li et al., 2021; Salomon et al., 2021) – we find a LG mass of $M_{\rm LG} = 4.54^{+0.77}_{-0.56} \times 10^{12}$ $M_\odot$ (including the measured travel velocity), and of $M_{\rm LG} = 5.09^{+0.72}_{-0.48} \times 10^{12}$ $M_\odot$ when $\boldsymbol{v}_{\rm travel}{=}0$. Thus, the inclusion of the that the travel velocity decreases the inferred LG mass by 10.88%.

Our conclusions can be summarized as follows:

- **The measured travel velocity of the MW disk directly implies a reduced LG mass from the Timing Argument.** For the measured travel velocity of 32 ± 4km s^{-1} from Petersen and Peñarrubia (2021), the inferred LG mass is $\sim 10 - 15\%$ lower than a system with a static MW halo ($\boldsymbol{v}_{\rm travel} = 0$). Using the same distance and proper motions as in the Timing Argument model of van der Marel et al. (2012a), we find that the inclusion of the travel velocity yields a reduction in the LG mass of $\sim 0.3 \times 10^{12}\,M_\odot$.

- **Higher travel velocity measurements will yield lower LG masses.** Simulations (Garavito-Camargo et al., 2021) suggest that tracers at large Galactocentric distances (60–100 kpc) will yield larger measurements of the travel velocity. If the travel velocity is measured to be larger based on tracers at larger Galactocentric distances, this will result in a decrease in the inferred LG mass by an additional $5 - 12\%$.

- **The inferred eccentricity of the MW–M31 orbit is decreased by 3–5% when accounting for the measured travel velocity.** With a larger measured travel velocity, the inferred MW–M31 orbit would be less radial. The inferred eccentricity decreases by up to $\sim 50\%$ for the largest travel velocities we consider ($\boldsymbol{v}_{\text{travel}} = 100 \text{km s}^{-1}$) compared to the static MW-halo model ($\boldsymbol{v}_{\text{travel}} = 0$). Less radial orbits are cosmologically preferred, thus the travel velocity makes the LG more cosmologically typical.

- **Improvements in M31 proper motion measurements will improve Timing Argument mass precision.** With future data releases from the *Gaia* Mission, we expect the proper-motion uncertainties to improve by a factor of $\sim$2–3 for individual sources (and likely more for measurements of the mean proper motions of stellar systems and galaxies like M31). We artificially scaled the proper-motion errors in each data set and find an expected improvement in the uncertainty on the inferred LG mass by a factor of 2–2.5$\times$ (see Section 2.4.4 for more detail).

This study highlights the importance of improved dynamical measurements within the LV in the near future in order to accurately measure the dark matter content of our LG. It is critical to refine our measurements of the proper motion of M31 and to measure the travel velocity of the MW disk with stellar tracers at further Galactocentric distances. These endeavors will (1) further refine estimates of the mass of the Local Group, enabling studies to realistically place the LG in a cosmological context, and (2) permit measurements of the travel velocity induced by the infall of the LMC and other satellite galaxies relative to tracers at large Galactocentric distances, which will establish a firm measurement of the LG mass via the Timing Argument, and thereby place meaningful limits on the individual masses of the M31 and MW galaxy.
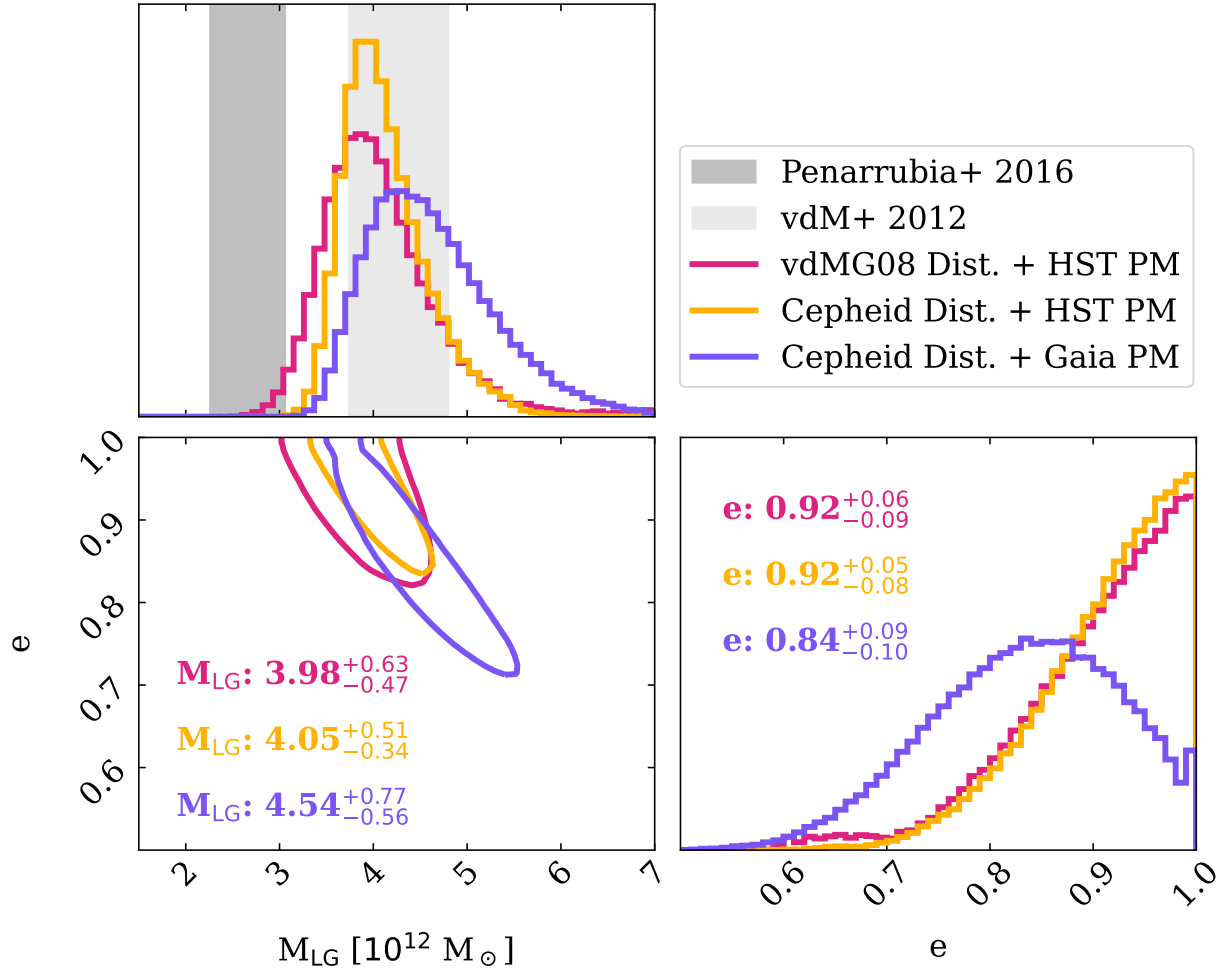
Figure 2.2: Sixty-eight percent credible regions of sampled posterior distributions with three observational data sets for a subset of our model parameters: the total mass of the Local Group (M_{LG}) and the eccentricity of the orbit of M31 about a fixed MW (e). Mean masses (in units of $10^{12}\,\mathrm{M_\odot}$) and eccentricities are reported in the bottom left and right panels along with the 68% credible region for each data set. The shaded regions in the upper left panel are the 68% credible region mass estimates of previous TA studies from van der Marel et al. (2012a) and Peñarrubia et al. (2016). The more radial orbit implied by the van der Marel et al. (2012a) *HST* proper motions leads to a lower inferred M_{LG} and a higher eccentricity, while the larger *Gaia* proper motions of Salomon et al. (2021) yield a more circular orbit, and thus a lower eccentricity and higher mass system.
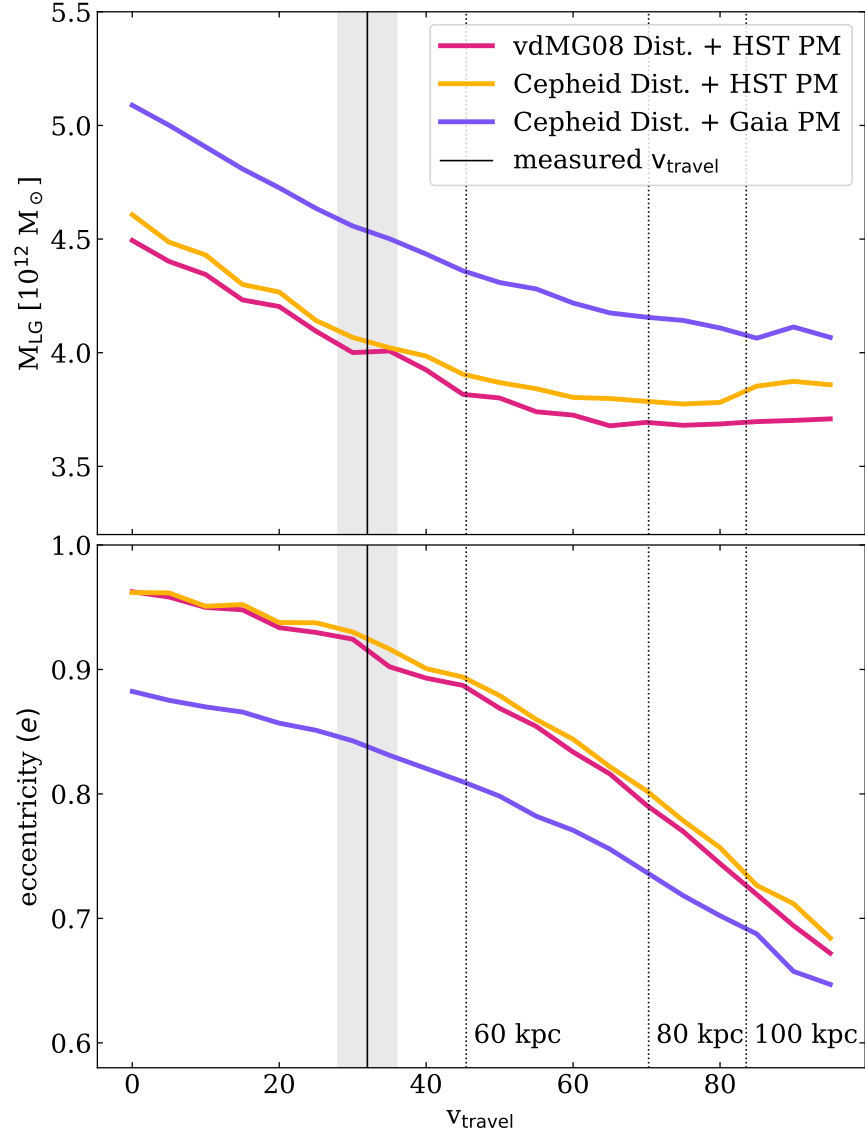
Figure 2.3: Mean inferred Local Group (LG) mass (top) and eccentricity (bottom) as a function of travel velocity magnitude of the MW disk. The larger *Gaia* proper motions (purple) lead to higher transverse motion and thus higher mass and a less eccentric orbit than either of the *HST* proper motion data sets (pink and yellow), though each data set displays the same general trend with increasing travel velocity. The solid vertical line and accompanying shaded region represent the median and 67% confidence interval of the travel velocity measured by Petersen and Peñarrubia (2021) of $v_{\text{travel}} = 32 \pm 4 \text{km s}^{-1}$. The dotted vertical lines represent simulated travel velocities for stellar tracers at different distances in Garavito-Camargo et al. (2021). **The inclusion of the travel velocity of the MW disk systematically lowers the inferred mass and eccentricity of the Local Group** regardless of observational data set. A larger measured travel velocity will yield a lower mass, less radial Local Group.

<center>**Chapter 3**</center>

A Physically Motivated Framework to Compare Pair Fractions of Isolated Low and High Mass Galaxies Across Cosmic Time

This chapter has been published previously as Chamberlain K., Besla G., Patel E., et al. 2024, ApJ, 962, 162 [1]

<center>**Abstract**</center>

Low mass galaxy pair fractions are under-studied, and it is unclear whether low mass pair fractions evolve in the same way as more massive systems over cosmic time. In the era of JWST, Roman, and Rubin, selecting galaxy pairs in a self-consistent way will be critical to connect observed pair fractions to cosmological merger rates across all mass scales and redshifts. Utilizing the Illustris TNG100 simulation, we create a sample of physically associated low mass ($10^8 < \mathrm{M}_* < 5 \times 10^9\ \mathrm{M}_\odot$) and high mass ($5 \times 10^9 < \mathrm{M}_* < 10^{11}\ \mathrm{M}_\odot$) pairs between $z = 0$ and 4.2. The low mass pair fraction increases from $z = 0$ to 2.5, while the high mass pair fraction peaks at $z = 0$ and is constant or slightly decreasing at $z > 1$. At $z = 0$, the low mass major (1:4 mass ratio) pair fraction is $4\times$ lower than high mass pairs, consistent with findings for cosmological merger rates. We show that separation limits that vary with the mass and redshift of the system, such as scaling by the virial radius of the host halo ($r_{\mathrm{sep}} < 1R_{\mathrm{vir}}$), are critical for recovering pair fraction differences between low mass and high mass systems. Alternatively, static physical separation limits applied equivalently to all galaxy pairs do not recover the differences between low and high mass pair fractions, even up to separations of 300 kpc. Finally, we place isolated mass-analogs of Local Group galaxy pairs, i.e., Milky Way (MW)–M31, MW–LMC, LMC–SMC, in a cosmological context, showing that isolated analogs of LMC–SMC-mass pairs and low-separation ($< 50\,\mathrm{kpc}$) MW–LMC-mass

---

[1] Chamberlain et al. (2024)

pairs are $2 - 3\times$ more common at $z \gtrsim 2 - 3$.

3.1   Introduction

Galaxy mergers have been studied in detail as a mechanism for driving galaxy evolution, and have been identified as a trigger of, for example, active galactic nuclei (AGN) (e.g. Hopkins et al., 2008; Treister et al., 2010; Ramos Almeida et al., 2011; Satyapal et al., 2014; Comerford et al., 2015; Glikman et al., 2015; Blecha et al., 2018; Ellison et al., 2019), star formation (e.g. Mihos and Hernquist, 1996; Di Matteo et al., 2008; Ellison et al., 2011; Hopkins et al., 2013; Patton et al., 2013; Martin et al., 2017; Hani et al., 2020; Patton et al., 2020; Martin et al., 2021), and changes in morphology (e.g. Conselice, 2003; Lotz et al., 2008; Casteels et al., 2014; Patton et al., 2016; Bignone et al., 2017; Rodriguez-Gomez et al., 2017; Martin et al., 2018; Jackson et al., 2019; Snyder et al., 2019; Jackson et al., 2022; Guzmán-Ortega et al., 2023). Constraining the merger rate for galaxies is critical for quantifying the importance of mergers for galaxy evolution and testing predictions for hierarchical assembly in cold dark matter theory (e.g. Stewart et al., 2009; Hopkins et al., 2010b; Rodriguez-Gomez et al., 2015).

In practice, merger rates cannot be measured straightforwardly from observations and, rather, are calculated by converting the observed frequency of a galaxy merger signature (i.e., asymmetry, concentration, pair fraction, etc.) to a merger rate using an observability timescale (e.g. Lotz et al., 2011). However, morphological signatures of mergers are often caused by non-merger phenomena. For example, low mass galaxies are more commonly morphologically disturbed by fly-bys and non-merger interactions than by mergers (Martin et al., 2021), and star-forming galaxies at high redshift tend to be clumpy and asymmetric even in isolation (Wuyts et al., 2013). Additionally, detection of these signatures can be strongly dependent on image depth or galaxy stellar mass, and identifying tidal features that rely on human classifications may be unreliable (Martin et al., 2022).

Pair fractions, on the other hand, can be calculated independently of morphological information, and thus offer a more robust method of observationally quantifying merger rates across cosmic time. Pair fractions of high mass ($M_* \gtrsim 10^{10}\,\mathrm{M_\odot}$) galaxies have been well studied across cosmic time both observationally (e.g. Patton et al., 2002; Lin et al., 2004, 2008; Lotz et al., 2011; Ferreras et al., 2014; Man et al., 2016; Duncan et al., 2019) and

theoretically (e.g. Rodriguez-Gomez et al., 2015; Snyder et al., 2017, 2023), with theoretical studies typically done in projection for comparison to observational campaigns[2]. Low mass galaxy pairs ($10^8 < M_* < 5 \times 10^9\,\mathrm{M_\odot}$) have been studied at low redshift (e.g. Stierwalt et al., 2015; Pearson et al., 2016; Besla et al., 2018; Paudel et al., 2018; Luber et al., 2022), but are less well understood across cosmic time owing to the difficulty in observing faint systems outside of the Local Volume. However, JWST (Gardner et al., 2006), as well as the next generation of deep and wide-field surveys from Rubin Observatory[3] (Ivezić et al., 2019) and Roman Space Telescope[4] (Spergel et al., 2015), will significantly revolutionize our ability to identify such systems at high redshift ($z \gtrsim 10$) (Behroozi et al., 2020) and in abundance at lower redshift ($z \lesssim 6$) (Robertson et al., 2019a,b).

There are reasons to believe that low mass and high mass pairs evolve differently as a function of time. For example, semi-empirical and cosmological studies find that galaxy merger rates vary both with redshift and the mass of the most massive galaxy of the pair (see, e.g. Guo and White, 2008; Stewart et al., 2009; Hopkins et al., 2010b; Rodriguez-Gomez et al., 2015; Martin et al., 2021). It is thus reasonable to assume that the pair fractions of these two mass scales reflect these evolutionary differences as well.

The redshift evolution of low and high mass pair fractions has not yet been studied in simulations in a self-consistent way, where high mass and low mass pairs are selected from simulations using otherwise equivalent selection criteria. We aim to characterize the redshift behavior of pair fractions of low mass and high mass pairs, independent of environmental and projection effects, and to create a robust framework in which to fairly compare pair fractions of different mass scales across cosmic time.

In particular, we take the approach of consistently selecting physically associated pairs of low mass ($10^8 < M_* < 5 \times 10^9\,\mathrm{M_\odot}$) and high mass ($5 \times 10^9 < M_* < 10^{11}\,\mathrm{M_\odot}$) galaxies. Specifically, we identify major ($1 - 1/4$) and minor ($1/10 - 1/4$) stellar mass ratio pairs from $z = 0$ to $z = 4.2$ in the IllustrisTNG cosmological simulation, TNG100. We require that pairs are part of the same Friends of Friends (FoF) group and that no other more massive

---

[2]The studies cited here have limits on the projected separation of their sample, such that the projected separations range between 5 kpc and ~ 140 kpc.

[3]https://rubinobservatory.org

[4]https://roman.gsfc.nasa.gov

perturbers are nearby, which allows us to ensure that the recovered pair fractions are inherent to the population of selected pairs rather than a function of environment.

Typically, pair fraction studies via simulations and observations apply physical projected separation cuts that are constant over time and do not vary with the mass of the target system. In this study, we identify how the application of a fixed separation criterion affects inferred pair fractions, and show that a time and mass evolving separation cut is necessary to permit equitable pair fraction comparisons across different mass regimes. Although implementing alternative selection criteria in future observational pair fraction studies may not always be strictly necessary, we recommend that pair selection criteria be reevaluated for observational studies that seek to compare pair fractions as a function of mass or redshift.

Finally, there are a number of galaxy pairs in the Local Group that are mass analogs of the isolated pairs in our sample. For example: the MW–M31 system is a high mass major pair, the MW–LMC and M31–M33 systems are high mass minor pairs, and the LMC–SMC are a low mass minor pair. Studies have examined the frequency of such configurations, particularly at low redshift or in the form of progenitor systems of the Local Group in cosmological simulations (Boylan-Kolchin et al., 2011; Fattahi et al., 2013; Patel et al., 2017b; Geha et al., 2017; Mao et al., 2021), but the prevalence of such pairs in isolation has not yet been quantified as a function of redshift. We utilize our pair dataset to quantify the likelihood of finding isolated mass-analogs of Local Group pairs as a function of redshift, particularly when the present day separations of these systems are folded in.

This paper is structured as follows. In Section 3.2, we outline our methodology for selecting physically associated high mass and low mass pairs from the TNG simulation. In Section 3.3, we provide an overview of the properties of the selected sample, including the number of primaries, pairs, and their stellar mass ratios as a function of time. We present the time-evolving pair fraction of high mass and low mass pairs in Section 3.4, and show how they change for different separation criteria. In Section 3.5, we give context to our results by drawing comparisons to Local Group pairs and other Illustris-based pair fraction studies, and discuss implications for observational campaigns. Finally, we summarize our results and conclusions in Section 3.6.

3.2 Methodology

We aim to quantify and characterize the frequency, or pair fraction, of low mass ($M_* = 10^8 - 5 \times 10^9 \, M_\odot$) and high mass ($M_* = 5 \times 10^9 - 10^{11} \, M_\odot$) galaxy pairs in cosmological simulations as a function of cosmic time. To this end, we utilize the IllustrisTNG suite of simulations to select subhalo pairs as a function of redshift, according to the selection criteria outlined in the remainder of this section.

In Sec. 3.2.1, we provide motivation for and details of the simulation utilized in this study. Sec. 3.2.2 outlines the initial mass cuts used to define our *Subhalo Catalog*, to which we will add stellar mass information. Sec. 3.2.3 outlines the abundance matching prescription used to associate dark matter subhalos with stellar masses, and the creation of the *Subhalo + Stellar Mass Catalog*, from which we will select pairs. Sec. 3.2.4 describes the second set of selection criteria that we use to finally construct the *Full Pair Catalog*.

3.2.1 Simulation Details

The IllustrisTNG project (Springel et al., 2018; Marinacci et al., 2018; Nelson et al., 2018; Naiman et al., 2018; Pillepich et al., 2018a) consists of a suite of dark-matter-only N-body and full physics cosmological simulations that adopt the *Planck2015* ΛCDM cosmology (Planck Collaboration et al., 2016).

In this study, we utilize data from TNG100-1, the main high-resolution, full physics simulation of a $(110.7 \text{ Mpc})^3$ volume (hereafter TNG100)[5] This simulation follows the evolution of baryons and 1820^3 dark matter particles from $z = 127$ to $z = 0$. The volume of this simulation is sufficiently large, and the resolution is sufficiently high, to conduct a simultaneous analysis of the statistics of both low mass and high mass galaxy pairs, as shown by studies of pair statistics in similarly sized volumes (Sales et al., 2013; Patel et al., 2017b,a; Besla et al., 2018).

We utilize the group catalogs produced by the SUBFIND algorithm (Springel et al., 2001a; Dolag et al., 2009). This catalog was created using the Friends-of-Friends (FoF) algorithm (Davis et al., 1985), which links nearby dark matter particles to define large halos

---

[5]We will also use data from TNG100-1-Dark, the main high-resolution dark-matter-only run (hereafter TNG100-Dark), as presented in Sec. 3.4.3.

of associated particles, from which subhalos are identified as overdense and gravitationally bound dark matter structures. In addition, we utilize the merger trees provided by the `SUBLINK` algorithm (Rodriguez-Gomez et al., 2015), which tracks subhalos between snapshots, enabling us to trace the mass evolution of our selected subhalos.

3.2.2   Choosing Low and High Mass Subhalos in TNG100

In this section, we outline the steps to create the *Subhalo Catalog*, which we will utilize to assign stellar masses to each of the dark matter subhalos.

To assess whether the pair fractions of low mass and high mass pairs evolve in fundamentally different ways as a function of redshift, rather than as a product of their environmental conditions, we will focus on galaxy pairs in low-density environments only.[6] As such, we ensure that our target subhalos are sufficiently isolated by placing limits on the virial mass of the FoF group to which our low mass or high mass samples belong.

The following selection process is repeated for each snapshot of the simulation over a redshift range of $z = 0 - 4.2$. We stop our analysis at $z = 4.2$ since the population of massive subhalo pairs falls off rapidly at larger redshifts, where the sample size of high mass primaries falls well below 100 subhalos per snapshot.

At each snapshot, we first apply a cut on the FoF group virial mass, M_{vir}, given by `Group_M_TopHat200` in the TNG100 group catalogs.[7] We define the group mass range for low mass and high mass groups as:

$$\textbf{low mass:}\, M_G = 8 \times 10^{10} - 5 \times 10^{11}\ M_\odot$$

$$\textbf{high mass:}\, M_G = 10^{12} - 6.5 \times 10^{12}\ M_\odot.$$

The FoF group mass criteria is fixed for all redshifts, which means that some low mass groups at high z may be the progenitors of high mass systems at $z = 0$.

By requiring that the FoF group virial mass does not exceed the above limits, we ensure

---

[6]Note that our pair fraction calculations are thus specifically for isolated systems, and the global pair fraction (including both isolated and non-isolated pairs) will be different.

[7]The mass `Group_M_TopHat200` is the mass enclosed by a sphere with mean density $\Delta_c * \rho_c$, where Δ_c is the overdensity constant from Bryan and Norman (1998) and ρ_c is the critical density of the universe at the time calculated. The corresponding virial radius in TNG100 is given by `Group_R_TopHat200`.

that there are no subhalos more massive than these limits that will perturb the dynamical state of identified pairs. For example, selecting low mass pairs from the low mass FoF groups ensures that the selected pairs are not satellite systems of high mass subhalos. Over 99% of subhalos selected from FoF groups in these mass limits are not within 1.5 Mpc of a more massive perturber at $z = 0$.

From the set of FoF groups that pass the group mass cut, we create a catalog of all subhalos within each FoF group that pass a current "minimum mass" threshold. At the given snapshot, we require a minimum subhalo mass, M_h, to be:

minimum subhalo mass: $M_h > 1 \times 10^9 \, \mathrm{M_\odot}$.

M_h is given by the `SubhaloMass` field in the group catalogs, and is the total combined mass of all bound dark *and* baryonic matter. This "minimum mass" threshold ensures that subhalos are resolved into > 100 dark matter particles, and thus should be robustly identifiable using the SUBFIND and SUBLINK algorithms (Rodriguez-Gomez et al., 2015).

For each subhalo that passes both criteria, i.e. the subhalo belongs to either a high mass or low mass FoF group and also passes the "minimum mass" threshold, we use the SUBLINK merger trees to identify the maximum subhalo mass achieved by the subhalo, M_{peak}. We consider only the given snapshot and all previous snapshots in the determination of M_{peak}.

All subhalos in a given snapshot that pass both the FoF group and "minimum mass" selection criteria form our full sample of subhalos, which we call the *Subhalo Catalog*. The catalog contains subhalos at each snapshot from $z = 0$ to 4.2 (snapshot numbers 20-99) and their associated properties, namely: Subhalo ID, FoF Group Number, current subhalo mass M_h, and peak subhalo mass M_{peak}. At z=0, this selection process results in 44,656 subhalos in low mass groups and 38,350 subhalos in high mass groups.

From here, we will use additional selection criteria to identify pairs of subhalos in each group.

3.2.3 Abundance Matching

We utilize a stellar mass to halo mass (SMHM) relationship to assign stellar masses to each of the subhalos in our *Subhalo Catalog.* There are a few reasons we opt to assign stellar masses to our subhalos, rather than use those computed directly from the stellar particles in TNG100.

First, and primarily, utilizing an abundance matching prescription enables the direct comparison of results between dark-matter-only and full hydrodynamics simulations, since the stellar masses are assigned in an identical and prescriptive way. We make a brief note of results for our equivalent analysis using the dark-matter-only, TNG100-Dark simulation, in Sec. 3.4.3.

Second, while the SMHM function of TNG100 at $z = 0$ closely reproduces the profile of the SMHM relation from various abundance matching and semi-empirical models (Pillepich et al., 2018a; Nelson et al., 2019), using stellar masses as calculated from abundance matching allows us to avoid any simulation-dependent stellar mass effects. In particular, we would like to avoid a dependence between our results and the particular subgrid physics model implemented in IllustrisTNG.

Third, abundance matching allows us to account for the observed spread in the SMHM relationship, as we can sample the relation many times to get a distribution of stellar masses for each subhalo in the simulation. Otherwise, we would only be able to perform this analysis once given the set of stellar masses from the simulation. This is particularly important in the low mass regime ($M_h \lesssim 10^{11}\,\mathrm{M_\odot}$) where the scatter in the SMHM function is large, between ~ 0.3 for $M_h \sim 10^{10}\,\mathrm{M_\odot}$ up to ~ 1dex for $M_h \sim 10^8\,\mathrm{M_\odot}$ (Munshi et al., 2021).

We use the abundance matching relationship presented in Moster et al. (2013). The SMHM relationship therein provides an analytic prescription to assign stellar masses to dark matter halos as a function of subhalo mass and redshift, and includes terms to account for the systematic scatter in the SMHM relationship, with a larger scatter at lower halo masses. We were careful to choose the input subhalo mass and redshift that would assign the most accurate stellar masses to each halo given their individual histories.

The abundance matching prescription is calibrated for centrals of FoF groups; thus, we

elect to use the maximum subhalo mass $M_{\rm peak}$ in the stellar mass calculation, rather than the subhalo mass at the given snapshot (see Besla et al., 2018). Using $M_{\rm peak}$ mass allows us to remain robust to scenarios in which a secondary has formed most of its stars, then loses a significant portion of its dark matter content through tidal interactions with a primary, but retains the bulk of its stellar content. In fact, Munshi et al. (2021) found that the stellar mass of subhalos at $z = 0$ in the "Marvel-ous Dwarfs" and "DC Justice League" zoom simulations are more closely correlated with $M_{\rm peak}$ than the $z = 0$ halo mass for halos with peak halo mass $10^8 < M_{\rm peak} < 10^{11}\,{\rm M_\odot}$.

We also use the current redshift of the given snapshot, $z_{\rm snap}$, of each subhalo in the stellar mass calculation. Using $z_{\rm snap}$ means that we account for changes in the stellar mass of both the primary and secondary halo, even after the secondary has entered the primary's halo. This assumption is consistent with findings from Akins et al. (2021), which found that massive dwarf satellites ($M_* \approx 10^8 - 10^9\,{\rm M_\odot}$) entering MW-mass host halos are rarely quenched, and with Geha et al. (2013), which found that dwarfs > 1.5 Mpc from a MW-type galaxy are often star forming and rarely quenched. Additionally, the SAGA survey has found that large satellites of MW-type galaxies are often very blue, with infall into the halo spurring high rates of star formation due to the large gas fraction in dwarfs (Mao et al., 2021). Thus, our abundance matching prescription is of the form $M_* = f(M_{\rm peak}, z_{\rm snap})$.

We calculate the stellar mass for a given subhalo by Gaussian sampling each of the fitting parameters of the analytic framework from Moster et al. (2013), in order to account for the spread in the SMHM relationship. We generate a single stellar mass "realization" using an independent draw from the SMHM distribution to calculate a stellar mass for each subhalo of the full *Subhalo Catalog*. For each snapshot, we repeat this process 1000 times to generate 1000 separate realizations of assigned stellar masses for the *Subhalo Catalog*. The resulting catalog is called the *Subhalo + Stellar Mass Catalog*, and consists of the set of all subhalos from the *Subhalo Catalog*, as well as the 1000 stellar mass realizations. Each realization is treated as an independent sample of galaxy stellar masses, which will allow us to report realistic spreads of pair properties.

3.2.4 Pair Selection

Starting from the *Subhalo + Stellar Mass Catalog*, we outline the pair matching process used to generate the *Full Pair Catalog* below. At each redshift, and for each stellar mass realization, we will identify subhalo pairs consisting of a "primary" and a "secondary," where primaries are the more massive of the pair by stellar mass.

Selecting Primaries

Primary galaxies (equivalently, "primary subhalos") are the most massive galaxy of their FoF group by stellar mass, such that each group will have a singular primary galaxy. Each stellar mass realization is treated independently, and so the subhalo identified as the primary of a group may change between stellar mass realizations.

At a given snapshot, and for each stellar mass realization, we rank-order the subhalos of each FoF group by stellar mass. Primaries are defined as the subhalo with the highest stellar mass (M_{*1}) in their FoF group that passes the following criteria:

$$\textbf{low mass primaries:}\ 10^8 < M_{*1} < 5 \times 10^9\, M_\odot$$
$$\textbf{high mass primaries:}\ 5 \times 10^9 < M_{*1} < 10^{11}\, M_\odot.$$

The stellar mass criteria is fixed, and *does not change* as a function of redshift. At $z = 0$, the stellar mass range for low mass primaries corresponds to isolated analogs of the LMC or M33, while the high mass primaries represent isolated analogs of the MW or M31.

Since our selection is based on stellar mass, and there is a large spread in the SMHM relation, a primary subhalo may not be the most massive subhalo in terms of total subhalo mass.

Selecting Secondary Companions

As before, the selection of secondary companions occurs independently for each stellar mass realization, and for each snapshot. Secondary subhalos are defined as the second most massive subhalo in a FoF group by stellar mass (M_{*2}). Secondary subhalos must also have a

stellar mass ratio with respect to primaries of:

$$\textbf{stellar mass ratio: } M_{*2}/M_{*1} > 1/10.$$

We do not include companions with a stellar mass ratio $M_{*2}/M_{*1} < 1/10$ as we will be limiting our pair sample to traditional definitions of major and minor pairs, which are typically defined to have stellar mass ratios $M_{*2}/M_{*1} > 1/10$ (i.e. Lotz et al., 2011; Rodriguez-Gomez et al., 2015; Snyder et al., 2017; Duncan et al., 2019; Wang et al., 2020; Guzmán-Ortega et al., 2023).

Our subhalo "minimum mass" threshold of $M_{\mathrm{h}} = 10^9$ $M_\odot$ (described in Sec. 3.2.2) corresponds to a mean stellar mass of approximately 10^6 $M_\odot$ at $z = 0$. This stellar mass is well below the 1/10 criteria for the lowest stellar mass primary considered ($M_{*1} > 10^8$ $M_\odot$), ensuring that our pair sample will be complete even at the lowest stellar masses considered.

Creating the Pair Catalog

Pairs consist of a single primary and secondary in a FoF group as defined via the criteria above, such that only one pair is identified in a single FoF group. Each pair is categorized as either a major or minor pair based on the stellar mass ratio between the primary and secondary. Following, e.g. Lotz et al. (2011); Rodriguez-Gomez et al. (2015), the stellar mass ratio criteria for major and minor pairs are:

$$\textbf{major pair: } \frac{1}{4} \leq \frac{\mathrm{M}_{*2}}{\mathrm{M}_{*1}} < 1$$
$$\textbf{minor pair: } \frac{1}{10} \leq \frac{\mathrm{M}_{*2}}{\mathrm{M}_{*1}} < \frac{1}{4}.$$

For each pair, we calculate the physical separation (proper kpc, not comoving kpc) between the two subhalos using the `SubhaloPos` field from the subhalo catalogs. We require that each pair have a minimum separation of 10 kpc between primary and secondary to limit the impact of very close subhalos becoming indistinguishable in SUBFIND as a result of the resolution limit due to the softening length.

If a primary subhalo does not have a companion that meets the stellar mass ratio criteria

and separation criteria, the subhalo will still be considered a primary. We refer to all primaries that do not have a companion with these criteria as "isolated primaries," including primaries with a companion that meets the stellar mass ratio criteria but has a separation < 10 kpc. The total number of primaries includes both isolated primaries and those with selected companions and is larger than the total number of pairs.

For each snapshot and each of the 1000 realizations of the stellar mass in *Subhalo + Stellar Mass Catalog*, we identify a set of isolated primaries and pairs. Additionally, within each realization, no single subhalo can be a part of two separate pairs, such that the primary and secondary of every pair are unique to the pair. The final *Full Pair Catalog* is the collection of all isolated primaries and pairs at each snapshot and includes the following information. For each isolated primary, we store the current subhalo mass ($M_{\rm h}$) and stellar mass from the given realization. For each pair, we store the primary and secondary subhalo masses ($M_{\rm h}$) and stellar masses, the pair separation, and the virial radius of the FoF group (see Sec. 3.2 for virial definitions).

3.3   Sample: Overview of Pair Properties

Utilizing the *Full Pair Catalog*, for each snapshot we compute the total number of primaries (isolated and paired) and pairs (including major and minor) in each of the 1000 realizations. We then compute the median and 1st and 99th percentile spread on the median over all realizations.[8] Additionally, we compute the low and high mass total pair fraction for each individual realization, defined here as the ratio of the total number of pairs ($N_{\rm pairs}$) to the total number of isolated *and* paired primaries ($N_{\rm primaries}$):

$$f_p = \frac{{\rm N_{pairs}}}{{\rm N_{primaries}}}.$$

We again compute the median and spread over all 1000 realizations.

Fig. 3.1 shows the median number (solid and dashed lines) of identified low and high mass primaries and pairs over the redshift range $z = 0 - 4$. The shaded regions show the 1-99%

---

[8]The spread on the median of each realization is very small. Thus, we opt to show the 1st and 99th percentile spread rather than those which align with traditional definitions of 1σ or 2σ measurements
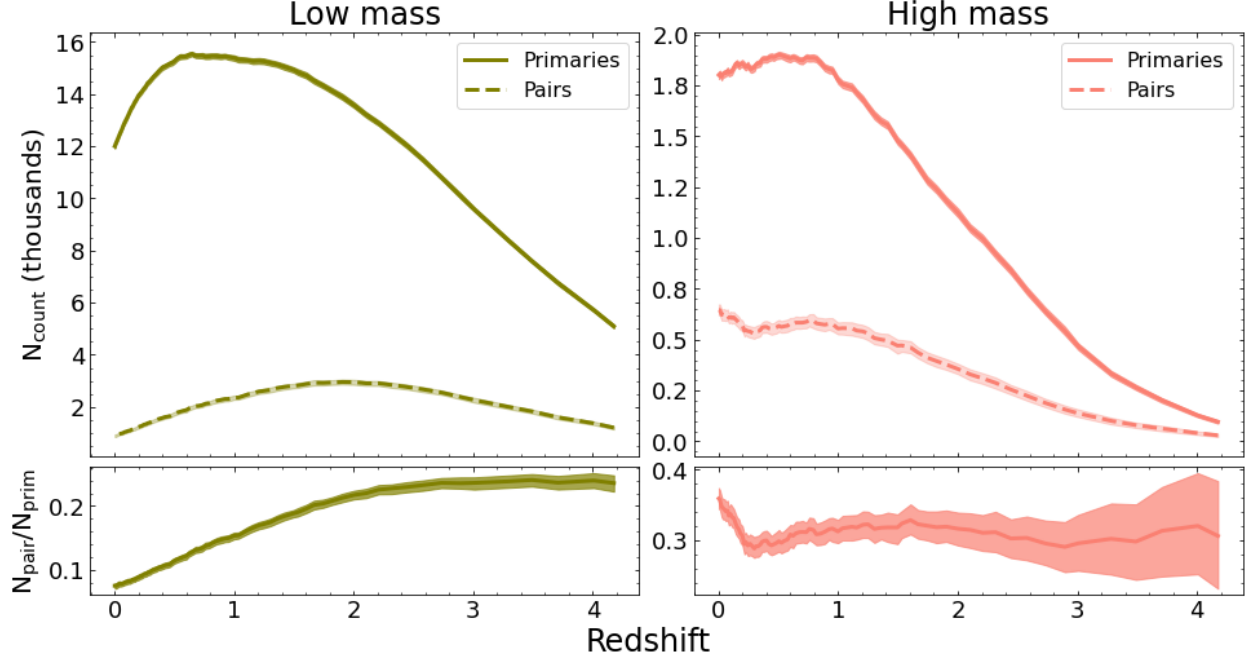
Figure 3.1: (Top) Number of isolated low mass (left) and high mass (right) primaries and pairs as a function of redshift. The solid and dashed lines represent the median of the set of total counts from each of the 1000 stellar mass realizations in the *Full Pair Catalog*, while the shaded regions depict the 1st-99th percentile spread of the median. There are approximately 8 times as many low mass primaries as high mass primaries. The low mass primary count (left) peaks at $z = 1$ (with $\sim 15,000$ primary subhalos per realization), while the low mass pair count peaks at $z = 2$ (with ~ 3000 pairs per realization). The high mass primary count (right) peaks at $z \sim 1$ (with ~ 1900 primary subhalos per realization), while the high mass pair count peaks at $z = 0$ (with ~ 700 pairs per realization). (Bottom) Total pair fraction (fraction of primaries with a major or minor secondary) as a function of redshift (see Sec. 3.3 for calculation details). The low mass total pair fraction is approximately flat between $z = 2.5 - 4$, and decreases from $z = 2.5$ to $z = 0$. The high mass total pair fraction is flat or decreasing from $z = 1$ to $z = 4$, but peaks sharply between $z = 0 - 0.25$.

spread of the set.

The number of identified primaries is lowest at $z = 4$, and rises to a maximum around $z = 1$ for both low and high mass primaries. The median count of low mass primaries (green solid line in top left panel) reaches a maximum of $15,545^{+89}_{-88}$ halos at $z \sim 0.6$, then decreases by $\sim 22\%$ to $12,002^{+85}_{-86}$ halos at $z = 0$. The count of high mass primaries (pink solid line in top right panel) reaches a maximum of 1901^{+16}_{-19} at $z = 0.5$, and slightly declines to $z = 0$. Our sample of high mass primaries represents approximately 20% of all subhalos in TNG100 with the same range of stellar masses at $z = 0$. There are roughly 8 times as many low mass
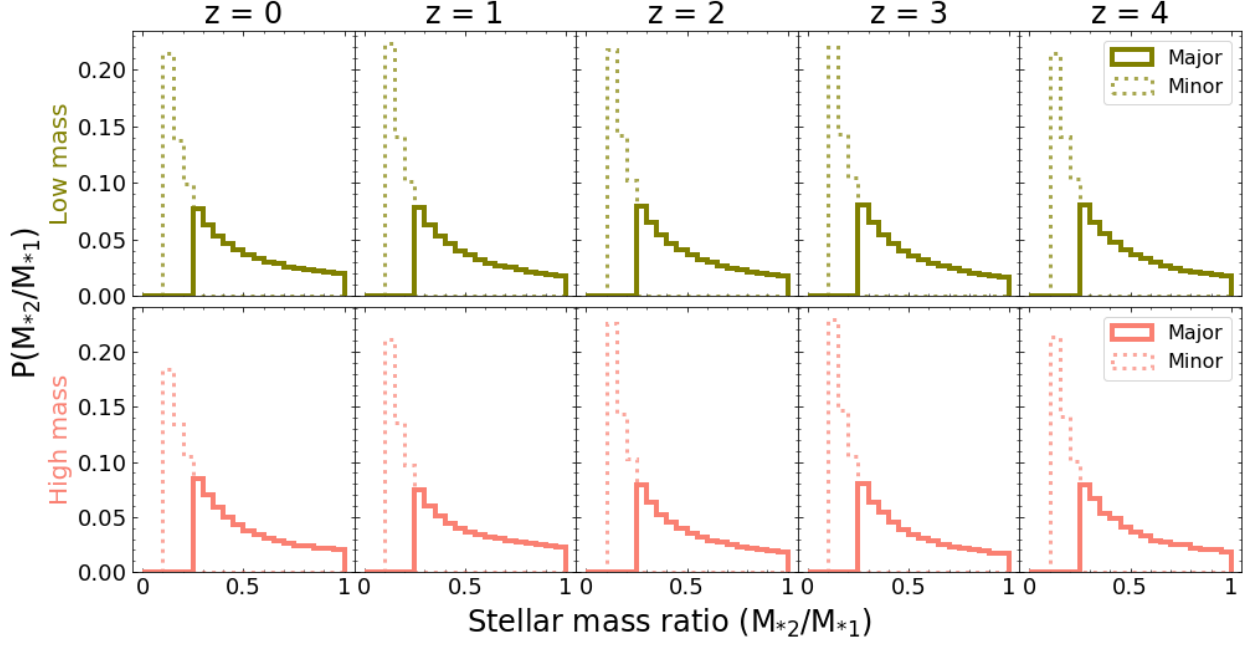
Figure 3.2: Stellar mass ratio distribution of all low mass (top) and high mass (bottom) pairs for all 1000 stellar mass realizations combined at each redshift. Major pairs (solid lines) are defined as pairs with mass ratio $M_{*2}/M_{*1} > 1/4$, while minor pairs (dotted lines) are defined as pairs with stellar mass ratio $1/10 < M_{*2}/M_{*1} < 1/4$. Overall, the stellar mass ratio distribution of major and minor pairs of low and high mass galaxies show little evolution from $z = 4$ (right) to $z = 0$ (left). Major pairs make up $51 - 55\%$ of the total sample of pairs at every redshift for both low and high mass pairs.

primaries as high mass primaries. Note that the comoving volume of TNG100 is the same at all redshifts.

Unlike the primary count, the pair counts for low and high mass pairs peak at very different redshifts. The count of low mass pairs (green dashed line) peaks much earlier, at $z = 1.9$ with 2956^{+99}_{-95} pairs, and decreases to 896^{+51}_{-50} pairs at $z = 0$. The pair count for high mass galaxies (pink dashed line), on the other hand, behaves more similarly to the primary count, increasing from $z = 4$ to $z \sim 1$, then decreasing to $z = 0.25$ before peaking with 647 ± 27 pairs at $z = 0$.

The bottom panel of Fig. 3.1 shows the total pair fraction for low mass and high mass pairs, or equivalently, the fraction of primaries with a major or minor companion. The total pair fractions for both low and high mass pairs are roughly flat for $z = 2.5 - 4$, and display opposite behavior for low redshifts between $z = 0 - 2.5$. The low mass total pair fraction

decreases from $0.233^{+0.008}_{-0.009}$ to 0.075 ± 0.004, a decrease of roughly 68%, while the high mass total pair fraction remains flat between $z = 1 - 2.5$, ranging between 0.275 and 0.351. At very low redshifts, from $z = 0 - 0.25$, the high mass total pair fraction spikes sharply from $0.288^{+0.016}_{-0.013}$ to $0.359^{+0.015}_{-0.014}$, an increase of 37%.

In Fig. 3.2, we show the combined distribution of stellar mass ratios of every pair from all 1000 realizations in the *Full Pair Catalog*. Major pairs make up $51 - 55\%$ of the full sample of pairs at every redshift for both low and high mass pairs. In general, the shape of the distribution remains constant from $z = 0$ (left) to $z = 4$ (right) for both low and high mass pairs, and changes weakly as a function of mass scale and of redshift. There are between ~ 3.3 and 4.8 times more pairs with mass ratios $\sim 1/4$ than $\sim 1/1$, and about $1.8 - 2.2$ times more pairs have 1/10 than 1/4. Roughly 2% of the total pair population is a 1:1 mass ratio encounter; this is true for low and high mass galaxies and across all redshifts considered.

3.4 Results: The Frequency of Low Mass and High Mass Pairs

We have created catalogs of isolated low and high mass galaxy pairs from $z = 0$ to 4.2 in the TNG100 simulation. In this section, we will analyze the frequency of major and minor pair types across cosmic time, with the goal of identifying potential differences between high and low mass galaxies. In Sec. 3.4.1, we examine the redshift evolution of the fraction of primaries with a major or minor companion (the "pair fraction") and compare the results for low mass and high mass pairs. In Sec. 3.4.2, we examine the redshift evolution of the pair fraction as a function of pair separation. In Sec. 3.4.3, we briefly describe how our equivalent pair fraction analysis utilizing the TNG100-Dark simulation compares to the TNG100 results presented in the previous two sections.

In the following analysis, we will treat each stellar mass realization in the *Full Pair Catalog* as an independent sample. At each snapshot, we calculate the median and 1st and 99th percentile spread on the median of the pair fractions in each of the 1000 realizations of the target pair sample. Each of the following figures shows the median as the solid or dashed lines, and the shaded regions correspond to the spread on the median.

3.4.1 Major and Minor Pair Fractions

The major and minor pair fractions are computed in the way as defined in Sec. 3.3 Eq. 3.1, where N_{pairs} is the total number of major *or* minor pairs in the sample. For example, the low mass major pair fraction is the number of low mass major pairs divided by the number of low mass primaries, which can also be interpreted as the likelihood of finding a major companion of an isolated low mass primary.

Fig. 3.3 shows the pair fractions calculated for low and high mass pairs (including both major and minor pairs separately) as a function of time for $z = 0 - 4$. Note that, as discussed in Sec. 3.2.4, we adopt a lower stellar mass ratio floor of $1/10$, and consequently the total pair sample is dominated by major pairs.

The low mass pair fraction evolves distinctly from that of high mass pairs. Low mass pair fractions for both major and minor pairs (green) are approximately constant from $z = 3$ to 4, then decline monotonically to $z = 0$. At $z = 0$, the major pair fraction is $0.041^{+0.003}_{-0.004}$, while the minor pair fraction is 0.034 ± 0.004. At $z = 3$, the pair fractions have increased by 207% to $0.126^{+0.008}_{-0.007}$ for major pairs and 0.111 ± 0.008 for minor pairs.

High mass pair fractions (pink) remain approximately constant for $z > 1$, where the median of the major pair fraction fluctuates between 0.150-0.179, and the median for minor pairs fluctuates between 0.135-0.151. Between $z = 0.3$ and $z = 0$, the major pair fraction increases from $0.163^{+0.011}_{-0.010}$ to $0.207^{+0.012}_{-0.014}$, while the minor pair fraction increases from $0.125^{+0.017}_{-0.014}$ to $0.152^{+0.016}_{-0.017}$.

The bottom panels of Fig. 3.3 show the low mass pair fraction subtracted from the high mass pair fraction (labeled "High $-$ Low"). The difference between high and low mass pair fractions increases with decreasing redshift, peaking at $z = 0$ with a difference of 0.166 ± 0.013 for major pairs and 0.111 ± 0.017 for minor pairs. Thus, at low redshift we expect both major and minor pairs to be more common in high mass galaxies than in low mass galaxies. From $z = 2.5$ to 4, the difference is approximately 0, and thus both major and minor pairs of high and low mass galaxies are equivalently common at high redshift.

Overall, these results show that low mass and high mass pair counts evolve differently over time, particularly at very low redshift, despite the pair fractions being roughly equal at

higher redshift. The implications for the difference in the evolution of pair fractions for low mass and high mass pairs across time are discussed in detail in Sec. 3.5.
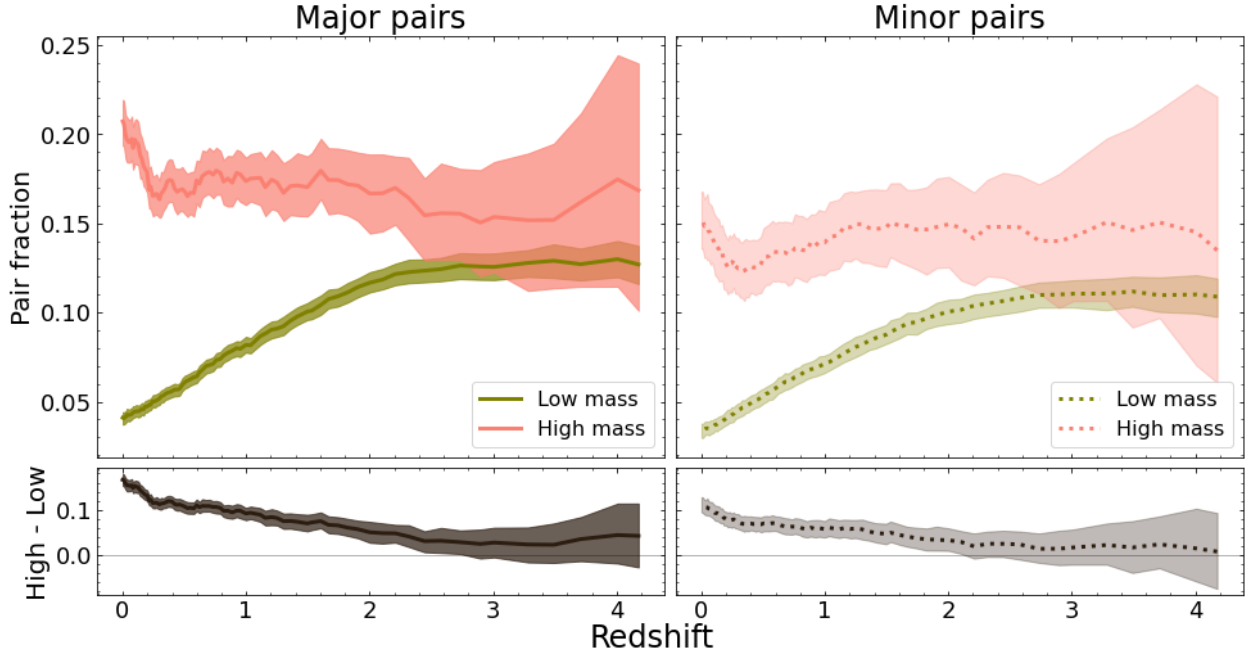
Figure 3.3: (Top) Median pair fraction as a function of redshift, defined as the fraction of low mass or high mass primaries with a major (solid) or minor (dashed) companion (see Sec. 3.2.4). All pairs in the *Full Pair Catalog* must have a minimum separation of at least $> 10\,\mathrm{kpc}$, with no constraint on the maximum separation. Shaded areas show the 1st-99th percentile range on the median (solid and dashed lines) from 1000 stellar mass realizations, as discussed at the beginning of Sec. 3.4. Low mass major and minor pair fractions (green) are both at their minima at $z = 0$, and increase by about 200% by $z \sim 2 - 2.5$, at which point they level off and remain constant from $z = 3$ to 4. On the other hand, high mass major and minor pair fractions reach their maxima at $z = 0$, then abruptly decline until $z \sim 0.25$ before remaining approximately constant from $z = 1 - 4$. (Bottom) The median and 1st-99th percentile range of the subtracted difference between high and low mass pair fractions. The difference peaks at $z = 0$ for both major and minor pairs, and declines with increasing redshift. This panel shows that the redshift evolution of the pair fractions of low and high mass pairs proceeds differently, particularly at low redshift where pairs are more common for high mass galaxies than low mass galaxies.

3.4.2 Major Pair Fractions as a Function of Separation

In this section, we analyze subsets of the low and high mass major pairs from the previous section that pass additional separation criteria. We study two different sets of separation criteria to compare the resulting pair fractions to the full sample shown in Fig. 3.3. In

Sec. 3.4.2 we apply a separation criterion that requires secondaries to be within a given factor of the virial radius of the FoF group, which is a reasonable proxy for the virial radius of the primary. In Sec. 3.4.2, we use a range of limits on the 3D pair separation, where limits are consistent with values adopted in the literature.

In all cases, solid lines correspond to the median pair fraction and shaded regions to the 1st–99th percentile, as explained at the beginning of Sec. 3.4.

Pair Separation Limits as a Function of the Virial Radius of the FoF Group

We calculate the pair fraction for subsamples of low mass and high mass major pairs by selecting only pairs that have separations less than some factor of the virial radius of its FoF group. Note that a minimum separation limit of 10 kpc is always applied to all of our pairs (see Sec. 3.2.4). The virial radius is taken from the `Group_R_TopHat200` field in the group catalogs.

Major pairs typically correspond to the two most massive subhalos in their FoF group. The virial mass of their FoF group is reasonably approximated by the combined subhalo mass of both galaxies in the pair. The combined mass of major low mass galaxy pairs recovers on average 98% of the FoF group mass, and the combined mass of major high mass galaxy pairs recovers an average of 93%. For example, the mass of the Local Group is dominated by that of the MW and M31 (e.g., Chamberlain et al., 2023). The virial radius of the FoF group is thus reasonably approximated by the virial radius of a halo with a virial mass equal to the combined subhalo mass of the two major pair members.

By focusing our separation criteria on the FoF group virial radius, the separation cut will vary both as a function of redshift and as a function of the combined mass of the pair consistently. For the high mass FoF groups, the median virial radius at $z = [0, 1, 2, 3, 4]$ is $\sim (348, 206, 134, 97, 76)$ kpc. For the low mass FoF groups, the median virial radius at $z = [0, 1, 2, 3, 4]$ is $\sim [134, 85, 59, 43, 33]$ kpc.

We choose 6 subsamples, consisting of pairs with separations less than $0.25, 0.5, 1.0, 1.5, 2.0,$ and $2.5 R_{\rm vir}$. The top row of Fig. 3.4 shows the median pair fraction (solid lines) for high mass (pink) and low mass (green) pairs in each of the 6 subsamples. In the bottom row, we show the recovery fraction, which is the fraction of the total pair sample that is recovered by

each subsample, i.e. the number of pairs that pass each separation criterion divided by the total number of pairs in the full sample presented in Sec. 3.4.1.

As the pair separation limits increase (left to right), the recovery fraction increases. So too does the pair fraction, as expected since each consecutive selection cut is less restrictive and will contain more of the full sample. More than 75% of the full pair sample is recovered at all redshifts when the sample contains all pairs within $2R_{\mathrm{vir}}$ (the two rightmost panels of Fig. 3.4).

All subsamples of high mass pairs display broadly the same pair fraction redshift evolution as the full high mass sample (pink line in left panel of Figure 3.3): Each of the subsampled high mass pair fractions peak at $z = 0$ and remain roughly constant or decrease at higher redshift. The finer detail trends from the full sample, particularly the upturn at low z, are reasonably captured if $r_{\mathrm{sep}} < 0.5R_{\mathrm{vir}}$, despite the recovery being $\sim 40\%$.

The subsamples of low mass pairs, however, show a different trend from the full sample (green line in left panel of Figure 3.3) if the separation cut is too small. For $r_{\mathrm{sep}} < 0.25R_{\mathrm{vir}}$, the pair fraction is flat or decreasing as a function of redshift (especially for $z > 1$), similar to the behavior for high mass pairs. For $r_{\mathrm{sep}} < 0.5R_{\mathrm{vir}}$ and $r_{\mathrm{sep}} < 1.0R_{\mathrm{vir}}$, the pair fraction rises to a peak at $z \sim 2$ and then decreases. When the separation is limited to $r_{\mathrm{sep}} < 1.5R_{\mathrm{vir}}$, the trends with redshift for the full low mass sample are recovered, particularly the roughly flat behavior from $z \sim 2 - 4$, despite a sample recovery of $< 75\%$. We also find that differences between the redshift evolution of high mass pairs vs. low mass pairs (particularly at $z < 2$) become apparent if $r_{\mathrm{sep}} < 0.5R_{\mathrm{vir}}$ for both galaxy types. Overall, we find that recovering the redshift evolution of the pair fractions of all galaxy pairs requires a separation cut that contains at least the closest $\sim 40 - 50\%$ of pairs from the full sample at all redshifts.

Pair Separation Limits Based on Static 3D Physical Separation

We calculate the pair fraction for subsamples of major low mass and high mass pairs by including only pairs with separations less than $[50, 70, 100, 150, 200, \mathrm{and}\ 300]$ kpc. Note that these separation criteria do not vary as a function of redshift or mass of the pair, and that a minimum separation limit of 10 kpc is always applied (see Sec. 3.2.4). These separation criteria create subsamples of the *Full Pair Catalog* containing low and high mass pairs with

Figure 3.4: The median and 1st-99th percentile spread are shown by the solid lines and shaded regions, respectively. (Top) The median pair fraction of the subset of high mass (pink) and low mass (green) pairs with 3D separations within a given factor of the pair's FoF group virial radius. Such a separation criteria will vary as a function of both the mass of the pair and the redshift. Recovering the redshift evolution seen for the total sample (left panel of Figure 3.3) requires separation cuts of $r_{\mathrm{sep}} < 1.5R_{\mathrm{vir}}$ for low mass pairs and $r_{\mathrm{sep}} < 0.5R_{\mathrm{vir}}$ for high mass pairs. Recovering the differences between high and low mass pair fraction trends seen for the total sample at $z > 2$, requires $r_{\mathrm{sep}} < 0.5R_{\mathrm{vir}}$ for both galaxy types. (Bottom) The recovery fraction, calculated as the fraction of the total collection of pairs recovered by the subset of pairs at the given separation cut. We find that recovering the redshift evolution of the pair fractions of all galaxy pairs requires a separation cut such that the number of close pairs constitutes more than $\sim 50\%$ of the full sample at all redshifts.

separations between $10 - 50\,\mathrm{kpc}$, $10 - 70\,\mathrm{kpc}$, and so on.

Fig. 3.5 shows the median pair fractions for the subsamples of pairs with separations lower than the physical separation listed at the top of each column. The bottom row of the plot shows the recovery fraction, or the number of pairs in each subsample compared to the full sample of major pairs. Again, as the maximum separation increases (left to right), so too does the pair fraction and recovered fraction of the subsample.

The low mass major pair fraction (green) maintains roughly the same behavior (decreasing with decreasing redshift) for each separation cut, and first recovers the redshift evolution and magnitude of the pair fraction of the full sample (left panel of Fig. 3.3) for a separation cut of $r_{\mathrm{sep}} < 150\,\mathrm{kpc}$. This is not surprising based on our results from the previous section as this separation is larger than the median virial radius of the sample and the recovery fraction is larger than 0.50 at all redshifts (reaching nearly 100% at $z \sim 3$). The low mass pair fraction does not change significantly by excluding pairs with separations $> 150\,\mathrm{kpc}$.

On the other hand, none of the subsamples of the high mass pairs accurately recover the behavior of the full high mass sample. In particular, the redshift evolution of the pair fraction between $z = 0.25$ and 2.5 is not readily distinguishable from that of low mass pairs for any subsample from a physical separation cut. At higher redshifts, the median pair fraction increases rather than leveling off or decreasing as in the full sample. Even for $r_{\mathrm{sep}} < 300\,\mathrm{kpc}$, the high mass pair fraction peaks at $z = 4$, at odds with results using the full pair sample or any of the virial radius cuts in the previous section.

By applying a separation cut that is constant as a function of the redshift and mass of the system, the recovery fraction of the total sample varies markedly as a function of redshift. This is in stark contrast to results from the previous section where the recovery fraction was roughly constant as a function of redshift. Because the same separation cut is applied to low and high mass pairs, the recovery fraction for low mass pairs is universally higher than for high mass pairs at each separation cut, which erases any differences in redshift evolution between the two galaxy types.
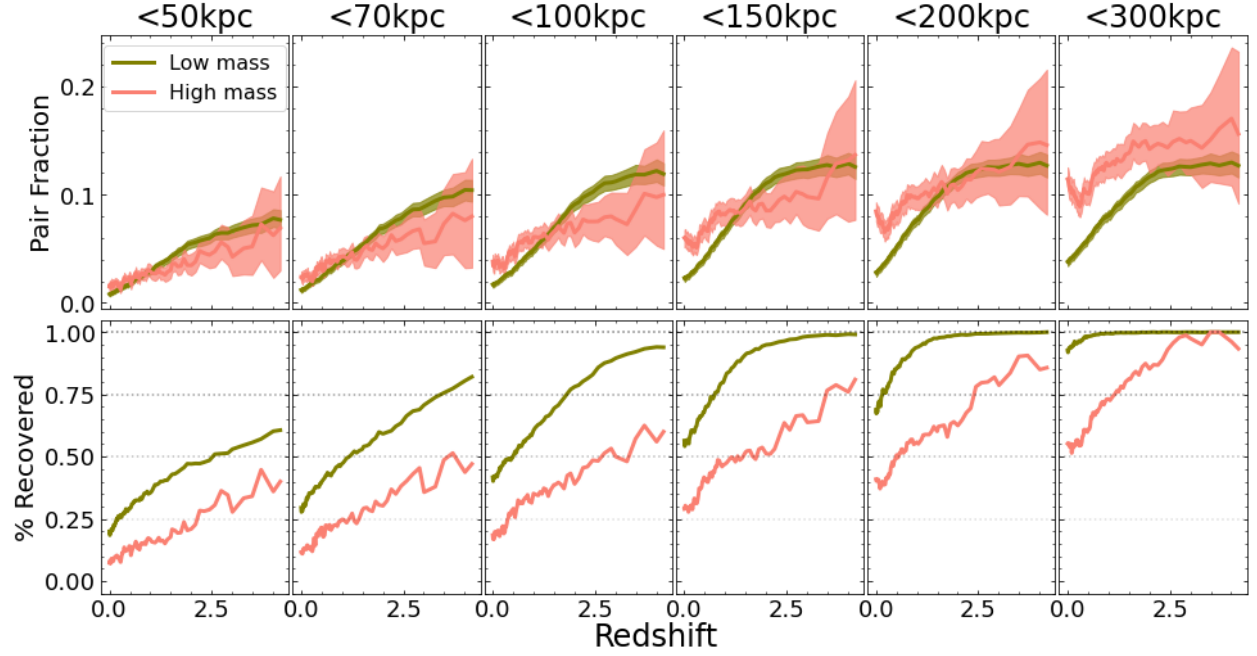
Figure 3.5: (Top) The major pair fraction of the subset of high mass (pink) and low mass (green) pairs with 3D separations less than the value given at the top of each column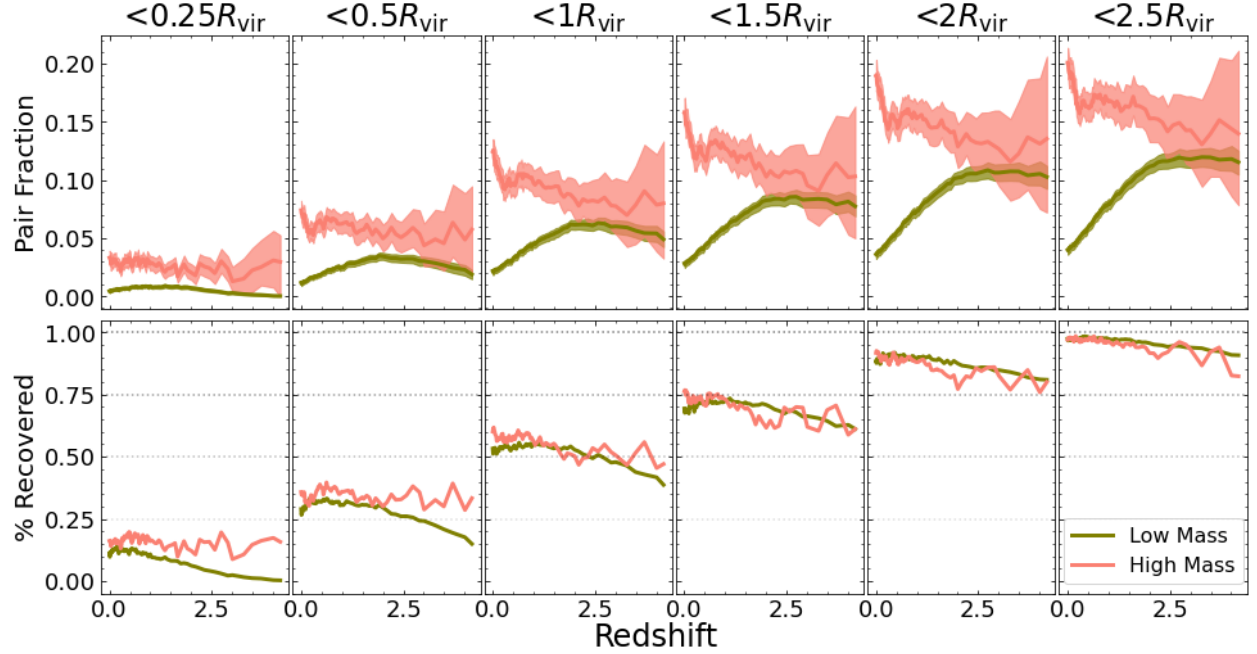. The median and 1st-99th percentile spread are shown by the solid lines and shaded regions, respectively. The 3D separation cut does not vary as a function of redshift or mass of the system. The general redshift evolution of the full high mass pair sample (decreasing with redshift for $z > 1$) is not recovered for any physical separation cut, while the behavior of low mass pair fractions is well recovered by the $r_{\mathrm{sep}} < 150$ kpc subsample. The pair fractions for low mass and high mass pairs are virtually indistinguishable for separation cuts less than 70 kpc. (Bottom) The fraction of the total collection of pairs in the subset that passes each separation cut. The recovered fraction varies as a function of redshift because a constant separation is chosen. A higher fraction of low mass pairs is recovered than high mass pairs at all separation cuts. Less than 50% of all high mass pairs have separations $r_{\mathrm{sep}} < 70$ kpc at all redshifts, and $> 50\%$ of the full high mass sample is recovered at all redshifts only for $r_{\mathrm{sep}} < 300$ kpc. Between 20-60% of low mass pairs have separations $r_{\mathrm{sep}} < 50$ kpc at all redshifts, while a separation cut of $r_{\mathrm{sep}} < 150$ kpc captures roughly 50-100% of the low mass pair population at all redshifts.

3.4.3 Comparison Between TNG100-1 and TNG100-Dark

We repeated the entirety of our analysis using data from the TNG100-Dark simulation. Each step in our selection criteria was repeated identically, including our selection of group halos, abundance matching process, and selection of primary and secondary halos. We created an equivalent catalog to the *Full Pair Catalog* containing only subhalo properties from the TNG100-Dark simulation, and calculated the low and high mass pair fractions for $z = 0 - 4.2$.

We found that the redshift evolution of low mass and high mass pair fractions in the TNG100-Dark simulation mimic those of the TNG100 simulation. In particular, low mass pair fractions remain flat between $z \sim 2$ and 4, and decline from $z = 2$ to a minimum at $z = 0$. High mass pair fractions likewise decrease with higher redshift for $z > 1$, and peak at $z = 0$. The numerical value of the pair fraction at all redshifts is $\sim 10\%$ larger in TNG100-Dark for both low and high mass pairs and for major and minor pairs, which is likely a result of the suppressed abundance of low mass halos due to baryonic physics (Chua et al., 2017).

3.5 Discussion

We performed a pair fraction analysis for low mass and high mass pairs in the TNG100 simulation from $z = 0 - 4.2$, utilizing the full spatial information that simulations enable to ensure that the pairs are physically colocated as part of the same FoF Group. In this section, we discuss the broader impacts and implications of the behavior of high and low mass pair fractions over time.

In Sec. 3.5.1, we draw comparisons between our pair sample and various Local Group pairs to quantify the likelihood of finding isolated analogs of such pairs at higher z. In Sec. 3.5.2, we compare our results to previous studies of pair fractions that utilize simulations. We discuss the observational implications of the pair fraction behavior of low mass pairs and high mass pairs as a function of redshift in Sec. 3.5.3. We conclude by discussing some possibilities for the pair fraction difference between low and high mass pairs in Sec. 3.5.4.

3.5.1 Implications for Local Group Galaxies

Our study encompasses the stellar mass range and stellar mass ratios of a few well-studied pairs within the Local Group and Local Volume. Thus, we can make predictions for the frequency of finding isolated mass analogs of these systems at $z > 0$ for the first time. For example, isolated mass analogs of the following pairs are included in each specified sample: the LMC–SMC and NGC4490-4485[9] (low mass minor pair), the MW–LMC and M31–M33 (high mass minor pair), and the MW–M31 (high mass major pair). Note that both the NGC 4490–4485 and MW–M31 pairs pass all of our pair selection criteria, while the LMC–SMC, MW–LMC, and M31–M33 pairs are non-isolated pairs within a more massive group environment.

Mass analogs of the MW–M31 pair are most common today (pink solid line in the left panel of Fig. 3.3). Given their large separation of $\sim$760 kpc, they would only be included in the $< 2.5R_{\mathrm{vir}}$ panel of Figure 3.4.

We find that isolated mass analogs of the LMC–SMC and NGC 4490–4485 are roughly three times as common at $z > 3$ than at $z = 0$ (green dotted line in the right panel of Fig. 3.3). These high z pairs may enter a more massive group halo to become satellites of a larger galaxy (like the LMC–SMC; Besla et al., 2007; Patel et al., 2017b), or, if they remain isolated, may continue to merge in a manner similar to NGC 4490–4485 (Pearson et al., 2018).

Isolated mass analogs of the MW–LMC and M31–M33 systems are equally likely at $z > 1$ as they are at present (right panel of Figure 3.3). If we fold in the present-day separation of the MW–LMC system ($\sim 50\,\mathrm{kpc}$), this high mass minor pair becomes rare at low z.[10] Specifically, we find that 2% of MW's would host such a close LMC at $z = 0$, which is consistent with other cosmological studies, such as Patel et al. (2017b), which finds that 3.8% of MW-mass halos host an LMC-mass analog within 50 kpc at $z = 0$. We also find that such systems (high mass minor pairs with a low separation) are 2-3 times more common at

---

[9]NGC4490-4485 is a low mass ($M_* = 7.2$ and $0.82 \times 10^9\,\mathrm{M_\odot}$, respectively) galaxy binary that is $\sim 7\,\mathrm{Mpc}$ away from the MW (Theureau et al., 2007; Pearson et al., 2018).

[10]Fig. 3.5 displays pair fraction trends for major pairs. The equivalent plot for minor pairs, which we did not include here, shows the same trends as the major pairs, particularly in the $< 50\,\mathrm{kpc}$ panel where the pair fraction for high mass minor pairs is < 0.02 at $z = 0$.

high z. M31–M33 analogs, which have higher separations ($\sim 200\,\mathrm{kpc}$), are more common than MW–LMC analogs at all redshifts.

3.5.2 Comparison to Existing Pair Fraction Studies

A direct comparison to pair fractions reported from observations is not straightforward, as observationally selected pairs suffer from contamination due to projected pairs and restrictive separation criteria that exclude more widely separated pairs. Instead, we compare our results to pair fractions and merger rates reported by other studies of the Illustris cosmological simulations to establish the reliability of our findings.

Besla et al. (2018) quantified low mass galaxy ($2 \times 10^8 < M_* < 5 \times 10^9$ $\mathrm{M}_\odot$) pair fractions at $z \sim 0$ in the Illustris-1 hydrodynamic cosmological simulation, utilizing both projected and 3D pairs. The selection criteria for projected pairs include a projected separation cut, $r_p < 150$ kpc, and a relative line-of-sight velocity difference $\Delta v_{\mathrm{los}} < 150\,\mathrm{km\ s^{-1}}$.

Searching for pairs in a projected space while having access to the true 3D positions and velocities of the galaxies allowed Besla et al. (2018) to quantify the contamination fraction of false pairs due to projection effects. They found that up to $\sim 40\%$ of identified companions were unrelated but appeared to be close due to projection effects. The projected pair sample also enabled a direct comparison of the cosmologically-derived pair fractions with an equivalently selected low mass galaxy pair fraction from the Sloan Digital Sky Survey (SDSS). They found that the low mass major pair fraction from the SDSS sample was in good agreement with the simulations. The Besla et al. (2018) study points to the Illustris simulation's ability to robustly constrain pair fractions of low mass galaxies, specifically at low z.

We find reasonable agreement with the sample of physical 3D pairs in Besla et al. (2018), which found a major pair fraction between 0.003-0.018 over a mass range of $2 \times 10^8 < M_* < 5 \times 10^9$ $M_\odot$. Our roughly equivalent low mass major pair sample, when adopting a separation cut of $r_{\mathrm{sep}} < 150\,\mathrm{kpc}$, results in a major pair fraction of $0.022^{+0.002}_{-0.003}$ at $z = 0$. We believe our pair fractions are somewhat higher than in Besla et al. (2018) as our stellar mass range for primaries extends to a lower value of $10^8\,\mathrm{M}_\odot$. As such, our results for low mass pairs are robust.

For high mass pairs, Snyder et al. (2017) created mock catalogs using light cones in the Illustris-1 simulation to select pairs in the same fashion as done in observations. They consider major pairs (stellar mass ratio $> 1/4$) with: $1 \times 10^{11} > M_{*1} > 1 \times 10^{10.5}\,\mathrm{M}_\odot$, projected distances between $14 - 71\,\mathrm{kpc}$, and a redshift separation of $\Delta z < 0.02(1 + z_{pri})$, corresponding to a velocity separation of $< 1.8 \times 10^4\,\mathrm{km\,s^{-1}}$ at $z = 2$. They find that the major pair fraction is constant or decreasing for $z > 1$, which is in good agreement with observational studies.

Snyder et al. (2023) extended this work, utilizing the TNG simulation to create mock images of extragalactic survey fields mimicking future planned surveys like JADES. From the mock images, they calculated the pair fraction for major pairs with projected separations between $5 - 70\,\mathrm{kpc}$ and with redshift separations of $\Delta z < 0.02(1 + z)$. Again, they found a flat or decreasing major pair fraction with increasing redshift above $z = 1$.

We cannot directly compare the values of the pair fractions in this work and Snyder et al. (2023), since their work is done in projected space, but we can compare the trends as a function of redshift. We find that the high mass major pair sample has a pair fraction that decreases with redshift above $z = 1$, in agreement with Snyder et al. (2023).

In addition, Rodriguez-Gomez et al. (2015) examine the merger rates of galaxies in the Illustris simulations as a function of stellar mass and redshift. From their Figures 7 and 10, there is roughly a factor of 4 difference in the major merger rate for high mass ($M_* \sim 10^{11}\,\mathrm{M}_\odot$) vs. low mass ($M_* \sim 10^8\,\mathrm{M}_\odot$) galaxies at $z = 0$, and the difference becomes smaller at higher redshift. A strong mass dependence of the galaxy merger rate at $z = 0$ is also seen in Figure 12 of Guzmán-Ortega et al. (2023), as well as in results from semi-empirical models (Stewart et al., 2009; Hopkins et al., 2010b). From our Figure 3.3, there is also a factor of 4 difference in the pair fraction for high and low mass galaxies at $z = 0$, which becomes smaller at higher redshift. The consistency between our results and the variation with stellar mass and redshift of the galaxy merger rate suggests that our finding of different pair fractions between low and high mass galaxies at $z = 0$, as well as their different redshift evolution trends, is indeed reliable.

3.5.3 Implications for Observational Pair Fraction Studies

In Sec. 3.4.1, we presented the pair fraction of high mass and low mass galaxy pairs and found that the relative frequency of the two populations evolves distinctly from $z = 0 - 4.2$. High mass pair fractions peak at $z = 0$, decrease from $z = 0$ to 0.3, after which they remain roughly constant or mildly decrease with increasing redshift. In contrast, low mass pair fractions increase with increasing redshift until $z = 2.5$, after which the frequency remains roughly constant with increasing redshift. This behavior is seen for both major and minor pairs.

In Sec. 3.4.2, we characterized the behavior of pair fractions for subsamples of the full pair catalog that pass additional separation cuts. We found that physical separation cuts which do not vary as a function of time and mass eliminate the ability to distinguish the different redshift evolution of high and low mass pair fractions. Instead, by adopting a separation cut based on the virial radius of the group halo, we can accurately recover the different redshift evolution of low mass vs. high mass pair fractions, particularly at $z < 2.5$.

These results indicate that future observational studies that seek to compare low mass and high mass pair fractions, particularly as a function of time, must take care when determining their pair selection criteria. We advocate for separation criteria that varies as both a function of mass and redshift, such as our choice of $r_{\text{sep}} < 1.0 R_{\text{vir}}$, where R_{vir} can be inferred using an estimate of the combined dark matter mass of the pair. [11] We have shown that utilizing fixed physical separation cuts can lead to significant deviation in the behavior of galaxy pair fractions for different galaxy masses and between $z = 0$ and 4, and thus it is imperative to carefully consider the selection criteria used in future observational pair fraction studies of low and high mass pairs over time.

---

[11]Taking the observed stellar mass of each pair member, the halo mass for each pair can be estimated using the SMHM relation (e.g. Moster et al., 2013). The combined halo mass of the pair can then be used as a proxy for the virial mass of the FoF group (M_{vir}) to compute the virial radius, e.g.

$$R_{\text{vir}} = \sqrt[3]{\frac{3M_{\text{vir}}}{4\pi\Delta_c\rho_c}}, \tag{3.1}$$

where ρ_c is the critical density of the Universe, and Δ_c is the overdensity constant (see Binney and Tremaine, 2008). Both ρ_c and Δ_c are functions of redshift, such that R_{vir} changes as a function of both the mass of the pair and redshift.

In addition, our findings are specific to systems in isolated environments, and thus may not be representative of the pair fractions of a more "standard" observational field that contains pairs in isolated and high density environments. Mitigating this issue in observations would require making certain isolation cuts, such as those employed in Geha et al. (2013) to identify low mass pairs in isolated (> 1.5 Mpc away from an L^* galaxy) and non-isolated (within 1.5 Mpc of an L^* galaxy) environments.

Given that chance projections will artificially boost the pair fraction as the pair separation is increased, recovering the general evolution of the pair fraction as a function of redshift may be more realistic than recovering the magnitude of the pair fraction itself, since the former requires smaller separation limits. The requirement of $r_{\mathrm{sep}} < 1.0\,R_{\mathrm{vir}}$ for low mass pairs translates to median separation limits that are less than $\sim 60(30)\,\mathrm{kpc}$ at $z \sim 2(4)$, which are sufficiently small as to avoid major projection effects. For high mass pairs, this translates to separations less than $\sim 135(75)$ at $z \sim 2(4)$.

Pair fractions are typically translated to galaxy merger rates using an observability window (Lotz et al., 2011). The good agreement between the difference in the low mass and high mass pair fractions and the mass-dependent galaxy merger rates from Rodriguez-Gomez et al. (2015) suggests that applying separation cuts which can recover this mass dependency are critical to reliably translating pair fractions to galaxy merger rates. In fact, JWST is expected to identify low mass galaxies ($M_* > 10^8\,\mathrm{M_\odot}$) out to at least $z = 10$ (Cowley et al., 2018; Williams et al., 2018; Behroozi et al., 2020). We argue that the adopted pair separation criteria, particularly for low mass pairs, will greatly affect the measured pair fractions and consequently the inferred merger rates.

3.5.4 Underlying Physical Behavior of Galaxy Pairs

Though we find a distinct difference in the redshift evolution of low mass and high mass pair fractions, our study does not explicitly identify the specific driver of these differences. In a ΛCDM universe, the buildup of structure proceeds hierarchically, with smaller structures merging to form larger and larger structures at later times. This may explain the significant decrease in the pair fraction of isolated low mass galaxies from $z = 2$ to $z = 0$, since more and more low mass systems would be accreted into larger group structures and would thus

be removed from our isolated pair sample.

On the other hand, the inherent dynamics of the pairs themselves may dictate the redshift evolution of their respective pair fractions. For example, if low mass pairs tend to have very short merger timescales, the total number of low mass pairs would decrease much more rapidly than massive pairs with a very long timescale.

Understanding in further detail the origin of the discrepancy in the redshift evolution of low mass vs. high mass pairs requires tracking the specific pairs across simulation snapshots to trace their orbits and study changes in the mass and environment of the pairs across cosmic time. We leave this as the focus of future work.

3.6 Summary and Conclusions

In this paper, we construct a sample of low mass ($10^8 < M_* < 5 \times 10^9$ M$_\odot$) and high mass ($5 \times 10^9 < M_* < 10^{11}$ M$_\odot$) pairs from the TNG100 simulation from $z = 0$ to 4.2. Pairs are selected as belonging to the same FoF group such that they are isolated and physically associated, and not contaminated by projection effects. Major and minor pairs are determined using the stellar mass ratio (1–1/4 and 1/4–1/10, respectively) between the primary and secondary halo, where stellar masses are assigned using an abundance matching prescription from Moster et al. (2013) to generate 1000 separate realizations of selected pairs at each redshift in order to sample the error space of the SMHM relation.

From this pair sample, we calculate the pair fraction as a function of redshift for 4 different pair types: low mass major pairs, low mass minor pairs, high mass major pairs, and high mass minor pairs. Our goal is to quantify the evolution of low mass and high mass galaxy pairs across cosmic time and to identify any differences in the redshift evolution of pair fractions of low mass and high mass pairs. We also aim to determine how separation criteria for pair selection can affect the pair fraction evolution of high and low mass pairs. To this end, we additionally employ both static and time- and mass-evolving separation cuts to explore the resulting impact on the pair fractions.

Our main findings are as follows:

- The pair fraction for low mass and high mass pairs does not proceed identically

throughout cosmic time. In fact, the two mass scales have opposite behaviors at $z < 2.5$ (see Figure 3.3). The pair fraction of low mass pairs increases from $z = 0$ to $z \sim 2.5$, while the pair fraction of high mass pairs peaks at $z = 0$ and is constant or slightly decreasing at $z > 1$.

- At z=0, we find a low mass major (minor) pair fraction of $0.041^{+0.003}_{-0.004}$ (0.034 ± 0.004), and a high mass major (minor) pair fraction of $0.207^{+0.012}_{-0.014}$ ($0.152^{+0.016}_{-0.017}$). These results are consistent with other simulation-based studies that find that the merger rate for high mass pairs is $\sim 4\times$ higher than for low mass galaxies (e.g., Rodriguez-Gomez et al., 2015).

- Low mass minor pairs evolve similarly to low mass major pairs as a function of redshift.

- The differences in redshift evolution of pair fractions for high and low mass pairs is well recovered using a subsample of pairs with a maximum separation cut that varies with mass and redshift, specifically for $r_{\mathrm{sep}} < 1R_{\mathrm{vir}}$, where R_{vir} is the virial radius of the FoF group. This separation cut corresponds to separations less than [134(348), 59(134), 33(76)] kpc at z=[0,2,4] for low mass (high mass) pairs. In particular, a maximum separation cut of $r_{\mathrm{sep}} < 1R_{\mathrm{vir}}$ encompasses between $\sim 40 - 60\%$ of the full population of pairs at all redshifts, and recovers the distinct differences in the redshift evolution of low mass vs. high mass pair fractions from $z = 0$ to 2.5.

- The identified differences in the redshift evolution of high and low mass pairs are erased when a static physical separation cut is employed, i.e. a separation that does not evolve with redshift or with mass (e.g. $r_{\mathrm{sep}} < 50\,\mathrm{kpc}$). This occurs because fixed-separation cuts capture roughly 10-50% more pairs in the low mass pair sample than the high mass sample at all redshifts. Consequently, selecting the same volume to study the pair fractions for low and high mass galaxies via a static separation cut will bias inferred pair fractions.

- Isolated mass-analogs of the MW–M31 are most common at $z = 0$, while analogs of the MW–LMC and M31–M33 are equally common at $z = 0$ as at $z > 1$. However, MW–LMC-type systems with very low separations ($\lesssim 50\,\mathrm{kpc}$) are 2-3 times more common

at higher redshift ($z \sim 2$). Isolated analogs of the LMC–SMC and NGC 4490–4485 are 3 times more common for $z > 3$.

A number of studies have identified a mass and redshift dependence in the galaxy merger rate as a function of time, particularly in cosmological simulations and semi-empirical models (see, e.g. Stewart et al., 2009; Hopkins et al., 2010b; Rodriguez-Gomez et al., 2015). Our results show that galaxy pair fractions for physically associated, isolated pairs likewise evolve as a function of mass and redshift. However, we also find that the recovered pair fractions are sensitive to the separation criteria that is used to define pairs. The redshift evolution of pair fractions for physically associated low mass and high mass galaxy pairs can only be distinguished when the separation criteria are a function of both mass and redshift.

Observational campaigns that seek to recover low mass and high mass pair fractions should consider using mass- and redshift-evolving separation criteria to select pairs. Many observational pair fraction studies use static definitions of the maximum projected separation to determine close pairs, then translate between pair fractions and merger rates via an observability timescale. The observability timescale, however, is not typically calibrated as a function of both mass and redshift, meaning that identical measured pair fractions of high and low mass pairs will yield indistinguishable merger rates.

In order to observationally recover the cosmologically expected difference between the merger rates of high and low mass galaxies, it is crucial to ensure that differences in the redshift evolution of the pair fraction for these galaxy populations can be adequately captured. This will be of particular importance in the era of JWST, where more low mass ($M_* \sim 10^8 \, \mathrm{M_\odot}$) galaxies and galaxy pairs will be discovered at higher redshift (up to $z > 10$), and for future wide-field galaxy surveys enabled by the Roman Space Telescope and Rubin Observatory.

Chapter 4

A Physically Motivated Framework to Compare Merger Timescales of Isolated Low- and High-Mass Galaxy Pairs Across Cosmic Time

Abstract

The merger timescales of isolated low-mass pairs ($10^8 < M_* < 5 \times 10^9$ $M_\odot$) on cosmologically motivated orbits have not yet been studied in detail, though isolated high-mass pairs ($5 \times 10^9 < M_* < 10^{11}$ $M_\odot$) have been studied extensively. It is common to apply the same separation criteria and expected merger timescales of high-mass pairs to low-mass systems, however it is unclear if their merger timescales are similar, or if they evolve similarly with redshift. We use the Illustris TNG100 simulation to quantify the merger timescales of isolated low-mass and high-mass major pairs as a function of cosmic time, and explore how different selection criteria impact the mass and redshift dependence of merger timescales. We find that the merger timescales for low- and high-mass pairs are the same from $z = 0 - 6$ in the absence of any separation criteria. We then present a physically-motivated framework for selecting pairs via a scaled separation criteria, wherein pair separations are scaled by the virial radius of the primary's FoF group halo ($r_{\mathrm{sep}} < 1 R_{\mathrm{vir}}$). Applying these scaled separation criteria recovers equivalent merger timescales for both mass scales at all redshifts. Alternatively, static physical separation selections applied equivalently to all galaxy pairs at all redshifts leads to a difference in merger rates of up to $\sim 1 \mathrm{Gyr}$ between low- and high-mass pairs, particularly for $r_{\mathrm{sep}} < 150\,\mathrm{kpc}$. As a result, applying the same merger timescales to physical separation-selected pairs will lead to a bias that systematically over-predicts low-mass galaxy merger rates.

4.1 Introduction

Galaxy merger rates provide an important pathway for tests of hierarchical assembly from ΛCDM theory, and are critical for understanding the formation and evolution of galaxies across time (e.g. Stewart et al., 2009; Hopkins et al., 2010b; Rodriguez-Gomez et al., 2015). In the era of future surveys with JWST, Rubin, and Roman, these tests will be extended to higher redshifts and lower mass scales than were previously accessible (Gardner et al., 2006; Spergel et al., 2015; Robertson et al., 2019a,b; Behroozi et al., 2020; Martin et al., 2022).

At higher redshift ($z \gtrsim 1$) and at lower masses ($M_* \lesssim 10^{9.5}$), even isolated galaxies are highly disturbed (Wuyts et al., 2012, 2013; Martin et al., 2018; Rodriguez-Gomez et al., 2019; Martin et al., 2021), making close pair fractions a critical alternative to morphological signatures for merger rate studies. However, there is currently no framework for comparing merger rates for low-mass and high-mass galaxies as a function of time, and tensions between predictions from theory and observational studies exist in the literature at low masses (see e.g. Fig. 10 in Rodriguez-Gomez et al., 2015).

This study seeks to establish a framework to enable comparisons of merger rates across mass scales and redshift so that merger rates of low-mass galaxies can be used as tests of ΛCDM theory. These results can also be used to interpret observations of galaxy morphologies and their hierarchical evolution, including the role of mergers in triggering starbursts, fueling active galactic nuclei (AGN), facilitating the formation of tidal features, etc., in low-mass galaxies (e.g. Stierwalt et al., 2015; Pearson et al., 2016; Privon et al., 2017; Kristensen et al., 2021; Martin et al., 2021; Luber et al., 2022; Martin et al., 2022; Guzmán-Ortega et al., 2023; Byrne-Mamahit et al., 2024; Kado-Fong et al., 2024).

In our previous work, we show that the redshift evolution of pair fractions of isolated low-mass and high-mass pairs in Illustris TNG100 differ significantly, particularly at $z < 3$ where pair fractions of low-mass pairs decrease up to 75% between $z = 3$ and $z = 0$, while high-mass pair fractions peak at $z = 0$ (Chamberlain et al., 2024). We suggested that differences in the merger timescales of low-mass and high-mass pairs might be the cause of the pair fraction evolution differences. In our following analysis, we will investigate this question directly and answer whether merger timescales are responsible for these pair fraction

differences.

Additionally, we found in Chamberlain et al. (2024) that recovering the pair fraction differences seen between the two mass scales is sensitive to the selection criteria adopted during pair selection. Physical separation cuts applied equivalently to low-mass and high-mass pairs at all redshifts eliminate the ability to distinguish the behavior of the true pair fraction evolution (see their Figure 5), even for separation cuts as large as $r_{\mathrm{sep}} < 300\,\mathrm{kpc}$. Alternatively, when separation criteria vary with the mass and redshift of each system, in particular when the separation is scaled by the virial radius R_{vir} of the pair's FoF group halo, the ability to distinguish the underlying pair fraction behavior was recovered for scaled separations as low as $r_{\mathrm{sep}} < 0.5\,R_{\mathrm{vir}}$ (see their Figure 4). Employing scaled separation criteria then permits the equivalent comparison of pair fractions between low-mass and high-mass pairs, and robust comparisons across redshifts from $z = 0 - 4$. Since merger rate estimates are derived from close pair fractions and merger timescales, the results from our previous work imply that careful consideration of separation criteria is required for merger timescale and merger rate studies at different mass scales and redshifts as well.

In order to investigate the impact of pair selection criteria on merger timescales specifically, we will track the pairs selected in Ch. 3 forwards and backwards in time to construct orbits for each pair. We will then study the merger timescales of isolated low-mass and high-mass pairs for the same set of physical and scaled separation criteria used in Ch. 3 to determine whether merger timescales of isolated pairs are robust to the selection criteria used to determine the pair samples.

In this paper, we aim to extend the framework for pair selection criteria presented in Ch. 3. In Sec. 4.2, we detail our selection criteria for isolated low-mass and high-mass orbits in the Illustris TNG100 simulation. We examine the redshift evolution of the number of pairs and merger fraction of our sample in Sec. 4.3. In Sec. 4.4, we present our findings on the separation and redshift dependence of the merger timescales of low-mass and high-mass pairs, and study the impact of physical and scaled separation criteria for pair selection. Finally, we discuss the implications of this work and provide suggestions for a self-consistent way of studying pairs across redshifts and mass scales in Sec. 4.5, and present our final conclusions in Sec. 4.6.

4.2 Methodology

The IllustrisTNG simulation suite (Springel et al., 2018; Marinacci et al., 2018; Nelson et al., 2018; Naiman et al., 2018; Pillepich et al., 2018a) is a set of large volume dark-matter-only and full magnetohydrodynamical cosmological simulations consistent with the *Planck 2015* ΛCDM cosmology (Planck Collaboration et al., 2016).

Following Ch. 3, we use TNG100-1 (hereafter TNG100), which is the highest resolution full physics run of the $(100\,\mathrm{Mpc})^3$ volume. In particular, we utilize the group catalogs produced by the SUBFIND algorithm (Springel et al., 2001b; Dolag et al., 2009) and the merger tree catalogs generated by the SUBLINK algorithm (Rodriguez-Gomez et al., 2015). The catalogs consist of a set of 100 snapshots, ranging from $z \sim 20$ (snapshot 0) to $z = 0$ (snapshot 99).

Our sample consists of major low-mass and high-mass pairs (stellar mass ratio $1/4 \leq M_{*2}/M_{*1} \leq 1$) that are isolated, but physically associated, as in Chamberlain et al. (2024). From this sample, we will determine the fraction of pairs at each snapshot that merge before $z = 0$, and track the orbits of each pair to study their merger timescales from $z = 0 - 6$.

4.2.1 Pair Sample

We begin with an extension of the *Full Pair Catalog* described in Ch. 3, which consists of a collection of isolated galaxy pairs at each snapshot in TNG100. We collect our base sample at each redshift in the simulation. A brief version of the selection routine is transcribed here for completeness, and we refer readers to Sec. 2 of Ch. 3 for more detail and a discussion of the selection criteria choices.

At each snapshot, low-mass and high-mass pairs are chosen by first selecting the two most massive subhalos (by assigned stellar mass, using abundance matching; see below) from FoF

groups with virial mass M_G [1]

$$\textbf{low mass:} \, M_G = 8 \times 10^{10} - 5 \times 10^{11} \, M_\odot$$

$$\textbf{high mass:} \, M_G = 1 \times 10^{12} - 6.5 \times 10^{12} \, M_\odot.$$

Requiring pairs to belong to the same FoF group ensures that the pairs are distant from other massive nearby systems that could perturb the dynamical state of the pair. In addition, for each pair, we calculated the Hill Radius of every FoF group with a higher mass within $10 Mpc$ of the pair, as a proxy to discern whether the pair lies outside the gravitational sphere of influence of these more massive groups. We found that over 99% of our pairs at $z = 0$ are more distant than two times the Hill Radius of each FoF group.

We require the subhalos that constitute a pair to meet a minimum subhalo mass, M_h, criteria of

$$\textbf{minimum subhalo mass:} \, M_h > 1 \times 10^9 \, M_\odot.$$

at the snapshot of consideration. For TNG100, this ensures that subhalos are resolved into over $\sim$100 particles, enough to robustly identify gravitationally bound subhalos in the SUBFIND and SUBLINK catalogs. For each subhalo in the FoF group that passes the minimum subhalo mass criteria, we utilize the SUBLINK catalogs to find the peak halo mass of each subhalo (Rodriguez-Gomez et al., 2015).

As in Ch. 3, stellar masses are assigned to each subhalo in the FoF group using the abundance matching prescription of Moster et al. (2013). Utilizing abundance matching to assign stellar masses allows us to circumvent simulation-specific stellar mass effects, and also results in a more straightforward process for applying our methodology to observational studies (see Sec. 4.5.3 for more details). The peak halo mass and current redshift are used to calculate the stellar mass of each subhalo via the abundance matching prescription $M_* = f(M_{\text{peak}}, z)$, where z is the redshift of consideration.

In Ch. 3, the abundance matching prescription was sampled 1000 times for each subhalo to

---

[1]We use `Group_M_TopHat200` from the TNG100 Group Catalogs as the FoF Group virial mass. This mass is defined to be the mass enclosed by a sphere with mean density $\Delta_c * \rho_c$, where Δ_c is the overdensity constant from Bryan and Norman (1998) and ρ_c is the critical density of the universe at the time calculated. The corresponding virial radius in TNG100 is given by `Group_R_TopHat200`.

account for the spread in the Stellar Mass – Halo Mass (SMHM) relation. For the present study, we only use the stellar masses given by the median of the abundance matching relationship. We expect that the spread of merger timescales from different orbital configurations, as well as the redshift spacing of the TNG100 snapshots, will dominate over uncertainties from the number of pairs in the catalog, which varied by $\sim 3\%$ (as shown in Fig. 1 in Ch. 3).

Primary subhalos are defined as the subhalo with the highest assigned stellar mass, M_{*1} in the FoF group, and secondaries are defined as the second most massive subhalo with stellar mass M_{*2}. Our sample of major pairs then consists of all pairs of primary and secondary subhalos with

$$\textbf{low mass primaries: } 10^8 < M_{*1} < 5 \times 10^9 \, \mathrm{M_\odot}$$
$$\textbf{high mass primaries: } 5 \times 10^9 < M_{*1} < 10^{11} \, \mathrm{M_\odot}$$
$$\textbf{stellar mass ratio: } M_{*2}/M_{*1} > 1/4.$$

A primary or secondary subhalo can only be a member of one single pair at a given snapshot, such that a collection of N pairs consists of N unique primaries and N unique secondaries. A subhalo can belong to multiple different pairs at different redshifts. For example, the primary of a pair that merges at $z = 2$ can be selected with a different secondary at $z = 1$, constituting a new pair. More detail regarding the uniqueness of pairs and orbits is discussed in Sec. 4.2.3.

The base sample of pairs used for this analysis then consists of the set of all isolated low-mass and high-mass major pairs from each redshift of the TNG100 simulation.

4.2.2 Mergers

Here we describe how mergers are identified. Note that this definition is specific to subhalo mergers and therefore results are not guaranteed to hold for galaxy mergers (see e.g., Rodriguez-Gomez et al., 2015; Patton et al., 2024), especially in cases where dark matter subhalos and galaxies have different centers of mass, as is the case in our own Galaxy (Gómez et al., 2015; Garavito-Camargo et al., 2019; Petersen and Peñarrubia, 2021; Chamberlain et al., 2023).

The primary and secondary subhalos of each pair have a `SubfindID` in the SUBFIND merger tree catalogs, which contain information about every FoF group and subhalo at each redshift. The SUBLINK catalogs track subhalos from one redshift to the next, and thus enable us to track subhalos both backwards and forwards in time from any given redshift.

We utilize the `DescendantID` field of the SUBLINK catalogs to determine which pairs from our base sample merge before the end of the simulation (at $z = 0$) and when each merger occurs. The `DescendantID` field provides the `SubhaloID`[2] of the subhalo's descendent in the next (or one of the following) snapshots, if it has one.

In this analysis, a pair is classified as a merger if the primary and secondary subhalo share the same `DescendantID` at the same redshift. This means that the primary and secondary subhalo have merged such that SUBFIND can no longer distinguish them as two separate halos, therefore yielding a single descendant subhalo. If a primary and secondary never share the same `DescendantID` at the same redshift, the pair is defined as a 'non-merger.'

For each merging pair, we define the *merger redshift* as the redshift that immediately follows the first snapshot where the primary and secondary have the same `DescendantID`. For example, if the primary and secondary have different `DescendantIDs` from $z = 6$ to $z = 2$, but have the same `DescendantID` at $z = 2$, then the merger must take place between $z = 2$ and $z = 1.9$, which is the next redshift corresponding to a snapshot in the simulation. In this example, we take $z = 1.9$ to be the merger redshift.

4.2.3   Orbits

We extract orbits for all mergers and non-mergers in our base pair sample using the merger tree catalogs. An orbit for a single pair is defined to be the physical separation between the primary and secondary subhalo as a function of redshift (or lookback time).

A given pair from the base sample at redshift z_n passes all of the selection criteria from Ch. 3 at z_n, and can additionally be followed backwards and forwards in time using the SUBLINK merger trees. We track the positions of both the primary and secondary subhalo at each redshift and calculate the physical separations after accounting for the periodic boundary

---

[2]Note that the `SubhaloID` is distinct from the `SubfindID`, and is unique for every subhalo in the merger trees. The SUBLINK catalogs provide the associated `SubfindID` of each subhalo.
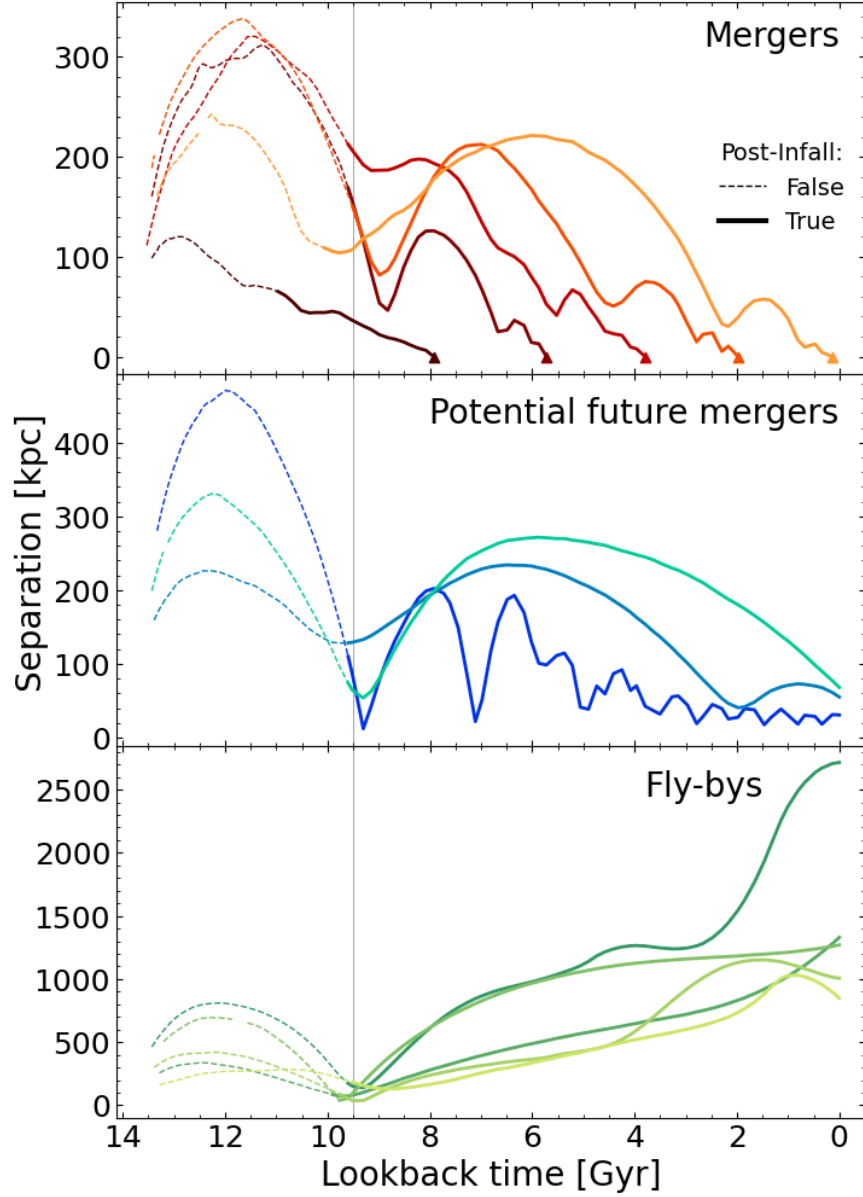
Figure 4.1: Selection of example orbits of low-mass major pairs that pass the pair selection criteria at $z = 1.5$, showing the separation between the primary and secondary as a function of lookback time. (Top) Orbits of pairs that merge before $z = 0$. (Middle) Orbits of pairs that do not merge before $z = 0$ (non-mergers), but are likely to merge if the simulation continued. (Bottom) Orbits of pairs that do not merge before $z = 0$ (non-mergers) and are unlikely to do so in the future $\sim 2\,\mathrm{Gyr}$ (past the end of the simulation). Solid lines represent the post-infall orbits, i.e. after the pair share a common FoF group. Dashed lines show the pre-infall portion of the orbit. Triangle points in the first panel show the first redshift after merger where the orbit has a separation of 0 kpc. The vertical grey line marks $z = 1.5$ at a lookback time of $9.5\,\mathrm{Gyr}$.

conditions of the simulation box. In cases where the primary or secondary does not have a defined position at a given redshift, we do not compute a value for the separation at that redshift.[3]

In addition to the physical separation, we also calculate the scaled separation of a pair at each redshift. We use the definition of scaled separation $r_{\rm sep}/R_{\rm vir}$ from Chamberlain et al. (2024), where $r_{\rm sep}$ is the physical separation in kpc, and $R_{\rm vir}$ is the virial radius of the pair's FoF group.[4] The virial radius of the pair's FoF group reasonably approximates the virial radius of a halo with a virial mass equal to the combined subhalo mass of the primary and secondary. This "scaled separation" is, by construction, a function of mass and redshift.

Note that we choose not to interpolate the orbits to get a more precise determination of the merger timescale, as the spread on the merger timescales in our study will be dominated by the variation of orbital configurations, rather than the uncertainty due to snapshot spacing. However, Patton et al. (2024) recently showed that for studies needing more precise determination of, e.g., pericenter passages or merger times, their 6D interpolation scheme can improve timing uncertainties from ±80Myr to ±3.3Myr.

Defining Post-Infall

While the orbit of a pair may be calculated at very early times, we wish to constrain our orbital analysis to only physically associated pairs, and thus will not consider the orbit of a subhalo pair before they belong to the same FoF group. Specifically, we will consider only the "post-infall" part of each pair's orbit.

We define the redshift of "first infall" as the redshift of the first snapshot where the primary and secondary have the same parent FoF halo, and post-infall as all following redshifts starting with the redshift of first infall.

Figure 4.1 presents a set of example orbits, which shows the wide variety of orbit-types

---

[3]If a subhalo is very small, or is passing through a more massive subhalo, and is unable to reach the density contrast required to be identified as an independent structure by the SUBFIND algorithm, it will not have a defined position in the SUBLINK catalogs. The SUBLINK algorithm allows for subhalos to skip a single snapshot, and identifies the 'skipped descendent' in the S_{n+2} snapshot, so that the orbit can be evaluated before and after the skip occurs. See Sec. 3 in Rodriguez-Gomez et al. (2015) for more details.

[4]Given by `Group_R_TopHat200` in the group catalogs. If the secondary is not in the same FoF group as the primary, the virial radius used to calculate the scaled separation will remain that of the primary's FoF group, which merging secondaries will eventually re-enter prior to merger.

that can be found in the TNG100 simulation for pairs that were originally selected from Ch. 3 at $z = 1.5$. The top panel shows the orbits of five pairs that merge, where solid lines show the post-infall parts of the orbit, and dashed lines show the pre-infall portions of the orbit before the secondary and primary ever share a FoF group halo. Even amongst galaxies of the same approximate stellar mass and stellar mass ratio, the spread of merger timescales can be very large, with merger timescales between $\sim 1 - 10\,\mathrm{Gyr}$ from first infall to merger (triangles).

For some pairs, the secondary subhalos can experience first infall, then after one pericentric passage can return to large distances where they are temporarily assigned a different FoF group halo than that of their primary. In these cases, we use the full orbit beginning at first infall, including the segments of the orbit where the secondary is assigned to another FoF group temporarily, through to merger as described in Section 4.2.2. This definition is most robust for considering the full interaction timescales of merging pairs.

The middle panel of Fig. 4.1 ("Potential Future Mergers") shows the orbits for three pairs that are classified as non-mergers, since they do not merge before $z = 0$, but which appear likely to merge within a few Gyr past the end of the simulation. These orbits can have a variety of orbital periods, and the number of pericentric passages can vary significantly. The two lighter blue orbits are very long period orbits with 1-2 pericenter passages in the past $10\,\mathrm{Gyr}$, while the darker blue orbit has a much shorter period with three close passages in just the past $2\,\mathrm{Gyr}$.

The bottom panel shows the orbits of "Fly-by" interactions (non-mergers) that are unlikely to merge in the near future, if ever. Note that we do not split our non-merger category into fly-bys and potential future mergers for any of our following analyses, and such distinctions were made only for the purposes of showing the diversity of selected orbits. We further discuss the role of non-mergers and fly-bys on our results in Sec. 4.5.2.

Uniqueness of Orbits

Since we collect the orbit for each pair at all redshifts after infall, a singular orbit will be selected as many times as the number of redshifts (or snapshots) where that pair exists. However, it is only necessary to keep a single instance of any given orbit in our catalog to

avoid skewing our data artificially to longer merger timescales.

To distinguish the collection of unique orbits, each pair is assigned a 'pairkey' while constructing their orbit. The pairkey is created by concatenating the earliest `SubhaloID` of the primary and secondary subhalo from the SUBLINK catalogs, and is unique for each pair of halos. After each pair is assigned a unique pairkey, we only keep one instance of an orbit per pair to avoid double/multi-counting in our orbit catalog.

Note that a single subhalo may be a member of many different pairs, but will only have one unique orbit per unique pair. For example, the primary of a low-mass pair selected at $z = 3$ that merges before $z = 2$ may be selected via our selection criteria again at $z = 1$ with a new secondary companion. In this case, both orbits (of the original low-mass pair and the new pair which includes the primary subhalo from the previous merger) are retained in the orbit catalog.

The total number of orbits, before removing the redundant orbits, is 71,429 for low-mass pairs, and 20,824 high-mass pairs. However, after removing all redundant orbits, there remain 22,213 low-mass orbits, and 3,029 high-mass orbits that each correspond to a unique pair of subhalos. The collection of all unique orbits constitutes our orbit sample and is the dataset that will be used for the remainder of this analysis.

4.3 Pair Sample Properties

4.3.1 Number of Pairs

The total number of pairs at a given redshift is equal to the number of orbits at that redshift, including both merger and non-merger pairs. A single, non-merging pair with first infall at $z = 3$ will contribute to the number of pairs at all redshifts from $z = 0 - 3$.

Figure 4.2 shows the number of low-mass and high-mass pairs as a function of redshift from $z = 0 - 6$. Low-mass pairs (green solid line) are most numerous between $z = 1.25 - 2$, while high-mass pairs (pink solid line) are most numerous between $z = 0 - 1$. The dashed lines show the number of unique pairs that merge prior to $z = 0$ for each sample. The number of pairs that merge decreases to zero at $z = 0$ since many pairs that exist at low redshift will have merger timescales that span beyond the end of the simulation (i.e., $z = 0$).

As subhalos experience first infall into a FoF group, the number of pairs increases. On the other hand, mergers simultaneously lead to a decrease in the number of pairs. The number of low-mass pairs increases from ~ 600 pairs at $z = 6$ to $\sim 6,600$ at $z = 2$. The decrease in the number of pairs after $z = 2$ means that the number of low-mass pairs that are merging at each redshift is larger than the rate at which pairs are added to the sample.

The number of high-mass pairs also increases until $z = 1$, at which point it remains approximately constant from $z = 0 - 1$ at ~ 1000 pairs. There is a slight decrease in the number of high mass pairs at the very lowest redshifts $z < 0.1$, where the mergers begin to outnumber the new pairs being added at each redshift.

In Fig. 1 of Ch. 3, the number of low-mass pairs peaks (with $\sim 3,000$ pairs) and begins to decrease at $z \sim 2$, and the number of high-mass pairs is approximately constant between $z = 0 - 1$, peaking at ~ 700 pairs. We find the same behavior with our pair sample, with low-mass pairs peaking at z=2 and high mass pairs leveling off between $z = 0 - 1$. However, in this study, the number of pairs at a given redshift is higher than in our previous work, since the orbit catalog includes a unique orbit for every pair from the previous work. For example, a pair that passes the Ch. 3 selection criteria only at $z = 1$ will only be counted as a pair at $z = 1$ in the previous work, while, in this study, it may be counted at many more redshifts since we can follow the orbit forwards and backwards in time.

4.3.2   Merger Fraction

We calculate the merger fraction by dividing the number of pairs that merge (dashed lines in Fig. 4.2) by the total number of merging and non-merging orbits (solid lines) at a given redshift. As before, an orbit with first infall at $z = 2$ and merger at $z = 1$ will be included in the merger fraction calculation for redshifts $z = 1 - 2$. Note, this definition of the merger fraction differs from that typically used in observational studies, where merger fractions are computed from close pair fractions with a correction term (e.g., Ventou et al., 2019).

Figure 4.3 shows the fraction of isolated pairs of low-mass (green) and high-mass (pink) pairs that merge before the end of the simulation as a function of redshift. At redshifts $z > 2$, the merger fraction for low-mass and high-mass pairs is greater than 0.9. The merger fraction for both mass ranges declines to zero at $z = 0$, due to the very small fraction of pairs at low
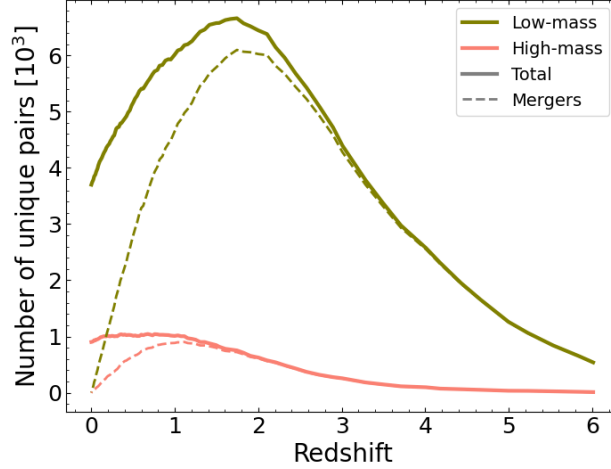
Figure 4.2: The number of unique low-mass (green) and high-mass (pink) pairs in our orbit catalog as a function of redshift. Orbits are only defined between first infall and the merger redshift (for merging pairs) or $z = 0$ (for non-merging pairs). The solid lines show the total number of pairs at a given redshift (including non-mergers and mergers), while dashed lines show the number of pairs at a given redshift that will merge before $z = 0$. The decrease in the number of unique low-mass pairs from $z = 2$ to $z = 0$ is due to pairs being removed from the sample via mergers.

redshift ($z < 1$) that have short enough merger timescales to merge before $z = 0$.

The merger fraction of low-mass and high-mass pairs is the same from $z = 0 - 0.5$ and $z = 2.5 - 6$. Between $z = 0.5 - 2.5$, the high-mass merger fraction is larger than the low-mass merger fraction, and the knee of the merger fraction occurs at a lower redshift. We discuss this difference in more detail in Sec. 4.5.2.

Note that the merger fraction defined here is a measure of the fraction of isolated pairs that merge before $z = 0$. It is not, however, a measure of the fraction of *all* low-mass and high-mass pairs in all environments that will merge.

4.4 Results: The Mass and Redshift Dependence of Merger Timescales

Using our sample of isolated low-mass and high-mass pairs in the TNG100 simulation, we calculate the merger timescales, or time until merger, for all of the merging pairs in sample. The merger timescale of a pair is defined to be the amount of time that elapses between the redshift at which pairs are selected and the merger redshift. Only the merging pairs will be considered for the remainder of the analysis.
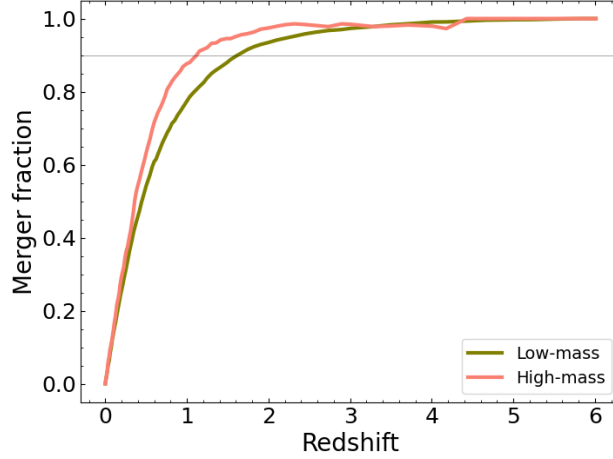
Figure 4.3: The fraction of low-mass (green) and high-mass (pink) orbits that merge before z=0 shown as a function of redshift. The horizontal line shows a merger fraction of 0.9, or 90%. High-mass pairs have merger fractions greater than 0.9 for $z > 1.1$, and low-mass pairs for $z > 1.6$. The sharp decline of the merger fraction to zero at low redshift is a non-physical feature of the simulation ending at $z = 0$. Only orbits with sufficiently short merger timescales will merge at redshifts $z <\sim 1$.

In Sec. 4.4.1, we explore how the merger timescale changes as a function of pair separation across redshifts for low-mass and high-mass pairs. In Sec. 4.4.2, we investigate the median time until merger for all pairs as a function of redshift. We will additionally examine the merger timescale's dependence on a variety of separation criteria. Separation criteria are applied to pairs at each redshift independently, such that a pair in the $10 - 50$ kpc bin at one redshift will not be part of the sample used at redshifts where its separation is > 50 kpc.

4.4.1 Separation Dependence of Merger Timescales

We calculate the time until merger as a function of separation for low-mass and high-mass pairs at a variety of redshifts from $z = 0.5 - 6$. Binning the pairs by separation, we can study how the merger timescale changes for pairs selected at different points in their orbits.

We bin our pair sample by merger timescale, in bins of 0.5Gyr, and separation bins of 20 kpc, and only consider the pairs with separations $r_{\mathrm{sep}} > 10$ kpc. Figure 4.4 shows a heatmap distribution of pairs as a function of merger timescale vs. separation for low-mass (top) and high-mass (bottom) pairs at redshifts $z = (0.5, 1, 1.5, 2, 3, 4, 5, 6)$. The colorbars to the right of each figure show the percentage of the population of pairs at that redshift that
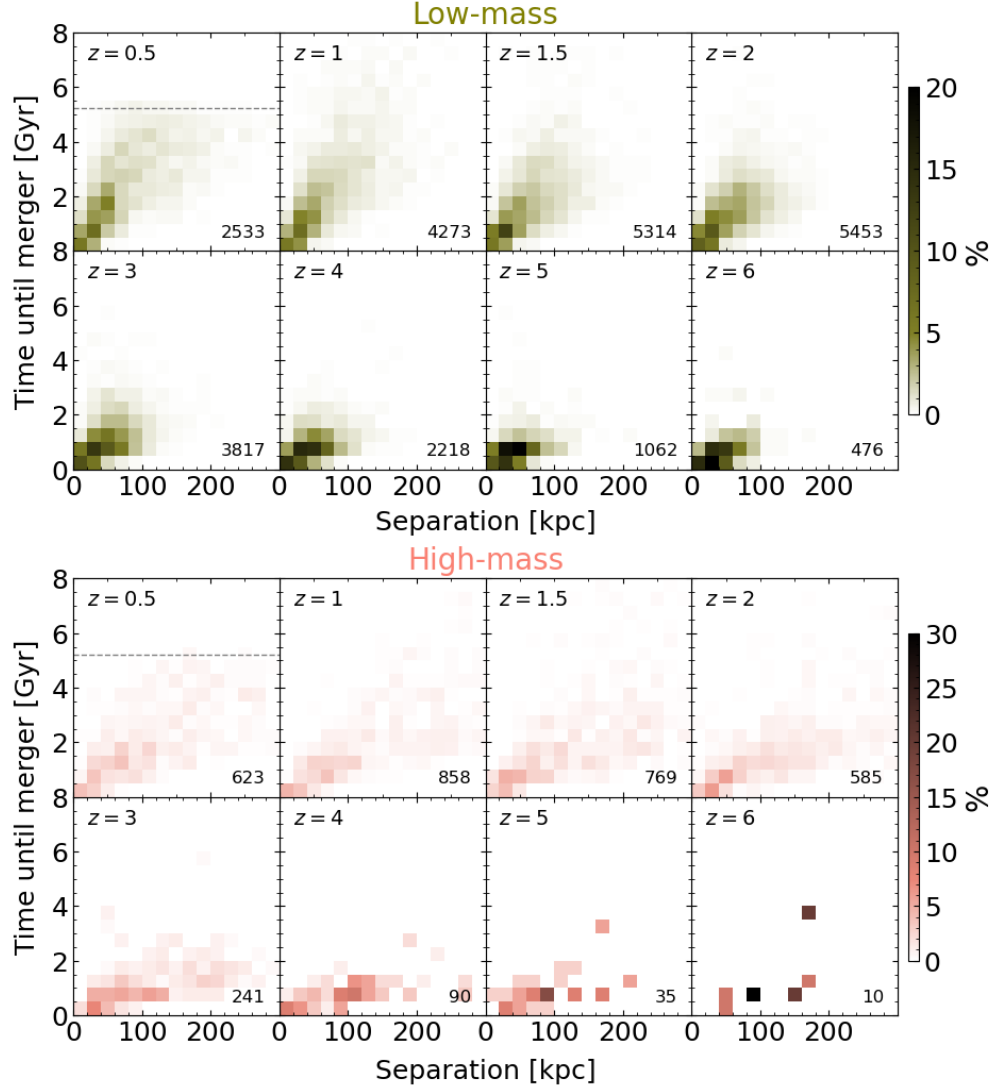
Figure 4.4: The distribution of merger timescales for low-mass (top) and high-mass (bottom) pairs as a function of physical separation at $z = 0.5, 1, 1.5, 2, 3, 4, 5$ and 6. The colorbars show the percentage of the total number of pairs at each redshift (given in the bottom right corner of each panel) that are in a given separation bin. In each of the first panels, the grey horizontal dashed line shows the time remaining in the simulation, above which there are no mergers. We find: i.) a positive correlation between separation and the time until merger at each selected redshift – the lowest separation pairs tend to have the shortest merger timescales; ii.) given a redshift and separation, the low-mass merger timescale is longer than the high-mass merger timescale, i.e. low-mass pairs at $z = 1$ with separations $r_{sep} < 100$ kpc merge within 6 Gyr, while high-mass pairs in the same separation range merge within 3 Gyr; iii.) merger timescales are longer for lower redshift pairs; iv.) the spread of merger timescales and separations increase with decreasing redshift.

are in each bin. The number of pairs at each redshift is printed in the bottom right corner of each panel. The horizontal line in the first panel shows the time remaining in the simulation until $z = 0$, above which no merging pairs exist.

We find that the merger timescale for low-mass and high-mass pairs is positively correlated with the separation of the pair at a given redshift. The merger timescale also increases with decreasing redshift for a given separation. For example, pairs at $z = 4$ with separations between $50 - 100$ kpc tend to merge in less time than pairs with the same separations at $z = 0.5$. For the same physical separation, the merger timescale of high-mass pairs is shorter than for low-mass at each redshift.

In addition, the spreads in the merger timescales and pair separations are smaller at higher redshift, for both low- and high-mass pairs. For example, the spread of merger timescales for low-mass pairs at $z = 1$ (4273 pairs) goes from $0 - 8\,\mathrm{Gyr}$, while pairs at $z = 4$ (2218 pairs) have merger timescales between $0 - 3\,\mathrm{Gyr}$. Likewise, the spread of separations at $z = 1$ is $0 - 200\,\mathrm{kpc}$, but at $z = 4$ the spread is smaller, between $10 - 125\,\mathrm{kpc}$. The high-mass pairs also have a larger spread in the distribution of merger timescales and separations at low redshift than at higher redshift. This is due to the growth of halos over time, and thus an increasing virial radius for FoF groups at lower redshifts.

Fig. 4.4 can be used to estimate the merger timescale of an isolated pair at a given redshift. For example, a low-mass pair at $z = 2$ with $r_{\mathrm{sep}} \sim 75$ kpc will merge in $0 - 5\,\mathrm{Gyr}$, with a most likely time to merger of around 2Gyr. On the other hand, a high-mass pair at $z = 2$ with $r_{\mathrm{sep}} \sim 75$ kpc will merge in $0 - 2\,\mathrm{Gyr}$, with a most likely merger timescale of around $0 - 1$Gyr.

4.4.2 Redshift Dependence of Merger Timescales

In this subsection, we study the merger timescales of low-mass and high-mass pairs as a function of redshift.

First, we consider the pair sample as a whole, and quantify the median merger timescale for all merging low- and high-mass pairs from $z = 0 - 6$. We then consider two sets of separation criteria to create separation-selected subsamples, as in Ch. 3, and study the impact of different selection criteria on the resulting merger timescales.

Full Sample

We calculate the merger timescales for pairs at each redshift, and quantify the median and spread on the merger timescale as a function of redshift in Fig. 4.5. We include the full catalog of merging orbits at each redshift, only excluding separations $r_{\text{sep}} < 10\,\text{kpc}$ to limit the impact of subhalos becoming indistinguishable in the SUBFIND catalogs.
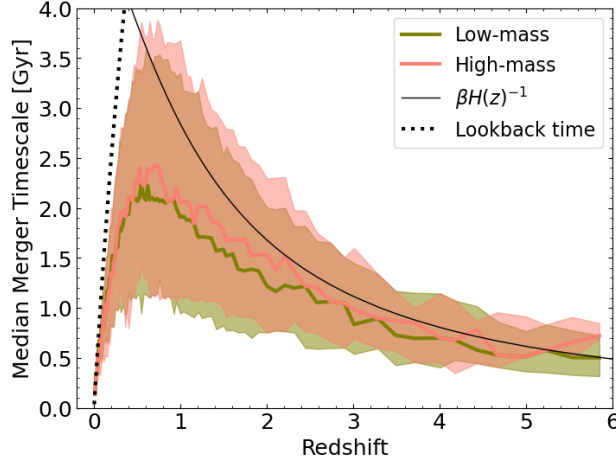
Figure 4.5: The median merger timescale as a function of redshift for low-mass (green) and high-mass (pink) pairs in our merger sample. Shaded regions represent the 1st and 3rd quartile spread on the median. The thick dotted black line at low redshifts shows the time to $z = 0$ (the lookback time) as a function of redshift, which sets the upper bound for the merger timescale that a merging pair can have. The thin black line shows the Hubble time as a function of redshift multiplied by a constant $\beta = 0.35$, which approximates the median time until merger from $z = 6$ to $z \sim 1$. The median time until merger is similar for low-mass and high-mass pairs, and rises from $z = 6$ to a peak at $z \sim 0.75$, then decreases to $z = 0$.

Figure 4.5 also shows the 1st and 3rd quartiles are indicated with shaded regions. Low-mass merger timescales (green) and high-mass merger timescales (pink) are roughly equivalent at all redshifts, which implies that mergers do not proceed in fundamentally different ways at different mass scales. We explore this point further in Sections 4.4.2 and 4.4.2.

The median time until merger is $\sim 0.5-0.7\,\text{Gyr}$ at $z \sim 6$, then rises to a peak of $2.3-2.4\,\text{Gyr}$ at $z \sim 0.6$, then decreases to zero at $z = 0$. The abrupt decrease is artificial rather than a true physical feature of merger timescales. As $z \to 0$, there is an increasingly small fraction of pairs that merge before $z = 0$, as seen by the dashed lines in Fig 4.2. These mergers must proceed on shorter timescales by definition, as they were selected as pairs that must merge prior to $z = 0$ (i.e., a pair at $z = 0.1$ that merges by $z = 0$ can have a maximal merger

timescale of 1.47Gyr, whereas a pair at $z = 1$ can have a maximal merger timescale of 8Gyr). This is shown by the dotted black line on the left of Fig. 4.5, which shows the lookback time of the simulation as a function of redshift.[5]

To understand the functional form of merger timescales between $z = 1 - 6$, which is shown by the thin black line in Fig. 4.5, we consider the following derivation. In principle, merger timescales for a body moving through a homogeneous field of collision-less matter can be analytically derived from the Chandrasekhar formula for dynamical friction (Binney and Tremaine, 2008).[6] Departures from the idealized case introduce perturbations to that solution, the validity of which has been tested in cosmological hydrodynamic and N-body simulations (Jiang et al., 2008; Boylan-Kolchin et al., 2008).

Such studies have found that the merger timescale in N-body hydrodynamic simulations is of the form

$$\tau_{\mathrm{merge}} = \frac{A(\Theta)}{\ln \Lambda} \frac{M_{\mathrm{prim}}}{M_{\mathrm{sec}}} \tau_{\mathrm{dyn}} \tag{4.1}$$

where M_{prim} and M_{sec} are the primary and secondary subhalo masses, $A(\Theta)$ is a constant for a given orbital configuration, $\ln \Lambda$ is the Coulomb logarithm taken to be $\ln \Lambda = \ln(1 + M_{\mathrm{prim}}/M_{\mathrm{sec}})$, and τ_{dyn} is the dynamical timescale at the virial radius of the primary subhalo. The dynamical timescale is related to the crossing time at the virial radius, and is given by

$$\tau_{\mathrm{dyn}} = \frac{R_{\mathrm{vir}}}{V_{\mathrm{circ}}(R_{\mathrm{vir}})}, \tag{4.2}$$

where $V_{\mathrm{circ}}(R_{\mathrm{vir}})$ is the circular velocity at the virial radius of the primary subhalo. Note that the dynamical time can thus be rewritten as

$$\tau_{\mathrm{dyn}} = (G\rho_{\mathrm{crit}})^{-1/2} = \left(\frac{3\, H^2(z)}{8\pi} \right)^{-1/2}. \tag{4.3}$$

In our study, we keep the stellar and FoF group mass criteria fixed as a function of redshift,

---

[5]The lookback time at a given redshift z_n is equivalent to the time elapsed between z_n and $z = 0$. Thus, merging pairs cannot have merger timescales larger than the lookback time of the simulation at a given redshift.

[6]Specifically, this derivation considers the merger timescale to be the time that elapses between the secondary subhalo crossing into the virial radius of the primary subhalo and the secondary's coalescence with the primary.

such that for a given pair, the merger timescale scales with redshift as

$$\tau_{\mathrm{merge}} \propto \tau_{\mathrm{dyn}} \propto \mathrm{H(z)}^{-1}, \tag{4.4}$$

assuming that there is no (or weak) redshift dependence of the distribution of orbital parameters. Thus, the merger timescale is expected to scale with the Hubble time at a given redshift.

In Fig. 4.5, the black dashed line shows the Hubble time $1/H(z)$ multiplied by $\beta = 0.35$. We did not perform a fit for this multiplicative constant, since we are interested in investigating the behavior of the merger timescale as a function of redshift rather than the specific values of the merger timescale. The redshift evolution of our median merger timescales is consistent with the scaling with $1/H(z)$ between $z =\sim 1 - 6$.[7]

It is notable that such a simple scaling holds for a complex simulation like TNG100 where subhalos are far from isotropic spherical distributions of mass. It is particularly interesting as well that low-mass and high-mass pairs have the same merger timescales *and* follow the $1/H(z)$ redshift scaling.

Physical Separation Selected Pairs

Since pair samples are typically picked via separation criteria in both simulations and observations, we study the impact of different separation-based selection criteria on inferred merger timescales. Separation selected samples have a lower separation criteria of 10 kpc. This lower separation criteria is also commonly applied to observationally selected pairs in studies of merger fractions and merger rates (see e.g. Lotz et al., 2011; Snyder et al., 2017; Besla et al., 2018, and observational studies cited therein).

The first set of separation criteria selects only pairs at a given redshift that have physical 3D separations greater than 10 kpc and less than $[50, 70, 100, 150, 200, \text{and } 300]$ kpc, yielding six pair subsamples. Pairs that are selected via the $r_{\mathrm{sep}} < 50$ kpc separation cut will be included in the $r_{\mathrm{sep}} < 70$ kpc subsample, and so on. These separation criteria do not vary as a function of time or mass, and are applied equivalently to the low-mass and high-mass

---

[7]$H(z)$ is calculated using the same cosmology as the TNG100 simulation, from Planck Collaboration et al. (2016). Specifically, $\Omega_M = 0.31$ and $\Omega_\Lambda = 0.69$.

samples at all redshifts. For example, an orbit in the separation bin < 50 kpc at $z = 2$ will not necessarily be in that same bin at other redshifts.

The top panel of Fig. 4.6 shows the merger timescale versus redshift for each of the low-mass (green) and high-mass (pink) pair subsamples with separations less than the physical separation listed above each panel. The same Hubble time redshift scaling from Sec. 4.4.2 is shown by the thin black line in each panel. We first note that the merger timescale peaks around redshift $z \sim 0.5$ for all low-mass and high-mass subsamples. In addition, all subsamples show the same decline of mean merger time as $z \to 0$, as discussed in the previous section. These traits are shown in Fig. 4.5, meaning they are features that are independent of separation criteria.

The subsamples with maximum separations of $[50, 70, \text{and } 100]$ kpc result in median merger timescales that are higher for low-mass pairs than high-mass pairs at all redshifts. The difference in the merger timescale is up to 0.8 Gyr longer for low-mass pairs than high-mass pairs at the same redshift for the same separation cut. The offset between the low-mass and high-mass merger timescale decreases for the largest separation cut of $r_{\text{sep}} < 300$ kpc. In the top rightmost panel, the median merger times converge for nearly all redshifts, similar to the merger timescales from the full sample shown in Fig. 4.5.

As the selection criteria increases (from left to right), each subsample contains a larger fraction of the full sample. The merger timescale for both low-mass and high-mass pairs increases with an increasing maximum separation cut. This follows directly from Sec. 4.4.1, where we found that the time until merger is positively correlated with increasing separation for all pairs. Including a higher fraction of larger-separation systems in each subsample increases the median time until merger at all redshifts.

The median merger timescale for low-mass pairs does not change significantly for any separation cuts above 150 kpc, which is larger than the average virial radius of low-mass systems at all redshifts. On the other hand, high-mass merger timescales tend to increase as separation increases. High-mass pairs tend to have higher separations than low-mass pairs, as shown in Sec. 4.4.1, due to the larger size of the high-mass subhalos.
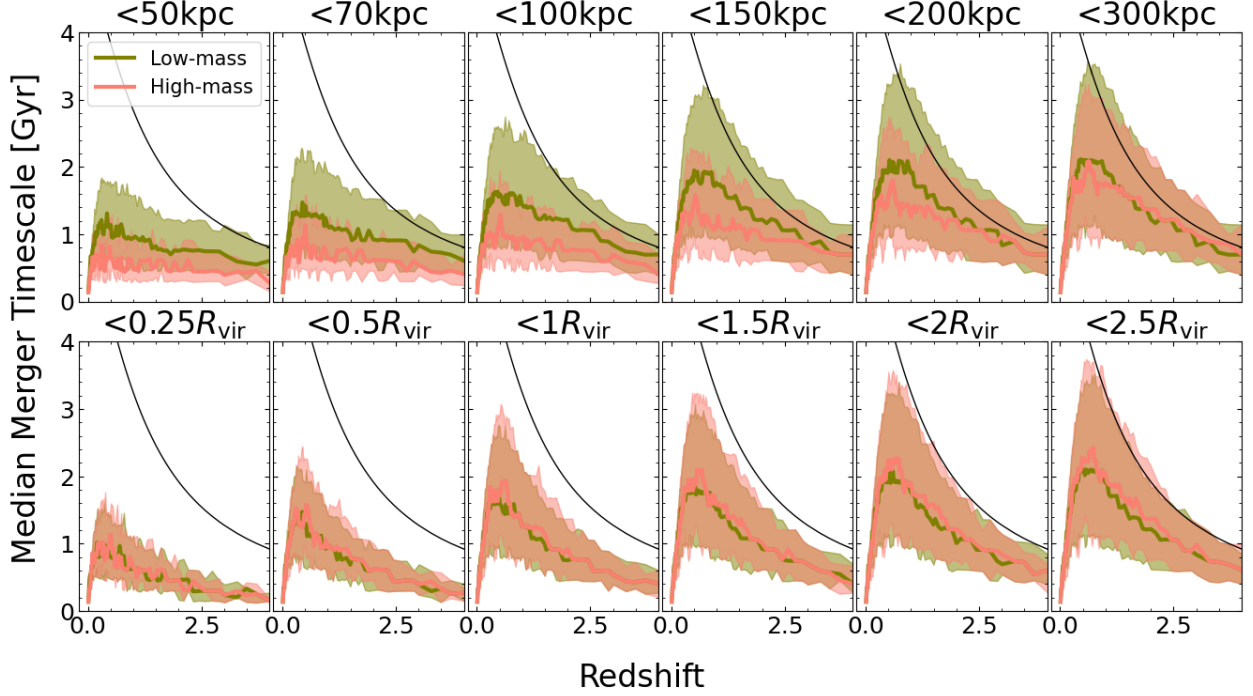
Figure 4.6: (Top) The median merger timescale as a function of redshift for low-mass (green) and high-mass (pink) pairs with 3D physical separations greater than 10 kpc and less than $50, 70, 100, 150, 200,$ and 300 kpc from left to right. (Bottom) The median time until merger as a function of redshift for pairs with physical separations greater than 10 kpc and less than $0.25, 0.5, 1, 1.5, 2,$ and $2.5 \, R_{\mathrm{vir}}$ from left to right. The thin black line is the same as shown in Fig. 4.5, and goes as the Hubble time $1/H(z)$ multiplied by 0.35 (see Sec. 4.4.2 for additional details). The time until merger increases from $z = 4$ to $z \sim 0.5 - 0.75$, at which point the time until merger decreases to zero since all low redshift mergers must have short merger timescales to merge before the end of the simulation at $z = 0$.

Scaled Separation Selected Pairs

We calculate the merger timescales for six additional subsamples of pairs, applying separation criteria that scale with both redshift and mass. The scaled separation, which we define in Section 4.2, is the separation of a pair divided by the virial radius of the pair's FoF group, R_{vir}. Scaled separation criteria select the equivalent *fraction* of the full volume of each FoF group, regardless of mass or redshift, whereas physical separation criteria will select the same volume around each primary, with no account for the growth of dark matter halos or spatial distributions of satellites. The scaled separation selected pairs have separations greater than 10 kpc and less than $[0.25, 0.5, 1, 1.5, 2, 2.5] \, R_{\mathrm{vir}}$. As in the previous section, the selection criteria are applied at each redshift independently.

As detailed in Ch. 3, the median virial radius for low-mass FoF groups at $z = [0, 1, 2, 3, 4]$ is approximately $[134, 85, 59, 43, 33]$ kpc, and for high-mass FoF groups is approximately $[348, 206, 134, 97, 76]$ kpc. Thus, choosing a scaled separation cut of $r_{\mathrm{sep}} < 1\, R_{\mathrm{vir}}$ at $z = 1$ will select low-mass pairs with separations $r_{\mathrm{sep}} \lesssim 85$ kpc and high-mass pairs with separations $r_{\mathrm{sep}} \lesssim 206$ kpc.

The bottom panel of Fig. 4.6 shows the median time until merger versus redshift for low-mass (green) and high-mass (pink) pair subsamples with scaled separations less than those listed at the top of each plot. As in the top row, the thin black line in each panel shows the Hubble time scaling derived in Sec. 4.4.2.

Quite unlike the physical separation selected subsamples in the top panels, using a scaled separation criteria results in nearly identical median merger timescales for low-mass and high-mass pairs at all redshifts. We find that the median time until merger at $z = 1$ for each scaled separation cut is about $\sim [0.64, 0.94, 1.25, 1.55, 1.85, 1.96]\,\mathrm{Gyr}$ respectively, for both low-mass and high-mass samples.

The median merger timescale starts off small at $z > 4$, then increases to a peak around $z \sim 0.6$, before quickly decreasing to zero at $z = 0$. This redshift evolution is similar to that of the full sample in Fig. 4.5.

The median time until merger at a given redshift increases. The low-mass and high-mass merger timescales increase for separation criteria that include a larger fraction of the virial radius, and thus larger separation pairs, but recover the behavior of the full sample by a separation cut of $2\, R_{\mathrm{vir}}$.

In addition, the slope of the merger timescale from $z = 6 \to 1$ is steeper for high-mass pairs in the scaled separation subsamples than the physical separation subsamples. This is especially noticeable in the first panel of the top and bottom rows, where the merger timescale of high-mass pairs is approximately flat for the physical separation cut $r_{\mathrm{sep}} < 50$ kpc.

4.5   Discussion

In this section, we will explore the implications and broader impacts of our merger timescale analysis, and put our study in context with previous work.

In Sec. 4.5.1, we return to one of the key questions posed in our previous work: what

are the underlying physical mechanisms that drive the difference in pair fraction evolution between low- and high-mass pairs? In Sec. 4.5.2, we will discuss the non-merger portion of our orbit sample and the difference between the merger fractions in the low-mass and high-mass regimes. Finally, in Sec. 4.5.3, we discuss the implications of our work for future observational and theoretical merger fraction and merger rate studies and provide suggestions for a self-consistent framework moving forward.

4.5.1 Connections to Pair Fractions

In our previous work (Chamberlain et al., 2024), we found that the pair fractions of isolated low-mass and high-mass pairs evolve very differently from $z = 0 - 2.5$ (see their Fig. 3). Low-mass major pair fractions are constant for $z > 2.2$, but decrease by almost 70% from $z = 3$ to $z = 0$. High-mass major pair fractions slowly increase from $z = 6$ to $z = 0$, with a more significant increase from $z = 0.25$ to $z = 0$. In short, the redshift evolution of pair fractions is opposite for low-mass pairs (which have a decreasing pair fraction with decreasing redshift) and high-mass pairs (which have an increasing pair fraction with decreasing redshift) from $z = 3 \rightarrow 0$.

Ch. 3 suggested a hypothesis for the difference in the behavior of the pair fractions: that perhaps low- mass and high-mass pairs have different merger timescales, which could lead to a difference in pair fractions from high to low redshift.

However in the present study, we have shown that the merger timescales of the full sample of low-mass and high-mass pairs are approximately equal at all redshifts, meaning that the opposing behaviour of low-mass and high-mass pair fractions is not a result of different merger timescales. Rather, we suspect that the build-up of larger structures due to hierarchical formation under ΛCDM leads to a reduced number of low-mass groups that enter the analysis at lower redshift. Additionally through this study, we have found that a significant fraction of the pairs selected in our previous work do indeed merge ($> 90\%$ of pairs for $z > 1.6$), so that the rate at which mergers occur is likely larger than the rate at which isolated low-mass pairs form, particularly at low redshift, thus leading to the quickly declining pair fraction measured in our previous work.

4.5.2 Non-merger Population

In our catalog of 22,213 low-mass pairs and 3,029 high-mass pairs, only 3700 (16.66%) low-mass pairs and 903 (29.71%) high-mass pairs do not merge by $z = 0$ (i.e. are classified here as "non-mergers"). In Sec. 4.3.2, we found that the merger fraction of low-mass and high-mass pairs at $z > 3$ is > 0.95 and the merger fraction decreases substantially at $z < 3$. While the decline in the merger fraction at $z \lesssim 1$ is primarily due to the limited time that a pair will have to merge before the end of the simulation, we also find that between $z =\sim 0.6 - 2.5$ the fraction of low-mass pairs is lower than that of high-mass pairs.

As in the previous subsection, one possible hypothesis that could explain the merger fraction differences is that low-mass pairs have shorter merger timescales than high-mass pairs, such that their mergers would occur at earlier times in the simulation leading to a decrease in the merger fraction at higher redshifts compared to high-mass pairs. However, we have shown that the merger timescales of our full low-mass and high-mass pair sample evolve similarly for $z = 0 - 6$ which means that the difference in the low- and high-mass merger fraction between $z = 0.5 - 2.5$ is not a result of a difference in merger timescales.

We suspect that the cause of the difference between low- and high-mass merger fractions is not a difference in the merging population itself, but rather in the non-merger population and its evolution over time. As we do not categorize our non-merging sample into "likely mergers" and "fly-by interactions" subsamples for this study (see Fig. 4.1), we cannot comment on how these two populations individually contribute to the difference in merger fractions. However, one possible explanation could be that a larger fraction of infalling low-mass pairs at lower redshift results in fly-by interactions. This could be the case if the velocity at which the secondary subhalo enters the primary's FoF group becomes increasingly large compared to the virial velocity[8], resulting in fewer bound systems. This phenomena will be tested in future work.

---

[8]The virial velocity is the value of the circular velocity at the virial radius.

4.5.3 Implications and Suggestions for Future Observational and Theoretical Studies of Pairs

While we are unable to make direct comparisons with previous observational studies of merger fractions and merger rates, as our study uses true physical separations from the simulation rather than projected separations, we can still draw meaningful conclusions about the application of our results to future studies of merger timescales and merger rates.

Pair Selection Criteria and Merger Rates in Illustris

Comparisons between studies of pair fractions, merger fractions, and merger rates, especially across cosmic time and different mass scales, are often challenged by the implementation of different selection criteria in each study.

In some observational studies, pair selection criteria are often set by the observational parameters of the survey itself. For example, limiting magnitudes and completeness limits can dictate which range of stellar masses and stellar mass ratios are considered (Patton et al., 2000; Lotz et al., 2008; Man et al., 2016; Ventou et al., 2019). Additionally, specific separation criteria may be chosen to avoid fiber collisions in a spectroscopic survey (as in Patton et al., 2011; Besla et al., 2018).

In theoretical studies, it is more straightforward to adopt several different pair selection criteria simultaneously for comparisons to specific observational studies (i.e. Lotz et al., 2011; Rodriguez-Gomez et al., 2015; Besla et al., 2018; Snyder et al., 2023). However, this then limits theoretical studies to a subset of pair selection criteria specific to their target comparison studies.

In recent years, some work has aimed to standardize pair selection criteria for future studies, in particular, to facilitate a fair comparison between theory and observations. One such study is Ventou et al. (2019), which created mock catalogs from the original Illustris-1 simulation to analyze the merger probability of galaxy pairs as a function of (both physical and projected) separation and relative velocity. They find that selecting pairs with projected separations between $5 \leq r_{\mathrm{proj}} \leq 50$ kpc and projected relative velocities of $v_{\mathrm{proj}} \leq 300\,\mathrm{km\,s^{-1}}$ selects all pairs that have greater than 30% chance of merging before $z = 0$. These selection criteria are

calibrated to select a population of pairs that are fairly likely to merge. Using their projected separation vs velocity analysis of merger probabilities, they also develop a weighting scheme to determine the likelihood of merger as a function of projected separation and velocity, which provides a way to more accurately calibrate merger fractions from close pair fractions. While their study considers the impact of stellar mass and redshift on the probability of merger, their suggested pair selection criteria do not vary with mass or redshift, which we have shown is crucial for interpreting and comparing pair fractions and merger timescales.

Rodriguez-Gomez et al. (2015) constructed galaxy merger trees to calculate the galaxy merger rate as a function of the stellar mass of the descendent subhalo and redshift in the original Illustris simulation. They find that the galaxy merger rate increases with increasing redshift for descendent galaxy masses $M_* > 10^{10}$ M$_\odot$. These findings are consistent with predictions of the galaxy merger rate from semi-empirical models (Stewart et al., 2009; Hopkins et al., 2010a), and with merger rates derived from observational merger fraction measurements calibrated by the corrected observability timescales of Lotz et al. (2011).

Additionally, Rodriguez-Gomez et al. (2015) find that the major merger rate at $z \sim 0.1$ increases with increasing descendant subhalo mass. While the redshift evolution of merger rates are broadly consistent with observations, they find significant discrepancies with major merger rates of galaxies with $M_* < 10^{10}$ M$_\odot$ from Casteels et al. (2014), which used morphological merger signatures to estimate merger rates at low z. As the Rodriguez-Gomez et al. (2015) work is self-consistently carried out at all redshifts and descendant masses, Rodriguez-Gomez et al. (2015) suggest that the discrepancy arises from significant uncertainty in the observability timescales of galaxies with lower mass $M_* < 10^{10}$ M$_\odot$, since the timescales in Casteels et al. (2014) are calibrated using an extrapolation of gas fraction data that is only available for $M_* > 10^{10}$ M$_\odot$.

These results imply that the timescales used to convert observational merger fractions (determined either by weighted close pair fractions or by morphologically selected pairs) are sensitive to the mass ranges and redshifts at which they are valid, and attempting to make comparisons between theoretical predictions and observational measurements can lead to seemingly incompatible results. Our work provides a unique framework that will allow for more robust comparisons of theoretical and observational samples.

Implementing Scaled Separation Pair Selection Criteria in Future Studies

In our previous work, we studied the impact of different separation criteria on the recovered pair fractions of low-mass and high-mass pairs, and found that features of the redshift evolution of the pair fractions can only be distinguished by employing scaled separation criteria (Chamberlain et al., 2024). In the present work, we explore how these same set of selection criteria impact the recovered merger timescales. We find that the merger timescales of isolated low-mass and high-mass pairs evolve nearly identically between $z = 0 - 6$. All subsamples of our pair catalog from scaled separation cuts result in identical behavior of the low-mass and high-mass merger timescales as a function of redshift as well. On the other hand, selecting pairs using a static physical separation criteria results in merger timescales that evolve differently between the two mass scales, and can differ by 0.8Gyr.

These results translate to important implications for observational studies of merger rates, which are typically determined using physical separation-selected close pairs and merger timescales. Our work has shown that both of these quantities can vary significantly for different pair selection criteria and that physical separation criteria can eliminate the distinguishing features of pair fractions or the equivalence of merger timescales between low-mass and high-mass pairs.

We therefore promote the adoption of separation criteria that vary as a function of mass and redshift for future pair studies. In particular, we point out the importance of utilizing pair selection criteria that permit fair comparisons of pair properties in observational studies (i.e. pair fractions, merger timescales, merger rates, etc.), particularly when the goal of such a study is to quantify and compare the redshift evolution of pair properties at different mass scales.

Specifically, we suggest employing separation criteria based on the scaled separation of each pair. The application of a scaled separation as demonstrated here can be straightforwardly applied to observational studies. Since estimates of a pair's stellar masses are needed to quantify the mass ratio of the pair (which is commonly computed for merger rate studies), no further observational information is needed to develop mass and redshift evolving separation cuts.

We provide a step by step example of this application as follows. First, compute the associated dark matter masses from the observed stellar masses of the pair using a SMHM relation (in this study, we employ that of Moster et al., 2013). Next, calculate the virial radius of a dark matter halo with a virial mass equal to the sum of the dark matter masses of the pair. [9] Finally, determine the physical separation for each pair individually that corresponds to the scaled separation criteria adopted in the study.

The process of computing the dark matter halo masses of the observed galaxies typically introduces systematic error to an observational study. When converting from stellar mass to dark matter halo mass, the SMHM relationship can be sampled, i.e. by computing many realizations of the dark matter mass of each galaxy, in a similar fashion as performed in Ch. 3, to derive the associated spread introduced by the abundance matching process.

As a concluding note, we remind readers that our results are explicitly for isolated pairs, as outlined in Sec. 4.2. One strength of this approach is that we have been able to study dynamics that are inherent to the pairs themselves, rather than those that are a product of the environment. Low-mass and high-mass pair merger timescales in high density environments may evolve differently than in our findings. We leave the extension of this analysis to more high-density environments as the focus of future work.

4.6   Summary and Conclusions

In this study, we construct a sample of the orbits of isolated low-mass ($10^8 < M_* < 5 \times 10^9 \, \mathrm{M_\odot}$) and high-mass ($5 \times 10^9 < M_* < 10^{11} \, \mathrm{M_\odot}$) major pairs (stellar mass ratio $> 1:4$) from $z = 0 - 6$ in the TNG100 simulation. Orbits of pairs, i.e. the 3D physical separation between the pair as a function of time, are defined from the redshift at which the primary and secondary subhalo first share a common FoF group (i.e., 'first infall') to either $z = 0$ or

---

[9] We showed in Ch. 3 that the virial radius of a halo with mass given by the combined dark matter halo masses of the primary and secondary recovers the virial radius of the FoF group with approximately 98% accuracy. The virial radius can be calculated from

$$R_{\mathrm{vir}} = \sqrt[3]{\frac{3 \mathrm{M_{vir}}}{4\pi \Delta_c \rho_c}}, \tag{4.5}$$

where ρ_c is the critical density of the Universe, and Δ_c is the overdensity constant (see Binney and Tremaine, 2008).

the redshift at which the pair merges.

The sample consists of 22,213 unique low-mass orbits and 3,029 unique-high mass orbits, for which we quantify the merger fraction as a function of redshift. We calculate the merger timescales of low-mass and high-mass major pairs as a function of separation and separately as a function of redshift. Our goal is to identify the merger timescales of pairs in a cosmological framework and to identify differences in the redshift evolution of the merger timescale between low-mass and high-mass pairs.

Additionally, motivated by our previous work on the pair fractions of low-mass and high-mass pairs in Chamberlain et al. (2024) where we showed that the evolution of the pair fraction is sensitive to the separation criteria used to select the pairs, we seek to determine the corresponding impact of various selection criteria on the merger timescales of pairs. Specifically, we look at two sets of selection criteria, one which selects pairs via a static physical separation cut, and the other which selects pairs based on a separation cut that evolves with redshift and mass. This is especially important for studies that seek to study pair fractions, merger fractions, merger timescales, and merger rates at different mass scales and/or as a function of redshift.

Our main conclusions are as follows:

- The merger fraction of physically associated low-mass and high-mass pairs is high (> 0.9) at $z \gtrsim 1.5$ (see Fig. 4.3). However, the merger fraction declines rapidly to zero as $z \to 0$, due to the finite length of the simulation, which artificially reduces the number of pairs with enough time left to merge at low redshifts.

- The merger timescale of a pair at a given redshift increases with increasing pair separation. Additionally, for a given physical separation, high-mass pairs have a shorter merger timescale than low-mass pairs at the same redshift. For example, low-mass pairs at $z = 1$ with separations $r_{\mathrm{sep}} < 100$ kpc merge within $6\,\mathrm{Gyr}$, while high-mass pairs in the same separation range merge within $3\,\mathrm{Gyr}$ (see Fig. 4.4).

- The median merger timescale peaks around $z \sim 0.6$ at $\sim 2.1 - 2.4\mathrm{Gyr}$ for both low-mass and high-mass pairs. At redshifts $z \gtrsim 1$, the median merger timescale for the full sample of low-mass and high-mass pairs that merge prior to $z = 0$ declines with increasing

redshift at a rate proportional to $1/H(z)$ (see Fig. 4.5). At $z \lesssim 1$, the maximum merger timescale is constrained by the time remaining in the simulation for the pair to merge, which causes the median merger timescale to decline to zero at $z = 0$. The decrease in the merger time at low redshifts is artificial and not representative of the true merger timescales of pairs at low redshift.

- When pairs are selected via a scaled separation criteria, namely the pair separation scaled by the virial radius R_{vir} of the FoF group of the primary, low-mass and high-mass merger timescales are nearly identical at all redshifts. This holds for all scaled separation criteria considered $(0.25, 0.5, 1, 1.5, 2, \mathrm{and}\ 3\, R_{\mathrm{vir}})$. At $z = [0, 1, 2, 3, 4]$, a scaled separation of $1\, R_{\mathrm{vir}}$ corresponds to an average physical separation of $[134, 85, 59, 43, 33]\,$kpc for low-mass pairs and $[348, 206, 134, 97, 76]\,$kpc for high-mass pairs.

- When pairs are selected via a physical separation criteria (one that does not vary with redshift or with mass), the median merger timescales of low-mass and high-mass pairs differ by up to 0.8Gyr. Thus, using the same merger timescale for low-mass and high-mass close pair samples selected via a physical separation cut will result in biased merger rate estimates.

Studies have found that merger rates of galaxy pairs vary with redshift and with the mass of the pair (Stewart et al., 2009; Hopkins et al., 2010a; Rodriguez-Gomez et al., 2015). In our previous work, we found that the pair fraction of isolated pairs in TNG100 likewise evolves with redshift and mass (Chamberlain et al., 2024). In this paper, we show that the merger timescales of major pairs in TNG100 vary with redshift, but that low-mass and high-mass pairs have equal merger timescales at all redshifts from $z = 0 - 6$ if the correct separation selection criteria is used to pick equivalent samples of pairs.

These works together give a comprehensive framework for inferring merger rates via pair fractions and merger timescales at redshifts from at least $z = 0 - 6$, and for quantifying the differences between low-mass and high-mass pairs. Indeed, separation selection criteria that scale with the mass and redshift of the target system are crucial for interpreting pair properties in a self-consistent way. In the future, observatories such as the Rubin Observatory, the Roman Space Telescope, JWST, and future ELTs, will detect an abundance of low-mass

pairs at a wide range of redshifts, and our theoretical framework for interpreting these observations will be more critical than ever.

Chapter 5

Summary and Future Outlooks

Studies of interacting galaxy pairs are critical to quantify the role of interactions and mergers in driving galaxy evolution across cosmic time. In this dissertation, I studied the dynamics of galaxy pairs from the Local Group (LG) to $z = 6$, leveraging new high-precision measurements of LG galaxies and data from the Illustris TNG100 cosmological simulation. In Sec. 5.1, I give an overview of the main findings of this work. In Sec. 5.2, I discuss how this work has laid the groundwork for future Local Group mass measurements. Finally, in Sec. 5.3, I explore possible extensions of the frameworks presented in this dissertation, and other future prospects for studies of pair dynamics in simulations.

5.1 Summary

The dynamics of low-mass galaxies in the LG can impact inferences made from observations, in particular for our measurements of the LG mass and orbit implied by the observed dynamics of M31. The traditional Timing Argument model, which uses the relative dynamics of the MW–M31 to infer the LG mass, assumes that the frame of reference of the observed kinematics of M31 are the same as the frame of reference moving with the MW dark matter halo's center of mass. Recent measurements from Petersen and Peñarrubia (2021) showed that the MW stellar disk is moving with respect to stars in the outer halo, as predicted by high-resolution simulations of the LMC's infall into the MW halo (Gómez et al., 2015; Laporte et al., 2018a; Garavito-Camargo et al., 2019; Cunningham et al., 2020; Petersen and Peñarrubia, 2020; Garavito-Camargo et al., 2021). The MW travel velocity has both radial and transverse components with respect to M31, which means that the true kinematics of M31 with respect to the MW dark matter halo are not the same as the observed kinematics of M31 taken in

the reference frame moving with the MW disk.

I created a framework to incorporate a moving MW disk in the Timing Argument model in Chapter 2. Utilizing recent high-precision observational data of M31's proper motion, distance, and line of sight velocity along with the first measurements of the MW disk travel velocity, I showed that the inferred mass of the LG decreases by about 12% compared to Timing Argument models that do not account for the travel velocity. In addition, future measurements of the MW travel velocity with more distant stellar tracers in the MW's outer halo will likely result in an increase in the measured travel velocity, as predicted in Garavito-Camargo et al. (2021). Utilizing the framework I developed, I showed that increases in the measured MW travel velocity will lead to an even lower inferred LG mass, as well as an increasingly less eccentric MW–M31 orbit (Fig. 2.3). Eccentricity decreases by $\sim 5\%$ for the measured travel velocity of 32km s^{-1}, and up to 30% for larger travel velocities depending on the assumed observational dataset. Cosmological simulations have shown that the orbits of MW–M31-mass analogs are commonly non-radial, suggesting the MW–M31 interaction is likely more cosmologically expected than previously believed. Finally, I showed that the recent Gaia eDR3 proper motion measurements of M31 from Salomon et al. (2021) — considerably higher than previous HST proper motions from van der Marel et al. (2012b) — yield systematically higher LG masses and lower eccentricities than inferred using the HST proper motions. I discuss how future high-precision data will affect LG mass measurements in the coming decade in Sec. 5.2.

With updated measurements for the LG mass, I turned to cosmological simulations to place LG-like pairs in a cosmological context by studying how their frequency and dynamics evolve with redshift. Some pairs of the LG whose dynamics have been studied in detail at low z include the MW–LMC, MW–M31, LMC–SMC, and M31–M33 (see e.g., Kallivayalil et al., 2006a,b; Besla et al., 2007; Besla et al., 2010; Sohn et al., 2012; van der Marel et al., 2012b,a; Patel et al., 2017a; van der Marel et al., 2019). In cosmological simulations, it is rare ($\sim 2 - 3\%$) to find MW/M31-mass analogs with an LMC-mass companion that has similar separation and relative velocity to the LMC (Boylan-Kolchin et al., 2011; Patel et al., 2017a). Studying the pair fractions of LG-like pairs as a function of cosmic time provides insight about the rarity of these types of systems at all redshifts.

In Chapter 3, I explored the pair fractions of low-mass pairs ($10^8 < M_* < 5 \times 10^9 \, \mathrm{M_\odot}$) and high-mass pairs ($5 \times 10^9 \, \mathrm{M_\odot} < M_* < 10^{11} \, \mathrm{M_\odot}$) from $z = 0 - 4$ in the Illustris TNG100 cosmological simulation. The pair sample was split into 4 categories, namely low-mass major pairs, low-mass minor pairs, high-mass major pairs, and high-mass minor pairs, where major pairs have a secondary to primary mass ratio of $1 - 1 : 4$ and minor pairs have mass ratios between $1 : 4 - 1 : 10$. The low-mass minor pair sample contained analogs of the LMC–SMC pair at $z = 0$, while the low-mass major pair sample contained analogs of LMC–M33-mass pairs. High-mass major pairs in this pair sample are analogous to the MW–M31 pair at $z = 0$, and high-mass minor pairs are analogs of MW–LMC or M31–M33. I found that pair fractions of low-mass minor pairs (LMC–SMC-mass analogs) were more than $\sim 3\times$ higher at $z > 2$ than at $z = 0$, and that the low-mass major and minor pair fraction is lowest at $z = 0$. Thus, it was fairly uncommon to find low-redshift isolated LMC–SMC analogs, though they were more common at higher redshift. The pair fractions of MW–LMC-mass analogs (high-mass minor pairs) was approximately constant from $z = 0 - 4$. Finding dynamical matches to the true MW–LMC system (which have $r_\mathrm{sep} < 50 \, \mathrm{kpc}$ and $v_\mathrm{rel} > 100 \mathrm{km \, s^{-1}}$) is challenging at $z = 0$, but such MW–LMC dynamical analogs are more common at higher redshifts, where the average pair separation is lower and relative velocities are higher. The redshift evolution of high-mass pair fractions was dramatically different compared to low-mass pair fractions. Though both low- and high-mass pair fractions were approximately constant from $z = 4$ to $z = 2.5$, the high-mass major pair fractions increased from $z = 2$ to $z = 0$, peaking at $z = 0$, while the low-mass pair fraction decreased by $\sim 60\%$ from $z = 2$ to $z = 0$.

In addition, I showed that caution should be taken when choosing pair selection criteria for pair fraction studies, particularly for understanding results in a cosmological context. Standard pair fraction studies select pairs using physical separation criteria, such as projected separations of $r_\mathrm{proj} = 10 \, \mathrm{kpc} - 50 \, \mathrm{kpc}$, which do not change with redshift or for different mass scales (see e.g., Lotz et al., 2011; Man et al., 2016; Snyder et al., 2017; Besla et al., 2018; Duncan et al., 2019, and references therein). I showed that selecting a pair sample with physical separation cuts applied equivalently for low- and high-mass pairs washes out the recovered pair fractions, making it impossible to distinguish the difference between high-mass and low-mass pair fractions and their redshift evolution. On the other hand, pair fractions at

different mass scales and redshifts can be meaningfully compared if the pair sample is selected via separation criteria that vary as a function of mass and redshift. Specifically, I considered scaled separation criteria, where the physical separation is scaled by the virial radius of the FoF group halo, and found that the difference in pair fractions could be seen using a scaled separation cut of $1R_{\mathrm{vir}}$. At $z = 2$, the average R_{vir} for high-mass pairs was approximately $130\,\mathrm{kpc}$, while for low-mass pairs R_{vir} was approximately $60\,\mathrm{kpc}$. This has lasting implications for future observational studies, which may need to reconsider how observational pair samples are defined in the future.

In Chapter 4, I extended the pair selection criteria framework to merger timescales. I calculated the orbits and merger timescales, from $z = 0 - 6$, of the sample of low- and high-mass pairs from the previous pair fraction study, specifically focusing on the major pairs. Orbits and merger timescales can put the rarity of, for example, MW–M31-mass systems into context and show how these systems change dynamically with time. I found that merger timescales of low-mass and high-mass major pairs are identical at redshifts from $z = 0 - 6$ for the full sample of pairs. However, extending the framework from Ch. 3, I also found that the merger timescales of low-mass and high-mass pairs are only equivalent if pairs are chosen via a scaled separation scheme. Selecting pairs with physical separation cuts that do not vary as a function of mass or redshift lead to low-mass and high-mass merger timescales that differ by up to 1Gyr.

For one, it was not clear that low-mass and high-mass pairs should have identical merger timescales when scaled by the size of their FoF halo, given that low-mass galaxies have shallower potential wells, larger gas fractions, etc. Instead, the median merger timescale for a pair scaled primarily with the dynamical time, or crossing time, of the FoF halo, but was independent of the mass scale. Thus, a pair with the same orbital parameters at separation $1R_{\mathrm{vir}}$ will merge at approximately the same time in a low-mass halo or in a high-mass halo. However, a low-mass pair with separation $r_{\mathrm{sep}} = 50\,\mathrm{kpc}$ will take *longer* to merge than a high-mass pair with a separation of $r_{\mathrm{sep}} = 50\,\mathrm{kpc}$ at any given redshift, so pair selection criteria are of critical importance when translating close pair fractions to merger rates using merger timescales. Although this study focused on major pairs specifically, I speculate that the merger timescales of scaled-separation selected minor pairs would also be equivalent

between high- and low-mass pairs (see Sec. 5.3 for more discussion).

Overall, this dissertation contextualized the rarity of LG-like systems as a function of time, and set up new frameworks for interpretations of pair-related properties such as pair fractions, merger timescales, and merger rates. They additionally demonstrate the importance of theoretically driven frameworks for interpretations of observations at different mass scales and redshifts, and also for observations of our own Local Group.

5.2   The Unification of High-Precision Data and Theory for Local Group Mass Estimates

High-precision data of the LG is only improving, as each new epoch of data provides better constraints on proper motion measurements. For example, proper motions for $G = 20$ sources (such as upper-giant-branch stars in M31) are expected to improve by a factor of six by the end of the Gaia survey (Gaia Collaboration et al., 2016). This translates to improvements in proper motion measurements for LG galaxies, which can then be used to create tighter constraints on the orbital histories of LG satellites and improved mass measurements from dynamical studies. In addition, techniques to combine complementary data from HST, Gaia, JWST, and Roman Space Telescope will allow for more precise proper motion measurements, particularly at larger distances, which will push the boundary of LG studies (see e.g. Warfield et al., 2023).

These future data will enable more precise mass estimates of the Local Group and permit higher-fidelity orbital modeling, which is necessary to constrain the merger and accretion history of the MW and M31. I have shown that the measured travel velocity of the MW disk changes the inferred LG mass from the Timing Argument, and that observations of more distant stellar tracers will likely lead to larger travel velocity estimates. However, the MW is not the only galaxy in the Local Group impacted by the dynamics of massive satellites, and thus improvements to mass measurements of the LG will also need to consider perturbations to the M31 halo as well.

Although M33 is likely on first infall into the halo of M31 (Patel et al., 2017a; van der Marel et al., 2019), it is likely that M31 has also experienced a reflex motion of its stellar disk away from the center of its dark matter halo through long-range interaction from M33

and potentially its previous accretion history. With precise orbital modeling of M31 and its satellite population, it's possible to constrain the expected travel velocity of the M31 disk, which can be integrated into Timing Argument measurements of the LG mass via the methodology I put forth in Ch. 2. In the future, it may be possible to observationally constrain M31's travel velocity as well, via proper motion measurements of stars in the disk and outer halo.

5.3 Extending Frameworks for Pair Studies in Simulations and Observations

Here, I will provide an overview of future prospects for extensions of the frameworks presented in Chapters 3 and 4.

Minor Merger Timescales

In Ch. 4, I showed that the merger timescales of isolated low-mass major pairs are equivalent to high-mass major pairs, assuming the same fraction of the total volume of the FoF group is used for pair selection criteria. Additionally, I found that merger timescales of major pairs scale with dynamical timescale as $1/H(z)$. To understand how the merger timescales of major pairs translate to pairs such as the MW–LMC, M31–M33, or the LMC–SMC, this study can be extended into the minor pair regime by utilizing the pair catalogs and orbit calculation packages I developed in Ch. 3 and Ch. 4. Extending the merger timescale study to lower mass ratio pairs will further test the importance of the dynamical timescale in setting the merger timescale of a pair, and whether this functional form for the merger timescale is equivalently applicable to pairs with different mass ratios.

Orbits and Merger Timescales of Galaxies vs. Subhalos

As shown by simulations and observations of our own MW, galaxies may not necessarily reside at or have the same velocity as the center of mass of their outer dark matter halo. Throughout the pair fraction and merger timescale studies in this dissertation, I studied subhalo pairs specifically. Although I expect that the pair fractions component of this study would remain roughly equivalent, the merger timescale analysis of Chapter 4 may

reveal discrepancies between the merger timescales of dark matter halos and galaxies, as shown in Rodriguez-Gomez et al. (2015). Extending this study to galaxy merger timescales specifically would require the use of baryonic merger trees, which are not publicly available.[1] Alternatively, particle data at each snapshot can be used to compute the center of mass of the star particles only and the orbits can be interpolated as in Patton et al. (2024) to get more precise estimates of the merger timescale.

Pair Fractions and Merger Timescales of Non-isolated Pairs

The frameworks developed in Chapters 3 and 4 are specific to pairs that are isolated from more massive neighbors that may impact the fundamental dynamics of the pairs. Previous observational pair studies have employed physical separation requirements to establish isolation (see e.g. Geha et al., 2012, who studied field dwarf galaxies that were $> 1.5\,\mathrm{Mpc}$ from an L_* galaxy). Applying isolation criteria that use specific physical separation cuts to higher redshift systems may prove challenging due to projection effects and distance uncertainties. Additionally, it is unclear if the results presented herein hold true for pairs in all environments, or are specific to very well isolated systems only. Thus, determining the pair fractions and merger timescales of systems as a function of environment will be crucial for interpreting pair fractions from more crowded fields.

The frameworks I have developed to compare pair fractions and merger rates over different mass scales and redshifts can be extended to pairs in higher density environments. This would facilitate easier comparison with observational studies that are unable to guarantee isolation for their pair sample. Extending this framework to high density environments can be done with the TNG100 simulation, in much the same manner as performed in Chapter 3. Rather than selecting subhalo pairs as the most massive pairs in a FoF group (where the FoF group mass is not significantly more than the total mass of the primary and secondary), pairs could be selected from larger FoF groups by proximity. A FoF group with $M_h \sim 10^{14}\,\mathrm{M_\odot}$ can host many MW/M31-mass and LMC/M33-mass analogs, and thus could host numerous pairs. Then, the pair fractions and merger timescales of pairs can be calculated in bins of the

---

[1]The available TNG100 merger trees track the evolution and mergers of the dark matter components of each subhalo, rather than the baryonic matter.

number density of galaxies. However, this type of study would also be aided by incorporating projection effects, as discussed in more detail in the next subsection.

Separation Criteria Studies in Projection

Of particular importance is the need to facilitate direct comparisons of simulations and observations. This can be achieved by utilizing the frameworks established in this dissertation, which perform pair studies on scaled-separation-selected pair samples, and incorporating projection effects by constructing mock catalogs, which have already been utilized by a variety of studies (see Snyder et al., 2017; Besla et al., 2018; Ventou et al., 2019; Snyder et al., 2023; Guzmán-Ortega et al., 2023, for examples of works that perform pair studies in projection using the Illustris/IllustrisTNG simulation suites). One of the biggest unknowns involved in translating the scaled pair selection framework to observations is whether projection effects eliminate the ability of scaled-separation selected pair samples to provide self-consistent measurements of pair fractions.

By performing the analyses in Chapters 3 and 4 in projection, and by removing the FoF group isolation criteria, the measured pair fractions could be directly compared to observational studies. This would permit predictive comparisons of pair fractions between simulations and observations, as done in Snyder et al. (2017); Besla et al. (2018); Snyder et al. (2023). Additionally, if the scaled-separation criteria framework can still robustly recover the redshift and mass dependence of pair fractions and merger timescales, then this framework can directly facilitate tests of ΛCDM cosmologies by comparing the observed pair fractions and merger rates for low-mass and high-mass pairs with predictions from TNG100.

References

H. B. Akins, C. R. Christensen, A. M. Brooks, F. Munshi, E. Applebaum, A. Engelhardt, and L. Chamberland. Quenching Timescales of Dwarf Satellites around Milky Way-mass Hosts. *ApJ*, 909(2):139, Mar. 2021. doi: 10.3847/1538-4357/abe2ab.

P. Barmby, M. L. N. Ashby, L. Bianchi, C. W. Engelbracht, R. D. Gehrz, K. D. Gordon, J. L. Hinz, J. P. Huchra, R. M. Humphreys, M. A. Pahre, P. G. Pérez-González, E. F. Polomski, G. H. Rieke, D. A. Thilker, S. P. Willner, and C. E. Woodward. Dusty Waves on a Starry Sea: The Mid-Infrared View of M31. *ApJ*, 650(1):L45–L49, Oct. 2006. doi: 10.1086/508626.

P. Behroozi, C. Conroy, R. H. Wechsler, A. Hearin, C. C. Williams, B. P. Moster, L. Y. A. Yung, R. S. Somerville, S. Gottlöber, G. Yepes, and R. Endsley. The Universe at z ¿ 10: predictions for JWST from the UNIVERSEMACHINE DR1. *MNRAS*, 499(4):5702–5718, Dec. 2020. doi: 10.1093/mnras/staa3164.

P. S. Behroozi, R. H. Wechsler, and C. Conroy. The Average Star Formation Histories of Galaxies in Dark Matter Halos from z = 0-8. *ApJ*, 770(1):57, June 2013. doi: 10.1088/0004-637X/770/1/57.

D. Benisty, E. Vasiliev, N. W. Evans, A.-C. Davis, O. V. Hartl, and L. E. Strigari. Gaia Wins the Timing Argument. *arXiv e-prints*, art. arXiv:2202.00033, Jan. 2022.

M. Bennett and J. Bovy. Vertical waves in the solar neighbourhood in Gaia DR2. *MNRAS*, 482(1):1417–1425, Jan. 2019. doi: 10.1093/mnras/sty2813.

G. Besla. The Orbits and Total Mass of the Magellanic Clouds. *ArXiv e-prints*, Nov. 2015.

G. Besla, N. Kallivayalil, L. Hernquist, B. Robertson, T. J. Cox, R. P. van der Marel, and C. Alcock. Are the Magellanic Clouds on Their First Passage about the Milky Way? *ApJ*, 668:949–967, Oct. 2007. doi: 10.1086/521385.

G. Besla, N. Kallivayalil, L. Hernquist, R. P. van der Marel, T. J. Cox, and D. Kereš. Simulations of the magellanic stream in a first infall scenario. *The Astrophysical Journal Letters*, 721(2):L97, 2010. URL http://stacks.iop.org/2041-8205/721/i=2/a=L97.

G. Besla, D. R. Patton, S. Stierwalt, V. Rodriguez-Gomez, E. Patel, N. J. Kallivayalil, K. E. Johnson, S. Pearson, G. C. Privon, and M. E. Putman. The frequency of dwarf galaxy multiples at low redshift in SDSS versus cosmological expectations. *MNRAS*, 480(3): 3376–3396, Nov. 2018. doi: 10.1093/mnras/sty2041.

L. A. Bignone, P. B. Tissera, E. Sillero, S. E. Pedrosa, L. J. Pellizza, and D. G. Lambas. Non-parametric morphologies of mergers in the Illustris simulation. *MNRAS*, 465(1): 1106–1122, Feb. 2017. doi: 10.1093/mnras/stw2788.

J. Binney and S. Tremaine. *Galactic Dynamics: Second Edition.* Princeton University Press, 2008.

J. Bland-Hawthorn and O. Gerhard. The Galaxy in Context: Structural, Kinematic, and Integrated Properties. *Annual Review of Astronomy and Astrophysics*, 54:529–596, Sept. 2016. doi: 10.1146/annurev-astro-081915-023441.

L. Blecha, G. F. Snyder, S. Satyapal, and S. L. Ellison. The power of infrared AGN selection in mergers: a theoretical study. *MNRAS*, 478(3):3056–3071, Aug. 2018. doi: 10.1093/mnras/sty1274.

M. Boylan-Kolchin, C.-P. Ma, and E. Quataert. Dynamical friction and galaxy merging time-scales. *MNRAS*, 383(1):93–101, Jan. 2008. doi: 10.1111/j.1365-2966.2007.12530.x.

M. Boylan-Kolchin, G. Besla, and L. Hernquist. Dynamics of the Magellanic Clouds in a Lambda cold dark matter universe. *MNRAS*, 414:1560–1572, June 2011. doi: 10.1111/j. 1365-2966.2011.18495.x.

G. L. Bryan and M. L. Norman. Statistical Properties of X-Ray Clusters: Analytic and Numerical Comparisons. *ApJ*, 495:80–99, Mar. 1998. doi: 10.1086/305262.

S. Byrne-Mamahit, D. R. Patton, S. L. Ellison, R. Bickley, L. Ferreira, M. Hani, S. Quai, and S. Wilkinson. Interacting galaxies in the IllustrisTNG simulations - VII: the connection between the most luminous active galactic nuclei and galaxy interactions. *MNRAS*, 528(4): 5864–5879, Mar. 2024. doi: 10.1093/mnras/stae419.

E. Carlesi, Y. Hoffman, J. G. Sorce, and S. Gottlöber. Constraining the mass of the Local Group. *MNRAS*, 465(4):4886–4894, Mar. 2017. doi: 10.1093/mnras/stw3073.

K. R. V. Casteels, C. J. Conselice, S. P. Bamford, E. Salvador-Solé, P. R. Norberg, N. K. Agius, I. Baldry, S. Brough, M. J. I. Brown, M. J. Drinkwater, S. P. Driver, A. W. Graham, J. Bland-Hawthorn, A. M. Hopkins, L. S. Kelvin, A. R. López-Sánchez, J. Loveday, A. S. G. Robotham, and J. A. Vázquez-Mata. Galaxy And Mass Assembly (GAMA): refining the local galaxy merger rate using morphological information. *MNRAS*, 445(2):1157–1169, Dec. 2014. doi: 10.1093/mnras/stu1799.

K. Chamberlain, A. M. Price-Whelan, G. Besla, E. C. Cunningham, N. Garavito-Camargo, J. Peñarrubia, and M. S. Petersen. Implications of the Milky Way Travel Velocity for Dynamical Mass Estimates of the Local Group. *ApJ*, 942(1):18, Jan. 2023. doi: 10.3847/ 1538-4357/aca01f.

K. Chamberlain, G. Besla, E. Patel, V. Rodriguez-Gomez, P. Torrey, G. Martin, K. Johnson, N. Kallivayalil, D. Patton, S. Pearson, G. Privon, and S. Stierwalt. A Physically Motivated Framework to Compare Pair Fractions of Isolated Low- and High-mass Galaxies across Cosmic Time. *ApJ*, 962(2):162, Feb. 2024. doi: 10.3847/1538-4357/ad19d0.

K. T. E. Chua, A. Pillepich, V. Rodriguez-Gomez, M. Vogelsberger, S. Bird, and L. Hernquist. Subhalo demographics in the Illustris simulation: effects of baryons and halo-to-halo variation. *MNRAS*, 472(4):4343–4360, Dec. 2017. doi: 10.1093/mnras/stx2238.

J. M. Comerford, D. Pooley, R. S. Barrows, J. E. Greene, N. L. Zakamska, G. M. Madejski, and M. C. Cooper. Merger-driven Fueling of Active Galactic Nuclei: Six Dual and Offset AGNs Discovered with Chandra and Hubble Space Telescope Observations. *ApJ*, 806(2): 219, June 2015. doi: 10.1088/0004-637x/806/2/219.

C. Conroy, R. P. Naidu, N. Garavito-Camargo, G. Besla, D. Zaritsky, A. Bonaca, and B. D. Johnson. All-sky dynamical response of the Galactic halo to the Large Magellanic Cloud. *Nature*, 592(7855):534–536, Apr. 2021. doi: 10.1038/s41586-021-03385-7.

C. J. Conselice. The Relationship between Stellar Light Distributions of Galaxies and Their Formation Histories. *ApJS*, 147(1):1–28, July 2003. doi: 10.1086/375001.

S. Courteau and S. van den Bergh. The Solar Motion Relative to the Local Group. *AJ*, 118 (1):337–345, July 1999. doi: 10.1086/300942.

W. I. Cowley, C. M. Baugh, S. Cole, C. S. Frenk, and C. G. Lacey. Predictions for deep galaxy surveys with JWST from ΛCDM. *MNRAS*, 474(2):2352–2372, Feb. 2018. doi: 10.1093/mnras/stx2897.

E. C. Cunningham, N. Garavito-Camargo, A. J. Deason, K. V. Johnston, D. Erkal, C. F. P. Laporte, G. Besla, R. Luger, and R. E. Sanderson. Quantifying the Stellar Halo's Response to the LMC's Infall with Spherical Harmonics. *ApJ*, 898(1):4, July 2020. doi: 10.3847/ 1538-4357/ab9b88.

M. Davis, G. Efstathiou, C. S. Frenk, and S. D. M. White. The evolution of large-scale structure in a universe dominated by cold dark matter. *ApJ*, 292:371–394, May 1985. doi: 10.1086/163168.

A. J. Deason, D. Erkal, V. Belokurov, A. Fattahi, F. A. Gómez, R. J. J. Grand, R. Pakmor, X.-X. Xue, C. Liu, C. Yang, L. Zhang, and G. Zhao. The mass of the Milky Way out to 100 kpc using halo stars. *MNRAS*, 501(4):5964–5972, Mar. 2021. doi: 10.1093/mnras/staa3984.

P. Di Matteo, F. Bournaud, M. Martig, F. Combes, A. L. Melchior, and B. Semelin. On the frequency, intensity, and duration of starburst episodes triggered by galaxy interactions and mergers. *A&A*, 492(1):31–49, Dec. 2008. doi: 10.1051/0004-6361:200809480.

J. D. Diaz, S. E. Koposov, M. Irwin, V. Belokurov, and N. W. Evans. Balancing mass and momentum in the Local Group. *MNRAS*, 443(2):1688–1703, Sept. 2014. doi: 10.1093/ mnras/stu1210.

K. Dolag, S. Borgani, G. Murante, and V. Springel. Substructures in hydrodynamical cluster simulations. *MNRAS*, 399:497–514, Oct. 2009. doi: 10.1111/j.1365-2966.2009.15034.x.

G. A. Dooley, A. H. G. Peter, T. Yang, B. Willman, B. F. Griffen, and A. Frebel. An observer's guide to the (Local Group) dwarf galaxies: predictions for their own dwarf satellite populations. *MNRAS*, 471(4):4894–4909, Nov. 2017. doi: 10.1093/mnras/stx1900.

R. Drimmel and E. Poggio. On the Solar Velocity. *Research Notes of the American Astronomical Society*, 2(4):210, Nov. 2018. doi: 10.3847/2515-5172/aaef8b.

K. Duncan, C. J. Conselice, C. Mundy, E. Bell, J. Donley, A. Galametz, Y. Guo, N. A. Grogin, N. Hathi, J. Kartaltepe, D. Kocevski, A. M. Koekemoer, P. G. Pérez-González, K. B. Mantha, G. F. Snyder, and M. Stefanon. Observational Constraints on the Merger History of Galaxies since z ≈ 6: Probabilistic Galaxy Pair Counts in the CANDELS Fields. *ApJ*, 876(2):110, May 2019. doi: 10.3847/1538-4357/ab148a.

G. Eadie and M. Jurić. The Cumulative Mass Profile of the Milky Way as Determined by Globular Cluster Kinematics from Gaia DR2. *ApJ*, 875(2):159, Apr. 2019. doi: 10.3847/1538-4357/ab0f97.

S. L. Ellison, P. Nair, D. R. Patton, J. M. Scudder, J. T. Mendel, and L. Simard. The impact of gas inflows on star formation rates and metallicities in barred galaxies. *MNRAS*, 416(3): 2182–2192, Sept. 2011. doi: 10.1111/j.1365-2966.2011.19195.x.

S. L. Ellison, A. Viswanathan, D. R. Patton, C. Bottrell, A. W. McConnachie, S. Gwyn, and J.-C. Cuillandre. A definitive merger-AGN connection at z ˜ 0 with CFIS: mergers have an excess of AGN and AGN hosts are more frequently disturbed. *MNRAS*, 487(2):2491–2504, Aug. 2019. doi: 10.1093/mnras/stz1431.

D. Erkal, T. S. Li, S. E. Koposov, V. Belokurov, E. Balbinot, K. Bechtol, B. Buncher, A. Drlica-Wagner, K. Kuehn, J. L. Marshall, C. E. Martínez-Vázquez, A. B. Pace, N. Shipp, J. D. Simon, K. M. Stringer, A. K. Vivas, R. H. Wechsler, B. Yanny, F. B. Abdalla, S. Allam, J. Annis, S. Avila, E. Bertin, D. Brooks, E. Buckley-Geer, D. L. Burke, A. Carnero Rosell, M. Carrasco Kind, J. Carretero, C. B. D'Andrea, L. N. da Costa, C. Davis, J. De Vicente, P. Doel, T. F. Eifler, A. E. Evrard, B. Flaugher, J. Frieman, J. García-Bellido, E. Gaztanaga, D. W. Gerdes, D. Gruen, R. A. Gruendl, J. Gschwend, G. Gutierrez, W. G. Hartley, D. L. Hollowood, K. Honscheid, D. J. James, E. Krause, M. A. G. Maia, M. March, F. Menanteau, R. Miquel, R. L. C. Ogando, A. A. Plazas, E. Sanchez, B. Santiago, V. Scarpine, R. Schindler, I. Sevilla-Noarbe, M. Smith, R. C. Smith, M. Soares-Santos, F. Sobreira, E. Suchyta, M. E. C. Swanson, G. Tarle, D. L. Tucker, and A. R. Walker. Modelling the Tucana III stream - a close passage with the LMC. *MNRAS*, 481(3): 3148–3159, Dec. 2018. doi: 10.1093/mnras/sty2518.

D. Erkal, V. Belokurov, C. F. P. Laporte, S. E. Koposov, T. S. Li, C. J. Grillmair, N. Kallivayalil, A. M. Price-Whelan, N. W. Evans, K. Hawkins, D. Hendel, C. Mateu, J. F. Navarro, A. del Pino, C. T. Slater, S. T. Sohn, and Orphan Aspen Treasury Collaboration. The total mass of the Large Magellanic Cloud from its perturbation on the Orphan stream. *MNRAS*, 487(2):2685–2700, Aug. 2019. doi: 10.1093/mnras/stz1371.

D. Erkal, V. A. Belokurov, and D. L. Parkin. Equilibrium models of the Milky Way mass are biased high by the LMC. *MNRAS*, 498(4):5574–5580, Nov. 2020. doi: 10.1093/mnras/staa2840.

D. Erkal, A. J. Deason, V. Belokurov, X.-X. Xue, S. E. Koposov, S. A. Bird, C. Liu, I. T. Simion, C. Yang, L. Zhang, and G. Zhao. Detection of the LMC-induced sloshing of the Galactic halo. *MNRAS*, 506(2):2677–2684, Sept. 2021. doi: 10.1093/mnras/stab1828.

M. A. Fardal, M. D. Weinberg, A. Babul, M. J. Irwin, P. Guhathakurta, K. M. Gilbert, A. M. N. Ferguson, R. A. Ibata, G. F. Lewis, N. R. Tanvir, and A. P. Huxor. Inferring the Andromeda Galaxy's mass from its giant southern stream with Bayesian simulation sampling. *MNRAS*, 434(4):2779–2802, Oct. 2013. doi: 10.1093/mnras/stt1121.

A. Fattahi, J. F. Navarro, E. Starkenburg, C. R. Barber, and A. W. McConnachie. Galaxy pairs in the local group. *MNRAS*, 431:L73–l77, Apr. 2013. doi: 10.1093/mnrasl/slt011.

I. Ferreras, I. Trujillo, E. Mármol-Queraltó, P. G. Pérez-González, A. Cava, G. Barro, J. Cenarro, A. Hernán-Caballero, N. Cardiel, J. Rodríguez-Zaurín, and M. Cebrián. Constraints on the merging channel of massive galaxies since z $\sim$ 1. *MNRAS*, 444(1):906–918, Oct. 2014. doi: 10.1093/mnras/stu1425.

S. P. Fillingham, M. C. Cooper, M. Boylan-Kolchin, J. S. Bullock, S. Garrison-Kimmel, and C. Wheeler. Environmental quenching of low-mass field galaxies. *MNRAS*, 477(4): 4491–4498, July 2018. doi: 10.1093/mnras/sty958.

C. Flynn, J. Holmberg, L. Portinari, B. Fuchs, and H. Jahreiß. On the mass-to-light ratio of the local Galactic disc and the optical luminosity of the Galaxy. *MNRAS*, 372(3): 1149–1160, Nov. 2006. doi: 10.1111/j.1365-2966.2006.10911.x.

A. S. Font, K. V. Johnston, P. Guhathakurta, S. R. Majewski, and R. M. Rich. Dynamics and Stellar Content of the Giant Southern Stream in M31. II. Interpretation. *AJ*, 131(3): 1436–1444, Mar. 2006. doi: 10.1086/499564.

J. E. Forero-Romero, Y. Hoffman, S. Bustamante, S. Gottlöber, and G. Yepes. The Kinematics of the Local Group in a Cosmological Context. *ApJ*, 767(1):L5, Apr. 2013. doi: 10.1088/2041-8205/767/1/l5.

T. K. Fritz, A. Di Cintio, G. Battaglia, C. Brook, and S. Taibi. The mass of our Galaxy from satellite proper motions in the Gaia era. *MNRAS*, 494(4):5178–5193, June 2020. doi: 10.1093/mnras/staa1040.

Gaia Collaboration, T. Prusti, J. H. J. de Bruijne, A. G. A. Brown, A. Vallenari, C. Babusiaux, C. A. L. Bailer-Jones, U. Bastian, M. Biermann, D. W. Evans, L. Eyer, F. Jansen, C. Jordi, S. A. Klioner, U. Lammers, L. Lindegren, X. Luri, F. Mignard, D. J. Milligan, C. Panem, V. Poinsignon, D. Pourbaix, S. Randich, G. Sarri, P. Sartoretti, H. I. Siddiqui, C. Soubiran, V. Valette, F. van Leeuwen, N. A. Walton, C. Aerts, F. Arenou, M. Cropper, R. Drimmel, E. Høg, D. Katz, M. G. Lattanzi, W. O'Mullane, E. K. Grebel, A. D. Holland, C. Huc, X. Passot, L. Bramante, C. Cacciari, J. Castañeda, L. Chaoul, N. Cheek, F. De Angeli,

C. Fabricius, R. Guerra, J. Hernández, A. Jean-Antoine-Piccolo, E. Masana, R. Messineo, N. Mowlavi, K. Nienartowicz, D. Ordóñez-Blanco, P. Panuzzo, J. Portell, P. J. Richards, M. Riello, G. M. Seabroke, P. Tanga, F. Thévenin, J. Torra, S. G. Els, G. Gracia-Abril, G. Comoretto, M. Garcia-Reinaldos, T. Lock, E. Mercier, M. Altmann, R. Andrae, T. L. Astraatmadja, I. Bellas-Velidis, K. Benson, J. Berthier, R. Blomme, G. Busso, B. Carry, A. Cellino, G. Clementini, S. Cowell, O. Creevey, J. Cuypers, M. Davidson, J. De Ridder, A. de Torres, L. Delchambre, A. Dell'Oro, C. Ducourant, Y. Frémat, M. García-Torres, E. Gosset, J. L. Halbwachs, N. C. Hambly, D. L. Harrison, M. Hauser, D. Hestroffer, S. T. Hodgkin, H. E. Huckle, A. Hutton, G. Jasniewicz, S. Jordan, M. Kontizas, A. J. Korn, A. C. Lanzafame, M. Manteiga, A. Moitinho, K. Muinonen, J. Osinde, E. Pancino, T. Pauwels, J. M. Petit, A. Recio-Blanco, A. C. Robin, L. M. Sarro, C. Siopis, M. Smith, K. W. Smith, A. Sozzetti, W. Thuillot, W. van Reeven, Y. Viala, U. Abbas, A. Abreu Aramburu, S. Accart, J. J. Aguado, P. M. Allan, W. Allasia, G. Altavilla, M. A. Álvarez, J. Alves, R. I. Anderson, A. H. Andrei, E. Anglada Varela, E. Antiche, T. Antoja, S. Antón, B. Arcay, A. Atzei, L. Ayache, N. Bach, S. G. Baker, L. Balaguer-Núñez, C. Barache, C. Barata, A. Barbier, F. Barblan, M. Baroni, D. Barrado y Navascués, M. Barros, M. A. Barstow, U. Becciani, M. Bellazzini, G. Bellei, A. Bello García, V. Belokurov, P. Bendjoya, A. Berihuete, L. Bianchi, O. Bienaymé, F. Billebaud, N. Blagorodnova, S. Blanco-Cuaresma, T. Boch, A. Bombrun, R. Borrachero, S. Bouquillon, G. Bourda, H. Bouy, A. Bragaglia, M. A. Breddels, N. Brouillet, T. Brüsemeister, B. Bucciarelli, F. Budnik, P. Burgess, R. Burgon, A. Burlacu, D. Busonero, R. Buzzi, E. Caffau, J. Cambras, H. Campbell, R. Cancelliere, T. Cantat-Gaudin, T. Carlucci, J. M. Carrasco, M. Castellani, P. Charlot, J. Charnas, P. Charvet, F. Chassat, A. Chiavassa, M. Clotet, G. Cocozza, R. S. Collins, P. Collins, G. Costigan, F. Crifo, N. J. G. Cross, M. Crosta, C. Crowley, C. Dafonte, Y. Damerdji, A. Dapergolas, P. David, M. David, P. De Cat, F. de Felice, P. de Laverny, F. De Luise, R. De March, D. de Martino, R. de Souza, J. Debosscher, E. del Pozo, M. Delbo, A. Delgado, H. E. Delgado, F. di Marco, P. Di Matteo, S. Diakite, E. Distefano, C. Dolding, S. Dos Anjos, P. Drazinos, J. Durán, Y. Dzigan, E. Ecale, B. Edvardsson, H. Enke, M. Erdmann, D. Escolar, M. Espina, N. W. Evans, G. Eynard Bontemps, C. Fabre, M. Fabrizio, S. Faigler, A. J. Falcão, M. Farràs Casas, F. Faye, L. Federici, G. Fedorets, J. Fernández-Hernández, P. Fernique, A. Fienga, F. Figueras, F. Filippi, K. Findeisen, A. Fonti, M. Fouesneau, E. Fraile, M. Fraser, J. Fuchs, R. Furnell, M. Gai, S. Galleti, L. Galluccio, D. Garabato, F. García-Sedano, P. Garé, A. Garofalo, N. Garralda, P. Gavras, J. Gerssen, R. Geyer, G. Gilmore, S. Girona, G. Giuffrida, M. Gomes, A. González-Marcos, J. González-Núñez, J. J. González-Vidal, M. Granvik, A. Guerrier, P. Guillout, J. Guiraud, A. Gúrpide, R. Gutiérrez-Sánchez, L. P. Guy, R. Haigron, D. Hatzidimitriou, M. Haywood, U. Heiter, A. Helmi, D. Hobbs, W. Hofmann, B. Holl, G. Holland, J. A. S. Hunt, A. Hypki, V. Icardi, M. Irwin, G. Jevardat de Fombelle, P. Jofré, P. G. Jonker, A. Jorissen, F. Julbe, A. Karampelas, A. Kochoska, R. Kohley, K. Kolenberg, E. Kontizas, S. E. Koposov, G. Kordopatis, P. Koubsky, A. Kowalczyk, A. Krone-Martins, M. Kudryashova, I. Kull, R. K. Bachchan, F. Lacoste-Seris, A. F. Lanza, J. B. Lavigne, C. Le Poncin-Lafitte, Y. Lebreton, T. Lebzelter, S. Leccia, N. Leclerc, I. Lecoeur-Taibi, V. Lemaitre, H. Lenhardt, F. Leroux, S. Liao, E. Licata, H. E. P. Lindstrøm, T. A. Lister, E. Livanou, A. Lobel, W. Löffler, M. López, A. Lopez-Lozano, D. Lorenz, T. Loureiro, I. MacDonald, T. Magalhães Fernandes, S. Managau, R. G. Mann,

G. Mantelet, O. Marchal, J. M. Marchant, M. Marconi, J. Marie, S. Marinoni, P. M. Marrese, G. Marschalkó, D. J. Marshall, J. M. Martín-Fleitas, M. Martino, N. Mary, G. Matijevič, T. Mazeh, P. J. McMillan, S. Messina, A. Mestre, D. Michalik, N. R. Millar, B. M. H. Miranda, D. Molina, R. Molinaro, M. Molinaro, L. Molnár, M. Moniez, P. Montegriffo, D. Monteiro, R. Mor, A. Mora, R. Morbidelli, T. Morel, S. Morgenthaler, T. Morley, D. Morris, A. F. Mulone, T. Muraveva, I. Musella, J. Narbonne, G. Nelemans, L. Nicastro, L. Noval, C. Ordénovic, J. Ordieres-Meré, P. Osborne, C. Pagani, I. Pagano, F. Pailler, H. Palacin, L. Palaversa, P. Parsons, T. Paulsen, M. Pecoraro, R. Pedrosa, H. Pentikäinen, J. Pereira, B. Pichon, A. M. Piersimoni, F. X. Pineau, E. Plachy, G. Plum, E. Poujoulet, A. Prša, L. Pulone, S. Ragaini, S. Rago, N. Rambaux, M. Ramos-Lerate, P. Ranalli, G. Rauw, A. Read, S. Regibo, F. Renk, C. Reylé, R. A. Ribeiro, L. Rimoldini, V. Ripepi, A. Riva, G. Rixon, M. Roelens, M. Romero-Gómez, N. Rowell, F. Royer, A. Rudolph, L. Ruiz-Dern, G. Sadowski, T. Sagristà Sellés, J. Sahlmann, J. Salgado, E. Salguero, M. Sarasso, H. Savietto, A. Schnorhk, M. Schultheis, E. Sciacca, M. Segol, J. C. Segovia, D. Segransan, E. Serpell, I. C. Shih, R. Smareglia, R. L. Smart, C. Smith, E. Solano, F. Solitro, R. Sordo, S. Soria Nieto, J. Souchay, A. Spagna, F. Spoto, U. Stampa, I. A. Steele, H. Steidelmüller, C. A. Stephenson, H. Stoev, F. F. Suess, M. Süveges, J. Surdej, L. Szabados, E. Szegedi-Elek, D. Tapiador, F. Taris, G. Tauran, M. B. Taylor, R. Teixeira, D. Terrett, B. Tingley, S. C. Trager, C. Turon, A. Ulla, E. Utrilla, G. Valentini, A. van Elteren, E. Van Hemelryck, M. van Leeuwen, M. Varadi, A. Vecchiato, J. Veljanoski, T. Via, D. Vicente, S. Vogt, H. Voss, V. Votruba, S. Voutsinas, G. Walmsley, M. Weiler, K. Weingrill, D. Werner, T. Wevers, G. Whitehead, Ł. Wyrzykowski, A. Yoldas, M. Žerjal, S. Zucker, C. Zurbach, T. Zwitter, A. Alecu, M. Allen, C. Allende Prieto, A. Amorim, G. Anglada-Escudé, V. Arsenijevic, S. Azaz, P. Balm, M. Beck, H. H. Bernstein, L. Bigot, A. Bijaoui, C. Blasco, M. Bonfigli, G. Bono, S. Boudreault, A. Bressan, S. Brown, P. M. Brunet, P. Bunclark, R. Buonanno, A. G. Butkevich, C. Carret, C. Carrion, L. Chemin, F. Chéreau, L. Corcione, E. Darmigny, K. S. de Boer, P. de Teodoro, P. T. de Zeeuw, C. Delle Luche, C. D. Domingues, P. Dubath, F. Fodor, B. Frézouls, A. Fries, D. Fustes, D. Fyfe, E. Gallardo, J. Gallegos, D. Gardiol, M. Gebran, A. Gomboc, A. Gómez, E. Grux, A. Gueguen, A. Heyrovsky, J. Hoar, G. Iannicola, Y. Isasi Parache, A. M. Janotto, E. Joliet, A. Jonckheere, R. Keil, D. W. Kim, P. Klagyivik, J. Klar, J. Knude, O. Kochukhov, I. Kolka, J. Kos, A. Kutka, V. Lainey, D. LeBouquin, C. Liu, D. Loreggia, V. V. Makarov, M. G. Marseille, C. Martayan, O. Martinez-Rubi, B. Massart, F. Meynadier, S. Mignot, U. Munari, A. T. Nguyen, T. Nordlander, P. Ocvirk, K. S. O'Flaherty, A. Olias Sanz, P. Ortiz, J. Osorio, D. Oszkiewicz, A. Ouzounis, M. Palmer, P. Park, E. Pasquato, C. Peltzer, J. Peralta, F. Péturaud, T. Pieniluoma, E. Pigozzi, J. Poels, G. Prat, T. Prod'homme, F. Raison, J. M. Rebordao, D. Risquez, B. Rocca-Volmerange, S. Rosen, M. I. Ruiz-Fuertes, F. Russo, S. Sembay, I. Serraller Vizcaino, A. Short, A. Siebert, H. Silva, D. Sinachopoulos, E. Slezak, M. Soffel, D. Sosnowska, V. Straižys, M. ter Linden, D. Terrell, S. Theil, C. Tiede, L. Troisi, P. Tsalmantza, D. Tur, M. Vaccari, F. Vachier, P. Valles, W. Van Hamme, L. Veltz, J. Virtanen, J. M. Wallut, R. Wichmann, M. I. Wilkinson, H. Ziaeepour, and S. Zschocke. The Gaia mission. *A&A*, 595:A1, Nov. 2016. doi: 10.1051/0004-6361/201629272.

N. Garavito-Camargo, G. Besla, C. F. P. Laporte, K. V. Johnston, F. A. Gómez, and L. L. Watkins. Hunting for the Dark Matter Wake Induced by the Large Magellanic Cloud. *ApJ*,

884(1):51, Oct. 2019. doi: 10.3847/1538-4357/ab32eb.

N. Garavito-Camargo, G. Besla, C. F. P. Laporte, A. M. Price-Whelan, E. C. Cunningham, K. V. Johnston, M. Weinberg, and F. A. Gómez. Quantifying the Impact of the Large Magellanic Cloud on the Structure of the Milky Way's Dark Matter Halo Using Basis Function Expansions. *ApJ*, 919(2):109, Oct. 2021. doi: 10.3847/1538-4357/ac0b44.

J. P. Gardner, J. C. Mather, M. Clampin, R. Doyon, M. A. Greenhouse, H. B. Hammel, J. B. Hutchings, P. Jakobsen, S. J. Lilly, K. S. Long, J. I. Lunine, M. J. McCaughrean, M. Mountain, J. Nella, G. H. Rieke, M. J. Rieke, H.-W. Rix, E. P. Smith, G. Sonneborn, M. Stiavelli, H. S. Stockman, R. A. Windhorst, and G. S. Wright. The James Webb Space Telescope. *Space Sci. Rev.*, 123(4):485–606, Apr. 2006. doi: 10.1007/s11214-006-8315-7.

S. Garrison-Kimmel, P. F. Hopkins, A. Wetzel, J. S. Bullock, M. Boylan-Kolchin, D. Kereš, C.-A. Faucher-Giguère, K. El-Badry, A. Lamberts, E. Quataert, and R. Sanderson. The Local Group on FIRE: dwarf galaxy populations across a suite of hydrodynamic simulations. *MNRAS*, 487(1):1380–1399, July 2019a. doi: 10.1093/mnras/stz1317.

S. Garrison-Kimmel, A. Wetzel, P. F. Hopkins, R. Sanderson, K. El-Badry, A. Graus, T. K. Chan, R. Feldmann, M. Boylan-Kolchin, C. C. Hayward, J. S. Bullock, A. Fitts, J. Samuel, C. Wheeler, D. Kereš, and C.-A. Faucher-Giguère. Star formation histories of dwarf galaxies in the FIRE simulations: dependence on mass and Local Group environment. *MNRAS*, 489(4):4574–4588, Nov. 2019b. doi: 10.1093/mnras/stz2507.

J. J. Geehan, M. A. Fardal, A. Babul, and P. Guhathakurta. Investigating the Andromeda stream - I. Simple analytic bulge-disc-halo model for M31. *MNRAS*, 366(3):996–1011, Mar. 2006. doi: 10.1111/j.1365-2966.2005.09863.x.

M. Geha, M. R. Blanton, R. Yan, and J. L. Tinker. A Stellar Mass Threshold for Quenching of Field Galaxies. *ApJ*, 757(1):85, Sept. 2012. doi: 10.1088/0004-637X/757/1/85.

M. Geha, T. M. Brown, J. Tumlinson, J. S. Kalirai, J. D. Simon, E. N. Kirby, D. A. VandenBerg, R. R. Muñoz, R. J. Avila, P. Guhathakurta, and H. C. Ferguson. The Stellar Initial Mass Function of Ultra-faint Dwarf Galaxies: Evidence for IMF Variations with Galactic Environment. *ApJ*, 771:29, July 2013. doi: 10.1088/0004-637x/771/1/29.

M. Geha, R. H. Wechsler, Y.-Y. Mao, E. J. Tollerud, B. Weiner, R. Bernstein, B. Hoyle, S. Marchi, P. J. Marshall, R. Muñoz, and Y. Lu. The SAGA Survey. I. Satellite Galaxy Populations around Eight Milky Way Analogs. *ApJ*, 847(1):4, Sept. 2017. doi: 10.3847/1538-4357/aa8626.

A. Gelman and D. B. Rubin. Inference from Iterative Simulation Using Multiple Sequences. *Statistical Science*, 7:457–472, Jan. 1992. doi: 10.1214/ss/1177011136.

S. Genel, M. Vogelsberger, V. Springel, D. Sijacki, D. Nelson, G. Snyder, V. Rodriguez-Gomez, P. Torrey, and L. Hernquist. Introducing the Illustris project: the evolution of galaxy populations across cosmic time. *MNRAS*, 445:175–200, Nov. 2014. doi: 10.1093/mnras/stu1654.

K. M. Gilbert, E. N. Kirby, I. Escala, J. Wojno, J. S. Kalirai, and P. Guhathakurta. Elemental Abundances in M31: First Alpha and Iron Abundance Measurements in M31's Giant Stellar Stream. *ApJ*, 883(2):128, Oct. 2019. doi: 10.3847/1538-4357/ab3807.

E. Glikman, B. Simmons, M. Mailly, K. Schawinski, C. M. Urry, and M. Lacy. Major Mergers Host the Most-luminous Red Quasars at z ~2: A Hubble Space Telescope WFC3/IR Study. *ApJ*, 806(2):218, June 2015. doi: 10.1088/0004-637x/806/2/218.

F. A. Gómez, G. Besla, D. D. Carpintero, Á. Villalobos, B. W. O'Shea, and E. F. Bell. And Yet it Moves: The Dangers of Artificially Fixing the Milky Way Center of Mass in the Presence of a Massive Large Magellanic Cloud. *ApJ*, 802(2):128, Apr. 2015. doi: 10.1088/0004-637x/802/2/128.

R. E. González, A. V. Kravtsov, and N. Y. Gnedin. On the Mass of the Local Group. *ApJ*, 793(2):91, Oct. 2014. doi: 10.1088/0004-637x/793/2/91.

Gravity Collaboration, R. Abuter, A. Amorim, N. Anugu, M. Bauböck, M. Benisty, J. P. Berger, N. Blind, H. Bonnet, W. Brandner, A. Buron, C. Collin, F. Chapron, Y. Clénet, V. Coudé Du Foresto, P. T. de Zeeuw, C. Deen, F. Delplancke-Ströbele, R. Dembet, J. Dexter, G. Duvert, A. Eckart, F. Eisenhauer, G. Finger, N. M. Förster Schreiber, P. Fédou, P. Garcia, R. Garcia Lopez, F. Gao, E. Gendron, R. Genzel, S. Gillessen, P. Gordo, M. Habibi, X. Haubois, M. Haug, F. Haußmann, T. Henning, S. Hippler, M. Horrobin, Z. Hubert, N. Hubin, A. Jimenez Rosales, L. Jochum, K. Jocou, A. Kaufer, S. Kellner, S. Kendrew, P. Kervella, Y. Kok, M. Kulas, S. Lacour, V. Lapeyrère, B. Lazareff, J. B. Le Bouquin, P. Léna, M. Lippa, R. Lenzen, A. Mérand, E. Müler, U. Neumann, T. Ott, L. Palanca, T. Paumard, L. Pasquini, K. Perraut, G. Perrin, O. Pfuhl, P. M. Plewa, S. Rabien, A. Ramírez, J. Ramos, C. Rau, G. Rodríguez-Coira, R. R. Rohloff, G. Rousset, J. Sanchez-Bermudez, S. Scheithauer, M. Schöller, N. Schuler, J. Spyromilio, O. Straub, C. Straubmeier, E. Sturm, L. J. Tacconi, K. R. W. Tristram, F. Vincent, S. von Fellenberg, I. Wank, I. Waisberg, F. Widmann, E. Wieprecht, M. Wiest, E. Wiezorrek, J. Woillez, S. Yazici, D. Ziegler, and G. Zins. Detection of the gravitational redshift in the orbit of the star S2 near the Galactic centre massive black hole. *A&A*, 615:L15, July 2018. doi: 10.1051/0004-6361/201833718.

Q. Guo and S. D. M. White. Galaxy growth in the concordance ΛCDM cosmology. *MNRAS*, 384(1):2–10, Feb. 2008. doi: 10.1111/j.1365-2966.2007.12619.x.

A. Guzmán-Ortega, V. Rodriguez-Gomez, G. F. Snyder, K. Chamberlain, and L. Hernquist. Morphological signatures of mergers in the TNG50 simulation and the Kilo-Degree Survey: the merger fraction from dwarfs to Milky Way-like galaxies. *MNRAS*, 519(4):4920–4937, Mar. 2023. doi: 10.1093/mnras/stac3334.

M. H. Hani, H. Gosain, S. L. Ellison, D. R. Patton, and P. Torrey. Interacting galaxies in the IllustrisTNG simulations - II: star formation in the post-merger stage. *MNRAS*, 493 (3):3716–3731, Apr. 2020. doi: 10.1093/mnras/staa459.

O. V. Hartl and L. E. Strigari. Local Group timing argument and virial theorem mass estimators from cosmological simulations. *MNRAS*, 511(4):6193–6204, Apr. 2022. doi: 10.1093/mnras/stac413.

G. Hinshaw, D. Larson, E. Komatsu, D. N. Spergel, C. L. Bennett, J. Dunkley, M. R. Nolta, M. Halpern, R. S. Hill, N. Odegard, L. Page, K. M. Smith, J. L. Weiland, B. Gold, N. Jarosik, A. Kogut, M. Limon, S. S. Meyer, G. S. Tucker, E. Wollack, and E. L. Wright. Nine-year Wilkinson Microwave Anisotropy Probe (WMAP) Observations: Cosmological Parameter Results. *ApJS*, 208:19, Oct. 2013. doi: 10.1088/0067-0049/208/2/19.

M. D. Homan and A. Gelman. The no-u-turn sampler: Adaptively setting path lengths in hamiltonian monte carlo. *J. Mach. Learn. Res.*, 15(1):1593–1623, Jan. 2014. ISSN 1532-4435.

P. F. Hopkins, L. Hernquist, T. J. Cox, and D. Kereš. A Cosmological Framework for the Co-Evolution of Quasars, Supermassive Black Holes, and Elliptical Galaxies. I. Galaxy Mergers and Quasar Activity. *ApJS*, 175(2):356–389, Apr. 2008. doi: 10.1086/524362.

P. F. Hopkins, K. Bundy, D. Croton, L. Hernquist, D. Keres, S. Khochfar, K. Stewart, A. Wetzel, and J. D. Younger. Mergers and Bulge Formation in ΛCDM: Which Mergers Matter? *ApJ*, 715(1):202–229, May 2010a. doi: 10.1088/0004-637X/715/1/202.

P. F. Hopkins, D. Croton, K. Bundy, S. Khochfar, F. van den Bosch, R. S. Somerville, A. Wetzel, D. Keres, L. Hernquist, K. Stewart, J. D. Younger, S. Genel, and C.-P. Ma. Mergers in ΛCDM: Uncertainties in Theoretical Predictions and Interpretations of the Merger Rate. *ApJ*, 724(2):915–945, Dec. 2010b. doi: 10.1088/0004-637x/724/2/915.

P. F. Hopkins, T. J. Cox, L. Hernquist, D. Narayanan, C. C. Hayward, and N. Murray. Star formation in galaxy mergers with realistic models of stellar feedback and the interstellar medium. *MNRAS*, 430(3):1901–1927, Apr. 2013. doi: 10.1093/mnras/stt017.

R. Ibata, M. Irwin, G. Lewis, A. M. N. Ferguson, and N. Tanvir. A giant stream of metal-rich stars in the halo of the galaxy M31. *Nature*, 412(6842):49–52, July 2001.

Ž. Ivezić, S. M. Kahn, J. A. Tyson, B. Abel, E. Acosta, R. Allsman, D. Alonso, Y. AlSayyad, S. F. Anderson, J. Andrew, J. R. P. Angel, G. Z. Angeli, R. Ansari, P. Antilogus, C. Araujo, R. Armstrong, K. T. Arndt, P. Astier, É. Aubourg, N. Auza, T. S. Axelrod, D. J. Bard, J. D. Barr, A. Barrau, J. G. Bartlett, A. E. Bauer, B. J. Bauman, S. Baumont, E. Bechtol, K. Bechtol, A. C. Becker, J. Becla, C. Beldica, S. Bellavia, F. B. Bianco, R. Biswas, G. Blanc, J. Blazek, R. D. Blandford, J. S. Bloom, J. Bogart, T. W. Bond, M. T. Booth, A. W. Borgland, K. Borne, J. F. Bosch, D. Boutigny, C. A. Brackett, A. Bradshaw, W. N. Brandt, M. E. Brown, J. S. Bullock, P. Burchat, D. L. Burke, G. Cagnoli, D. Calabrese, S. Callahan, A. L. Callen, J. L. Carlin, E. L. Carlson, S. Chandrasekharan, G. Charles-Emerson, S. Chesley, E. C. Cheu, H.-F. Chiang, J. Chiang, C. Chirino, D. Chow, D. R. Ciardi, C. F. Claver, J. Cohen-Tanugi, J. J. Cockrum, R. Coles, A. J. Connolly, K. H. Cook, A. Cooray, K. R. Covey, C. Cribbs, W. Cui, R. Cutri, P. N. Daly, S. F. Daniel, F. Daruich, G. Daubard, G. Daues, W. Dawson, F. Delgado, A. Dellapenna, R. de Peyster,

M. de Val-Borro, S. W. Digel, P. Doherty, R. Dubois, G. P. Dubois-Felsmann, J. Durech, F. Economou, T. Eifler, M. Eracleous, B. L. Emmons, A. Fausti Neto, H. Ferguson, E. Figueroa, M. Fisher-Levine, W. Focke, M. D. Foss, J. Frank, M. D. Freemon, E. Gangler, E. Gawiser, J. C. Geary, P. Gee, M. Geha, C. J. B. Gessner, R. R. Gibson, D. K. Gilmore, T. Glanzman, W. Glick, T. Goldina, D. A. Goldstein, I. Goodenow, M. L. Graham, W. J. Gressler, P. Gris, L. P. Guy, A. Guyonnet, G. Haller, R. Harris, P. A. Hascall, J. Haupt, F. Hernandez, S. Herrmann, E. Hileman, J. Hoblitt, J. A. Hodgson, C. Hogan, J. D. Howard, D. Huang, M. E. Huffer, P. Ingraham, W. R. Innes, S. H. Jacoby, B. Jain, F. Jammes, M. J. Jee, T. Jenness, G. Jernigan, D. Jevremović, K. Johns, A. S. Johnson, M. W. G. Johnson, R. L. Jones, C. Juramy-Gilles, M. Jurić, J. S. Kalirai, N. J. Kallivayalil, B. Kalmbach, J. P. Kantor, P. Karst, M. M. Kasliwal, H. Kelly, R. Kessler, V. Kinnison, D. Kirkby, L. Knox, I. V. Kotov, V. L. Krabbendam, K. S. Krughoff, P. Kubánek, J. Kuczewski, S. Kulkarni, J. Ku, N. R. Kurita, C. S. Lage, R. Lambert, T. Lange, J. B. Langton, L. Le Guillou, D. Levine, M. Liang, K.-T. Lim, C. J. Lintott, K. E. Long, M. Lopez, P. J. Lotz, R. H. Lupton, N. B. Lust, L. A. MacArthur, A. Mahabal, R. Mandelbaum, T. W. Markiewicz, D. S. Marsh, P. J. Marshall, S. Marshall, M. May, R. McKercher, M. McQueen, J. Meyers, M. Migliore, M. Miller, D. J. Mills, C. Miraval, J. Moeyens, F. E. Moolekamp, D. G. Monet, M. Moniez, S. Monkewitz, C. Montgomery, C. B. Morrison, F. Mueller, G. P. Muller, F. Muñoz Arancibia, D. R. Neill, S. P. Newbry, J.-Y. Nief, A. Nomerotski, M. Nordby, P. O'Connor, J. Oliver, S. S. Olivier, K. Olsen, W. O'Mullane, S. Ortiz, S. Osier, R. E. Owen, R. Pain, P. E. Palecek, J. K. Parejko, J. B. Parsons, N. M. Pease, J. M. Peterson, J. R. Peterson, D. L. Petravick, M. E. Libby Petrick, C. E. Petry, F. Pierfederici, S. Pietrowicz, R. Pike, P. A. Pinto, R. Plante, S. Plate, J. P. Plutchak, P. A. Price, M. Prouza, V. Radeka, J. Rajagopal, A. P. Rasmussen, N. Regnault, K. A. Reil, D. J. Reiss, M. A. Reuter, S. T. Ridgway, V. J. Riot, S. Ritz, S. Robinson, W. Roby, A. Roodman, W. Rosing, C. Roucelle, M. R. Rumore, S. Russo, A. Saha, B. Sassolas, T. L. Schalk, P. Schellart, R. H. Schindler, S. Schmidt, D. P. Schneider, M. D. Schneider, W. Schoening, G. Schumacher, M. E. Schwamb, J. Sebag, B. Selvy, G. H. Sembroski, L. G. Seppala, A. Serio, E. Serrano, R. A. Shaw, I. Shipsey, J. Sick, N. Silvestri, C. T. Slater, J. A. Smith, R. C. Smith, S. Sobhani, C. Soldahl, L. Storrie-Lombardi, E. Stover, M. A. Strauss, R. A. Street, C. W. Stubbs, I. S. Sullivan, D. Sweeney, J. D. Swinbank, A. Szalay, P. Takacs, S. A. Tether, J. J. Thaler, J. G. Thayer, S. Thomas, A. J. Thornton, V. Thukral, J. Tice, D. E. Trilling, M. Turri, R. Van Berg, D. Vanden Berk, K. Vetter, F. Virieux, T. Vucina, W. Wahl, L. Walkowicz, B. Walsh, C. W. Walter, D. L. Wang, S.-Y. Wang, M. Warner, O. Wiecha, B. Willman, S. E. Winters, D. Wittman, S. C. Wolff, W. M. Wood-Vasey, X. Wu, B. Xin, P. Yoachim, and H. Zhan. LSST: From Science Drivers to Reference Design and Anticipated Data Products. *ApJ*, 873(2):111, Mar. 2019. doi: 10.3847/1538-4357/ab042c.

R. A. Jackson, G. Martin, S. Kaviraj, C. Laigle, J. E. G. Devriendt, Y. Dubois, and C. Pichon. Massive spheroids can form in single minor mergers. *MNRAS*, 489(4):4679–4689, Nov. 2019. doi: 10.1093/mnras/stz2440.

R. A. Jackson, S. Kaviraj, G. Martin, J. E. G. Devriendt, E. A. Noakes-Kettel, J. Silk, P. Ogle,

and Y. Dubois. Extremely massive disc galaxies in the nearby Universe form through gas-rich minor mergers. *MNRAS*, 511(1):607–615, Mar. 2022. doi: 10.1093/mnras/stac058.

N. Jarosik, C. L. Bennett, J. Dunkley, B. Gold, M. R. Greason, M. Halpern, R. S. Hill, G. Hinshaw, A. Kogut, E. Komatsu, D. Larson, M. Limon, S. S. Meyer, M. R. Nolta, N. Odegard, L. Page, K. M. Smith, D. N. Spergel, G. S. Tucker, J. L. Weiland, E. Wollack, and E. L. Wright. Seven-year Wilkinson Microwave Anisotropy Probe (WMAP) Observations: Sky Maps, Systematic Errors, and Basic Results. *ApJS*, 192(2):14, Feb. 2011. doi: 10.1088/0067-0049/192/2/14.

C. Y. Jiang, Y. P. Jing, A. Faltenbacher, W. P. Lin, and C. Li. A Fitting Formula for the Merger Timescale of Galaxies in Hierarchical Clustering. *ApJ*, 675(2):1095–1105, Mar. 2008. doi: 10.1086/526412.

E. Kado-Fong, A. Robinson, K. Nyland, J. E. Greene, K. A. Suess, S. Stierwalt, and R. Beaton. Dwarf–Dwarf Interactions Can Both Trigger and Quench Star Formation. *ApJ*, 963(1):37, Mar. 2024. doi: 10.3847/1538-4357/ad18cb.

F. D. Kahn and L. Woltjer. Intergalactic Matter and the Galaxy. *ApJ*, 130:705, Nov. 1959. doi: 10.1086/146762.

N. Kallivayalil, R. P. van der Marel, C. Alcock, T. Axelrod, K. H. Cook, A. J. Drake, and M. Geha. The Proper Motion of the Large Magellanic Cloud Using HST. *ApJ*, 638:772–785, Feb. 2006a. doi: 10.1086/498972.

N. Kallivayalil, R. P. van der Marel, and C. Alcock. Is the SMC Bound to the LMC? The Hubble Space Telescope Proper Motion of the SMC. *ApJ*, 652:1213–1229, Dec. 2006b. doi: 10.1086/508014.

N. Kallivayalil, R. P. van der Marel, G. Besla, J. Anderson, and C. Alcock. Third-epoch Magellanic Cloud Proper Motions. I. Hubble Space Telescope/WFC3 Data and Orbit Implications. *ApJ*, 764(2):161, Feb. 2013. doi: 10.1088/0004-637x/764/2/161.

S. E. Koposov, D. Erkal, T. S. Li, G. S. Da Costa, L. R. Cullinane, A. P. Ji, K. Kuehn, G. F. Lewis, A. B. Pace, N. Shipp, D. B. Zucker, J. Bland-Hawthorn, S. Lilleengen, S. L. Martell, and S5 Collaboration. S [5]: Probing the Milky Way and Magellanic Clouds potentials with the 6D map of the Orphan-Chenab stream. *MNRAS*, 521(4):4936–4962, June 2023. doi: 10.1093/mnras/stad551.

M. T. Kristensen, K. A. Pimbblet, B. K. Gibson, S. J. Penny, and S. Koudmani. Merger Histories and Environments of Dwarf AGN in IllustrisTNG. *ApJ*, 922(2):127, Dec. 2021. doi: 10.3847/1538-4357/ac236d.

T. L. Kroeker and R. G. Carlberg. The Accuracy of Galaxy Masses from the Timing Argument. *ApJ*, 376:1, July 1991. doi: 10.1086/170249.

R. Kumar, C. Carroll, A. Hartikainen, and O. Martin. Arviz a unified library for exploratory analysis of bayesian models in python. *Journal of Open Source Software*, 4(33):1143, 2019. doi: 10.21105/joss.01143. URL https://doi.org/10.21105/joss.01143.

C. F. P. Laporte, F. A. Gómez, G. Besla, K. V. Johnston, and N. Garavito-Camargo. Response of the Milky Way's disc to the Large Magellanic Cloud in a first infall scenario. *MNRAS*, 473(1):1218–1230, Jan. 2018a. doi: 10.1093/mnras/stx2146.

C. F. P. Laporte, K. V. Johnston, F. A. Gómez, N. Garavito-Camargo, and G. Besla. The influence of Sagittarius and the Large Magellanic Cloud on the stellar disc of the Milky Way Galaxy. *MNRAS*, 481(1):286–306, Nov. 2018b. doi: 10.1093/mnras/sty1574.

P. Lemos, N. Jeffrey, L. Whiteway, O. Lahav, N. Libeskind, and Y. Hoffman. Sum of the masses of the milky way and m31: A likelihood-free inference approach. *Phys. Rev. D*, 103: 023009, Jan. 2021. doi: 10.1103/PhysRevD.103.023009. URL https://link.aps.org/doi/10.1103/PhysRevD.103.023009.

S. Li, A. G. Riess, M. P. Busch, S. Casertano, L. M. Macri, and W. Yuan. A Sub-2% Distance to M31 from Photometrically Homogeneous Near-infrared Cepheid Period-Luminosity Relations Measured with the Hubble Space Telescope. *ApJ*, 920(2):84, Oct. 2021. doi: 10.3847/1538-4357/ac1597.

Y.-S. Li and S. D. M. White. Masses for the Local Group and the Milky Way. *MNRAS*, 384 (4):1459–1468, Mar. 2008. doi: 10.1111/j.1365-2966.2007.12748.x.

T. C. Licquia and J. A. Newman. Improved Estimates of the Milky Way's Stellar Mass and Star Formation Rate from Hierarchical Bayesian Meta-Analysis. *ApJ*, 806(1):96, June 2015. doi: 10.1088/0004-637X/806/1/96.

S. Lilleengen, M. S. Petersen, D. Erkal, J. Peñarrubia, S. E. Koposov, T. S. Li, L. R. Cullinane, A. P. Ji, K. Kuehn, G. F. Lewis, D. Mackey, A. B. Pace, N. Shipp, D. B. Zucker, J. Bland-Hawthorn, T. Hilmi, and S5 Collaboration. The effect of the deforming dark matter haloes of the Milky Way and the Large Magellanic Cloud on the Orphan-Chenab stream. *MNRAS*, 518(1):774–790, Jan. 2023. doi: 10.1093/mnras/stac3108.

L. Lin, D. C. Koo, C. N. A. Willmer, D. R. Patton, C. J. Conselice, R. Yan, A. L. Coil, M. C. Cooper, M. Davis, S. M. Faber, B. F. Gerke, P. Guhathakurta, and J. A. Newman. The DEEP2 Galaxy Redshift Survey: Evolution of Close Galaxy Pairs and Major-Merger Rates up to z ~1.2. *ApJ*, 617(1):L9–l12, Dec. 2004. doi: 10.1086/427183.

L. Lin, D. R. Patton, D. C. Koo, K. Casteels, C. J. Conselice, S. M. Faber, J. Lotz, C. N. A. Willmer, B. C. Hsieh, T. Chiueh, J. A. Newman, G. S. Novak, B. J. Weiner, and M. C. Cooper. The Redshift Evolution of Wet, Dry, and Mixed Galaxy Mergers from Close Galaxy Pairs in the DEEP2 Galaxy Redshift Survey. *ApJ*, 681(1):232–243, July 2008. doi: 10.1086/587928.

L. Liu, B. F. Gerke, R. H. Wechsler, P. S. Behroozi, and M. T. Busha. How Common are the Magellanic Clouds? *ApJ*, 733:62, May 2011. doi: 10.1088/0004-637x/733/1/62.

J. M. Lotz, M. Davis, S. M. Faber, P. Guhathakurta, S. Gwyn, J. Huang, D. C. Koo, E. Le Floc'h, L. Lin, J. Newman, K. Noeske, C. Papovich, C. N. A. Willmer, A. Coil, C. J. Conselice, M. Cooper, A. M. Hopkins, A. Metevier, J. Primack, G. Rieke, and B. J. Weiner.

The Evolution of Galaxy Mergers and Morphology at z ¡ 1.2 in the Extended Groth Strip. *ApJ*, 672(1):177–197, Jan. 2008. doi: 10.1086/523659.

J. M. Lotz, P. Jonsson, T. J. Cox, D. Croton, J. R. Primack, R. S. Somerville, and K. Stewart. The Major and Minor Galaxy Merger Rates at z ¡ 1.5. *ApJ*, 742(2):103, Dec. 2011. doi: 10.1088/0004-637x/742/2/103.

N. Luber, S. Pearson, M. E. Putman, G. Besla, S. Stierwalt, and J. P. Meyers. Investigating the Baryon Cycle in Interacting Dwarfs with the Very Large Array and Pan-STARRS. *AJ*, 163(2):49, Feb. 2022. doi: 10.3847/1538-3881/ac3750.

D. Lynden-Bell. The dynamical age of the local group of galaxies. *The Observatory*, 101: 111–114, Aug. 1981.

A. W. S. Man, A. W. Zirm, and S. Toft. Resolving the Discrepancy of Galaxy Merger Fraction Measurements at z ∼ 0-3. *ApJ*, 830(2):89, Oct. 2016. doi: 10.3847/0004-637x/830/2/89.

Y.-Y. Mao, M. Geha, R. H. Wechsler, B. Weiner, E. J. Tollerud, E. O. Nadler, and N. Kallivayalil. The SAGA Survey. II. Building a Statistical Sample of Satellite Systems around Milky Way-like Galaxies. *ApJ*, 907(2):85, Feb. 2021. doi: 10.3847/1538-4357/abce58.

F. Marinacci, R. J. J. Grand, R. Pakmor, V. Springel, F. A. Gómez, C. S. Frenk, and S. D. M. White. Properties of H I discs in the Auriga cosmological simulations. *MNRAS*, 466(4): 3859–3875, Apr. 2017. doi: 10.1093/mnras/stw3366.

F. Marinacci, M. Vogelsberger, R. Pakmor, P. Torrey, V. Springel, L. Hernquist, D. Nelson, R. Weinberger, A. Pillepich, J. Naiman, and S. Genel. First results from the IllustrisTNG simulations: radio haloes and magnetic fields. *MNRAS*, 480(4):5113–5139, Nov. 2018. doi: 10.1093/mnras/sty2206.

G. Martin, S. Kaviraj, J. E. G. Devriendt, Y. Dubois, C. Laigle, and C. Pichon. The limited role of galaxy mergers in driving stellar mass growth over cosmic time. *MNRAS*, 472(1): L50–l54, Nov. 2017. doi: 10.1093/mnrasl/slx136.

G. Martin, S. Kaviraj, J. E. G. Devriendt, Y. Dubois, and C. Pichon. The role of mergers in driving morphological transformation over cosmic time. *MNRAS*, 480(2):2266–2283, Oct. 2018. doi: 10.1093/mnras/sty1936.

G. Martin, R. A. Jackson, S. Kaviraj, H. Choi, J. E. G. Devriendt, Y. Dubois, T. Kimm, K. Kraljic, S. Peirani, C. Pichon, M. Volonteri, and S. K. Yi. The role of mergers and interactions in driving the evolution of dwarf galaxies over cosmic time. *MNRAS*, 500(4): 4937–4957, Jan. 2021. doi: 10.1093/mnras/staa3443.

G. Martin, A. E. Bazkiaei, M. Spavone, E. Iodice, J. C. Mihos, M. Montes, J. A. Benavides, S. Brough, J. L. Carlin, C. A. Collins, P. A. Duc, F. A. Gómez, G. Galaz, H. M. Hernández-Toledo, R. A. Jackson, S. Kaviraj, J. H. Knapen, C. Martínez-Lombilla, S. McGee, D. O'Ryan, D. J. Prole, R. M. Rich, J. Román, E. A. Shah, T. K. Starkenburg, A. E. Watkins, D. Zaritsky, C. Pichon, L. Armus, M. Bianconi, F. Buitrago, I. Busá, F. Davis, R. Demarco,

A. Desmons, P. García, A. W. Graham, B. Holwerda, D. S. H. Hon, A. Khalid, J. Klehammer, D. Y. Klutse, I. Lazar, P. Nair, E. A. Noakes-Kettel, M. Rutkowski, K. Saha, N. Sahu, E. Sola, J. A. Vázquez-Mata, A. Vera-Casanova, and I. Yoon. Preparing for low surface brightness science with the Vera C. Rubin Observatory: Characterization of tidal features from mock images. *MNRAS*, 513(1):1459–1487, June 2022. doi: 10.1093/mnras/stac1003.

M. McLeod, N. Libeskind, O. Lahav, and Y. Hoffman. Estimating the mass of the Local Group using machine learning applied to numerical simulations. *JCAP*, 2017(12):034, Dec. 2017. doi: 10.1088/1475-7516/2017/12/034.

P. J. McMillan. The solar neighbourhood in angle coordinates: the Hyades moving group. *MNRAS*, 418(3):1565–1574, Dec. 2011. doi: 10.1111/j.1365-2966.2011.19520.x.

J. C. Mihos and L. Hernquist. Gasdynamics and Starbursts in Major Mergers. *ApJ*, 464:641, June 1996. doi: 10.1086/177353.

S. Milošević, M. Mićić, and G. F. Lewis. Metallicity distribution of the progenitor of the Giant Stellar Stream in the Andromeda Galaxy. *MNRAS*, Jan. 2022. doi: 10.1093/mnras/stac249.

B. P. Moster, T. Naab, and S. D. M. White. Galactic star formation and accretion histories from matching galaxies to dark matter haloes. *MNRAS*, 428:3121–3138, Feb. 2013. doi: 10.1093/mnras/sts261.

F. Munshi, A. M. Brooks, E. Applebaum, C. R. Christensen, T. Quinn, and S. Sligh. Quantifying Scatter in Galaxy Formation at the Lowest Masses. *ApJ*, 923(1):35, Dec. 2021. doi: 10.3847/1538-4357/ac0db6.

J. P. Naiman, A. Pillepich, V. Springel, E. Ramirez-Ruiz, P. Torrey, M. Vogelsberger, R. Pakmor, D. Nelson, F. Marinacci, L. Hernquist, R. Weinberger, and S. Genel. First results from the IllustrisTNG simulations: a tale of two elements - chemical evolution of magnesium and europium. *MNRAS*, 477(1):1206–1224, June 2018. doi: 10.1093/mnras/sty618.

D. Nelson, A. Pillepich, S. Genel, M. Vogelsberger, V. Springel, P. Torrey, V. Rodriguez-Gomez, D. Sijacki, G. F. Snyder, B. Griffen, F. Marinacci, L. Blecha, L. Sales, D. Xu, and L. Hernquist. The illustris simulation: Public data release. *Astronomy and Computing*, 13: 12–37, Nov. 2015. doi: 10.1016/j.ascom.2015.09.003.

D. Nelson, A. Pillepich, V. Springel, R. Weinberger, L. Hernquist, R. Pakmor, S. Genel, P. Torrey, M. Vogelsberger, G. Kauffmann, F. Marinacci, and J. Naiman. First results from the IllustrisTNG simulations: the galaxy colour bimodality. *MNRAS*, 475(1):624–647, Mar. 2018. doi: 10.1093/mnras/stx3040.

D. Nelson, V. Springel, A. Pillepich, V. Rodriguez-Gomez, P. Torrey, S. Genel, M. Vogelsberger, R. Pakmor, F. Marinacci, R. Weinberger, L. Kelley, M. Lovell, B. Diemer, and L. Hernquist. The IllustrisTNG simulations: public data release. *Computational Astrophysics and Cosmology*, 6(1):2, May 2019. doi: 10.1186/s40668-019-0028-x.

C. Partridge, O. Lahav, and Y. Hoffman. Weighing the local group in the presence of dark energy. *MNRAS*, 436:L45–l48, Nov. 2013. doi: 10.1093/mnrasl/slt109.

E. Patel and K. S. Mandel. Evidence for a Massive Andromeda Galaxy Using Satellite Galaxy Proper Motions. *ApJ*, 948(2):104, May 2023. doi: 10.3847/1538-4357/acc029.

E. Patel, G. Besla, and S. T. Sohn. Orbits of massive satellite galaxies - I. A close look at the Large Magellanic Cloud and a new orbital history for M33. *MNRAS*, 464(4):3825–3849, Feb. 2017a. doi: 10.1093/mnras/stw2616.

E. Patel, G. Besla, and K. Mandel. Orbits of massive satellite galaxies - II. Bayesian estimates of the Milky Way and Andromeda masses using high-precision astrometry and cosmological simulations. *MNRAS*, 468(3):3428–3449, July 2017b. doi: 10.1093/mnras/stx698.

E. Patel, G. Besla, K. Mandel, and S. T. Sohn. Estimating the Mass of the Milky Way Using the Ensemble of Classical Satellite Galaxies. *ApJ*, 857(2):78, Apr. 2018. doi: 10.3847/1538-4357/aab78f.

D. R. Patton, R. G. Carlberg, R. O. Marzke, C. J. Pritchet, L. N. da Costa, and P. S. Pellegrini. New Techniques for Relating Dynamically Close Galaxy Pairs to Merger and Accretion Rates: Application to the Second Southern Sky Redshift Survey. *ApJ*, 536(1): 153–172, June 2000. doi: 10.1086/308907.

D. R. Patton, C. J. Pritchet, R. G. Carlberg, R. O. Marzke, H. K. C. Yee, P. B. Hall, H. Lin, S. L. Morris, M. Sawicki, C. W. Shepherd, and G. D. Wirth. Dynamically Close Galaxy Pairs and Merger Rate Evolution in the CNOC2 Redshift Survey. *ApJ*, 565(1):208–222, Jan. 2002. doi: 10.1086/324543.

D. R. Patton, S. L. Ellison, L. Simard, A. W. McConnachie, and J. T. Mendel. Galaxy pairs in the Sloan Digital Sky Survey - III. Evidence of induced star formation from optical colours. *MNRAS*, 412(1):591–606, Mar. 2011. doi: 10.1111/j.1365-2966.2010.17932.x.

D. R. Patton, P. Torrey, S. L. Ellison, J. T. Mendel, and J. M. Scudder. Galaxy pairs in the Sloan Digital Sky Survey - VI. The orbital extent of enhanced star formation in interacting galaxies. *MNRAS*, 433(1):L59–l63, June 2013. doi: 10.1093/mnrasl/slt058.

D. R. Patton, F. D. Qamar, S. L. Ellison, A. F. L. Bluck, L. Simard, J. T. Mendel, J. Moreno, and P. Torrey. Galaxy pairs in the Sloan Digital Sky Survey - XI. A new method for measuring the influence of the closest companion out to wide separations. *MNRAS*, 461(3): 2589–2604, Sept. 2016. doi: 10.1093/mnras/stw1494.

D. R. Patton, K. D. Wilson, C. J. Metrow, S. L. Ellison, P. Torrey, W. Brown, M. H. Hani, S. McAlpine, J. Moreno, and J. Woo. Interacting galaxies in the IllustrisTNG simulations - I: Triggered star formation in a cosmological context. *MNRAS*, 494(4):4969–4985, June 2020. doi: 10.1093/mnras/staa913.

D. R. Patton, L. Faria, M. H. Hani, P. Torrey, S. L. Ellison, S. D. Thakur, and R. I. Westlake. Interacting galaxies in the IllustrisTNG simulations - VI: Reconstructed orbits, close encounters, and mergers. *MNRAS*, 529(2):1493–1506, Apr. 2024. doi: 10.1093/mnras/stae608.

S. Paudel, R. Smith, S. J. Yoon, P. Calderón-Castillo, and P.-A. Duc. A Catalog of Merging Dwarf Galaxies in the Local Universe. *ApJS*, 237(2):36, Aug. 2018. doi: 10.3847/1538-4365/aad555.

J. Peñarrubia and A. Fattahi. What galaxy masses perturb the local cosmic expansion? *MNRAS*, 468(2):1300–1316, June 2017. doi: 10.1093/mnras/stx323.

J. Peñarrubia, Y.-Z. Ma, M. G. Walker, and A. McConnachie. A dynamical model of the local cosmic expansion. *MNRAS*, 443(3):2204–2222, Sept. 2014. doi: 10.1093/mnras/stu879.

J. Peñarrubia, F. A. Gómez, G. Besla, D. Erkal, and Y.-Z. Ma. A timing constraint on the (total) mass of the Large Magellanic Cloud. *MNRAS*, 456(1):L54–l58, Feb. 2016. doi: 10.1093/mnrasl/slv160.

S. Pearson, G. Besla, M. E. Putman, K. A. Lutz, X. Fernández, S. Stierwalt, D. R. Patton, J. Kim, N. Kallivayalil, K. Johnson, and E.-C. Sung. Local Volume TiNy Titans: gaseous dwarf-dwarf interactions in the Local Universe. *MNRAS*, 459(2):1827–1846, June 2016. doi: 10.1093/mnras/stw757.

S. Pearson, G. C. Privon, G. Besla, M. E. Putman, D. Martínez-Delgado, K. V. Johnston, R. J. Gabany, D. R. Patton, and N. Kallivayalil. Modelling the baryon cycle in low-mass galaxy encounters: the case of NGC 4490 and NGC 4485. *MNRAS*, 480(3):3069–3090, Nov. 2018. doi: 10.1093/mnras/sty2052.

P. J. E. Peebles. Dynamics of the Local Group: the Dwarf Galaxies. *arXiv e-prints*, art. arXiv:1705.10683, May 2017.

M. S. Petersen and J. Peñarrubia. Reflex motion in the Milky Way stellar halo resulting from the Large Magellanic Cloud infall. *MNRAS*, 494(1):L11–l16, May 2020. doi: 10.1093/mnrasl/slaa029.

M. S. Petersen and J. Peñarrubia. Detection of the Milky Way reflex motion due to the Large Magellanic Cloud infall. *Nature Astronomy*, 5:251–255, Jan. 2021. doi: 10.1038/s41550-020-01254-3.

A. Pillepich, D. Nelson, L. Hernquist, V. Springel, R. Pakmor, P. Torrey, R. Weinberger, S. Genel, J. P. Naiman, F. Marinacci, and M. Vogelsberger. First results from the IllustrisTNG simulations: the stellar mass content of groups and clusters of galaxies. *MNRAS*, 475(1):648–675, Mar. 2018a. doi: 10.1093/mnras/stx3112.

A. Pillepich, V. Springel, D. Nelson, S. Genel, J. Naiman, R. Pakmor, L. Hernquist, P. Torrey, M. Vogelsberger, R. Weinberger, and F. Marinacci. Simulating galaxy formation with the IllustrisTNG model. *MNRAS*, 473(3):4077–4106, Jan. 2018b. doi: 10.1093/mnras/stx2656.

A. Pillepich, D. Nelson, V. Springel, R. Pakmor, P. Torrey, R. Weinberger, M. Vogelsberger, F. Marinacci, S. Genel, A. van der Wel, and L. Hernquist. First results from the TNG50 simulation: the evolution of stellar and gaseous discs across cosmic time. *MNRAS*, 490(3):3196–3233, Dec. 2019. doi: 10.1093/mnras/stz2338.

A. Pillepich, D. Sotillo-Ramos, R. Ramesh, D. Nelson, C. Engler, V. Rodriguez-Gomez, M. Fournier, M. Donnari, V. Springel, and L. Hernquist. Milky Way and Andromeda analogs from the TNG50 simulation. *arXiv e-prints*, art. arXiv:2303.16217, Mar. 2023. doi: 10.48550/arXiv.2303.16217.

Planck Collaboration, P. A. R. Ade, N. Aghanim, M. Arnaud, M. Ashdown, J. Aumont, C. Baccigalupi, A. J. Banday, R. B. Barreiro, J. G. Bartlett, N. Bartolo, E. Battaner, R. Battye, K. Benabed, A. Benoît, A. Benoit-Lévy, J. P. Bernard, M. Bersanelli, P. Bielewicz, J. J. Bock, A. Bonaldi, L. Bonavera, J. R. Bond, J. Borrill, F. R. Bouchet, F. Boulanger, M. Bucher, C. Burigana, R. C. Butler, E. Calabrese, J. F. Cardoso, A. Catalano, A. Challinor, A. Chamballu, R. R. Chary, H. C. Chiang, J. Chluba, P. R. Christensen, S. Church, D. L. Clements, S. Colombi, L. P. L. Colombo, C. Combet, A. Coulais, B. P. Crill, A. Curto, F. Cuttaia, L. Danese, R. D. Davies, R. J. Davis, P. de Bernardis, A. de Rosa, G. de Zotti, J. Delabrouille, F. X. Désert, E. Di Valentino, C. Dickinson, J. M. Diego, K. Dolag, H. Dole, S. Donzelli, O. Doré, M. Douspis, A. Ducout, J. Dunkley, X. Dupac, G. Efstathiou, F. Elsner, T. A. Enßlin, H. K. Eriksen, M. Farhang, J. Fergusson, F. Finelli, O. Forni, M. Frailis, A. A. Fraisse, E. Franceschi, A. Frejsel, S. Galeotta, S. Galli, K. Ganga, C. Gauthier, M. Gerbino, T. Ghosh, M. Giard, Y. Giraud-Héraud, E. Giusarma, E. Gjerløw, J. González-Nuevo, K. M. Górski, S. Gratton, A. Gregorio, A. Gruppuso, J. E. Gudmundsson, J. Hamann, F. K. Hansen, D. Hanson, D. L. Harrison, G. Helou, S. Henrot-Versillé, C. Hernández-Monteagudo, D. Herranz, S. R. Hildebrandt, E. Hivon, M. Hobson, W. A. Holmes, A. Hornstrup, W. Hovest, Z. Huang, K. M. Huffenberger, G. Hurier, A. H. Jaffe, T. R. Jaffe, W. C. Jones, M. Juvela, E. Keihänen, R. Keskitalo, T. S. Kisner, R. Kneissl, J. Knoche, L. Knox, M. Kunz, H. Kurki-Suonio, G. Lagache, A. Lähteenmäki, J. M. Lamarre, A. Lasenby, M. Lattanzi, C. R. Lawrence, J. P. Leahy, R. Leonardi, J. Lesgourgues, F. Levrier, A. Lewis, M. Liguori, P. B. Lilje, M. Linden-Vørnle, M. López-Caniego, P. M. Lubin, J. F. Macías-Pérez, G. Maggio, D. Maino, N. Mandolesi, A. Mangilli, A. Marchini, M. Maris, P. G. Martin, M. Martinelli, E. Martínez-González, S. Masi, S. Matarrese, P. McGehee, P. R. Meinhold, A. Melchiorri, J. B. Melin, L. Mendes, A. Mennella, M. Migliaccio, M. Millea, S. Mitra, M. A. Miville-Deschênes, A. Moneti, L. Montier, G. Morgante, D. Mortlock, A. Moss, D. Munshi, J. A. Murphy, P. Naselsky, F. Nati, P. Natoli, C. B. Netterfield, H. U. Nørgaard-Nielsen, F. Noviello, D. Novikov, I. Novikov, C. A. Oxborrow, F. Paci, L. Pagano, F. Pajot, R. Paladini, D. Paoletti, B. Partridge, F. Pasian, G. Patanchon, T. J. Pearson, O. Perdereau, L. Perotto, F. Perrotta, V. Pettorino, F. Piacentini, M. Piat, E. Pierpaoli, D. Pietrobon, S. Plaszczynski, E. Pointecouteau, G. Polenta, L. Popa, G. W. Pratt, G. Prézeau, S. Prunet, J. L. Puget, J. P. Rachen, W. T. Reach, R. Rebolo, M. Reinecke, M. Remazeilles, C. Renault, A. Renzi, I. Ristorcelli, G. Rocha, C. Rosset, M. Rossetti, G. Roudier, B. Rouillé d'Orfeuil, M. Rowan-Robinson, J. A. Rubiño-Martín, B. Rusholme, N. Said, V. Salvatelli, L. Salvati, M. Sandri, D. Santos, M. Savelainen, G. Savini, D. Scott, M. D. Seiffert, P. Serra, E. P. S. Shellard, L. D. Spencer, M. Spinelli, V. Stolyarov, R. Stompor, R. Sudiwala, R. Sunyaev, D. Sutton, A. S. Suur-Uski, J. F. Sygnet, J. A. Tauber, L. Terenzi, L. Toffolatti, M. Tomasi, M. Tristram, T. Trombetti, M. Tucci, J. Tuovinen, M. Türler, G. Umana, L. Valenziano, J. Valiviita, F. Van Tent, P. Vielva, F. Villa, L. A. Wade, B. D. Wandelt, I. K. Wehus, M. White, S. D. M. White, A. Wilkinson, D. Yvon, A. Zacchei, and A. Zonca. Planck 2015 results. XIII. Cosmological

parameters. *A&A*, 594:A13, Sept. 2016. doi: 10.1051/0004-6361/201525830.

Planck Collaboration, N. Aghanim, Y. Akrami, M. Ashdown, J. Aumont, C. Baccigalupi, M. Ballardini, A. J. Banday, R. B. Barreiro, N. Bartolo, S. Basak, R. Battye, K. Benabed, J. P. Bernard, M. Bersanelli, P. Bielewicz, J. J. Bock, J. R. Bond, J. Borrill, F. R. Bouchet, F. Boulanger, M. Bucher, C. Burigana, R. C. Butler, E. Calabrese, J. F. Cardoso, J. Carron, A. Challinor, H. C. Chiang, J. Chluba, L. P. L. Colombo, C. Combet, D. Contreras, B. P. Crill, F. Cuttaia, P. de Bernardis, G. de Zotti, J. Delabrouille, J. M. Delouis, E. Di Valentino, J. M. Diego, O. Doré, M. Douspis, A. Ducout, X. Dupac, S. Dusini, G. Efstathiou, F. Elsner, T. A. Enßlin, H. K. Eriksen, Y. Fantaye, M. Farhang, J. Fergusson, R. Fernandez-Cobos, F. Finelli, F. Forastieri, M. Frailis, A. A. Fraisse, E. Franceschi, A. Frolov, S. Galeotta, S. Galli, K. Ganga, R. T. Génova-Santos, M. Gerbino, T. Ghosh, J. González-Nuevo, K. M. Górski, S. Gratton, A. Gruppuso, J. E. Gudmundsson, J. Hamann, W. Handley, F. K. Hansen, D. Herranz, S. R. Hildebrandt, E. Hivon, Z. Huang, A. H. Jaffe, W. C. Jones, A. Karakci, E. Keihänen, R. Keskitalo, K. Kiiveri, J. Kim, T. S. Kisner, L. Knox, N. Krachmalnicoff, M. Kunz, H. Kurki-Suonio, G. Lagache, J. M. Lamarre, A. Lasenby, M. Lattanzi, C. R. Lawrence, M. Le Jeune, P. Lemos, J. Lesgourgues, F. Levrier, A. Lewis, M. Liguori, P. B. Lilje, M. Lilley, V. Lindholm, M. López-Caniego, P. M. Lubin, Y. Z. Ma, J. F. Macías-Pérez, G. Maggio, D. Maino, N. Mandolesi, A. Mangilli, A. Marcos-Caballero, M. Maris, P. G. Martin, M. Martinelli, E. Martínez-González, S. Matarrese, N. Mauri, J. D. McEwen, P. R. Meinhold, A. Melchiorri, A. Mennella, M. Migliaccio, M. Millea, S. Mitra, M. A. Miville-Deschênes, D. Molinari, L. Montier, G. Morgante, A. Moss, P. Natoli, H. U. Nørgaard-Nielsen, L. Pagano, D. Paoletti, B. Partridge, G. Patanchon, H. V. Peiris, F. Perrotta, V. Pettorino, F. Piacentini, L. Polastri, G. Polenta, J. L. Puget, J. P. Rachen, M. Reinecke, M. Remazeilles, A. Renzi, G. Rocha, C. Rosset, G. Roudier, J. A. Rubiño-Martín, B. Ruiz-Granados, L. Salvati, M. Sandri, M. Savelainen, D. Scott, E. P. S. Shellard, C. Sirignano, G. Sirri, L. D. Spencer, R. Sunyaev, A. S. Suur-Uski, J. A. Tauber, D. Tavagnacco, M. Tenti, L. Toffolatti, M. Tomasi, T. Trombetti, L. Valenziano, J. Valiviita, B. Van Tent, L. Vibert, P. Vielva, F. Villa, N. Vittorio, B. D. Wandelt, I. K. Wehus, M. White, S. D. M. White, A. Zacchei, and A. Zonca. Planck 2018 results. VI. Cosmological parameters. *A&A*, 641:A6, Sept. 2020. doi: 10.1051/0004-6361/201833910.

G. C. Privon, S. Stierwalt, D. R. Patton, G. Besla, S. Pearson, M. Putman, K. E. Johnson, N. Kallivayalil, S. Liss, and T. Titans. A Widespread, Clumpy Starburst in the Isolated Ongoing Dwarf Galaxy Merger dm1647+21. *ApJ*, 846(1):74, Sept. 2017. doi: 10.3847/1538-4357/aa8560.

M. E. Putman, Y. Zheng, A. M. Price-Whelan, J. Grcevich, A. C. Johnson, E. Tollerud, and J. E. G. Peek. The Gas Content and Stripping of Local Group Dwarf Galaxies. *ApJ*, 913(1):53, May 2021. doi: 10.3847/1538-4357/abe391.

C. Ramos Almeida, C. N. Tadhunter, K. J. Inskip, R. Morganti, J. Holt, and D. Dicken. The optical morphologies of the 2 Jy sample of radio galaxies: evidence for galaxy interactions. *MNRAS*, 410(3):1550–1576, Jan. 2011. doi: 10.1111/j.1365-2966.2010.17542.x.

B. Robertson, M. Dickinson, H. C. Ferguson, S. Finkelstein, S. Furlanetto, P. Dayal, J. Greene, A. Hutter, P. Madau, D. Marrone, J. E. Rhoades, J. Rhodes, A. Shapley, D. Stark,

R. Wechsler, and E. Zackrisson. Understanding Galaxy Formation via Near-Infrared Surveys in the 2020s. *BAAS*, 51(3):30, May 2019a.

B. E. Robertson, M. Banerji, S. Brough, R. L. Davies, H. C. Ferguson, R. Hausen, S. Kaviraj, J. A. Newman, S. J. Schmidt, J. A. Tyson, and R. H. Wechsler. Galaxy formation and evolution science in the era of the Large Synoptic Survey Telescope. *Nature Reviews Physics*, 1(7):450–462, June 2019b. doi: 10.1038/s42254-019-0067-x.

A. S. G. Robotham, I. K. Baldry, J. Bland-Hawthorn, S. P. Driver, J. Loveday, P. Norberg, A. E. Bauer, K. Bekki, S. Brough, M. Brown, A. Graham, A. M. Hopkins, S. Phillipps, C. Power, A. Sansom, and L. Staveley-Smith. Galaxy And Mass Assembly (GAMA): in search of Milky Way Magellanic Cloud analogues. *MNRAS*, 424:1448–1453, Aug. 2012. doi: 10.1111/j.1365-2966.2012.21332.x.

V. Rodriguez-Gomez, S. Genel, M. Vogelsberger, D. Sijacki, A. Pillepich, L. V. Sales, P. Torrey, G. Snyder, D. Nelson, V. Springel, C.-P. Ma, and L. Hernquist. The merger rate of galaxies in the Illustris simulation: a comparison with observations and semi-empirical models. *MNRAS*, 449:49–64, May 2015. doi: 10.1093/mnras/stv264.

V. Rodriguez-Gomez, L. V. Sales, S. Genel, A. Pillepich, J. Zjupa, D. Nelson, B. Griffen, P. Torrey, G. F. Snyder, M. Vogelsberger, V. Springel, C.-P. Ma, and L. Hernquist. The role of mergers and halo spin in shaping galaxy morphology. *MNRAS*, 467(3):3083–3098, May 2017. doi: 10.1093/mnras/stx305.

V. Rodriguez-Gomez, G. F. Snyder, J. M. Lotz, D. Nelson, A. Pillepich, V. Springel, S. Genel, R. Weinberger, S. Tacchella, R. Pakmor, P. Torrey, F. Marinacci, M. Vogelsberger, L. Hernquist, and D. A. Thilker. The optical morphologies of galaxies in the IllustrisTNG simulation: a comparison to Pan-STARRS observations. *MNRAS*, 483(3):4140–4159, Mar. 2019. doi: 10.1093/mnras/sty3345.

L. V. Sales, W. Wang, S. D. M. White, and J. F. Navarro. Satellites and haloes of dwarf galaxies. *MNRAS*, 428(1):573–578, Jan. 2013. doi: 10.1093/mnras/sts054.

J. B. Salomon, R. Ibata, C. Reylé, B. Famaey, N. I. Libeskind, A. W. McConnachie, and Y. Hoffman. The proper motion of Andromeda from Gaia EDR3: confirming a nearly radial orbit. *MNRAS*, 507(2):2592–2601, Oct. 2021. doi: 10.1093/mnras/stab2253.

J. Salvatier, T. V. Wieckiâ, and C. Fonnesbeck. PyMC3: Python probabilistic programming framework, Oct. 2016.

S. Satyapal, S. L. Ellison, W. McAlpine, R. C. Hickox, D. R. Patton, and J. T. Mendel. Galaxy pairs in the Sloan Digital Sky Survey - IX. Merger-induced AGN activity as traced by the Wide-field Infrared Survey Explorer. *MNRAS*, 441(2):1297–1304, June 2014. doi: 10.1093/mnras/stu650.

T. Sawala, S. McAlpine, J. Jasche, G. Lavaux, A. Jenkins, P. H. Johansson, and C. S. Frenk. The SIBELIUS Project: E Pluribus Unum. *MNRAS*, 509(1):1432–1446, Jan. 2022. doi: 10.1093/mnras/stab2684.

R. Schönrich, J. Binney, and W. Dehnen. Local kinematics and the local standard of rest. *MNRAS*, 403(4):1829–1833, Apr. 2010. doi: 10.1111/j.1365-2966.2010.16253.x.

N. Shipp, T. S. Li, A. B. Pace, D. Erkal, A. Drlica-Wagner, B. Yanny, V. Belokurov, W. Wester, S. E. Koposov, K. Kuehn, G. F. Lewis, J. D. Simpson, Z. Wan, D. B. Zucker, S. L. Martell, M. Y. Wang, and S5 Collaboration. Proper Motions of Stellar Streams Discovered in the Dark Energy Survey. *ApJ*, 885(1):3, Nov. 2019. doi: 10.3847/1538-4357/ab44bf.

N. Shipp, D. Erkal, A. Drlica-Wagner, T. S. Li, A. B. Pace, S. E. Koposov, L. R. Cullinane, G. S. Da Costa, A. P. Ji, K. Kuehn, G. F. Lewis, D. Mackey, J. D. Simpson, Z. Wan, D. B. Zucker, J. Bland-Hawthorn, P. S. Ferguson, S. Lilleengen, and S. Lilleengen. Measuring the Mass of the Large Magellanic Cloud with Stellar Streams Observed by S ^{5}. *ApJ*, 923 (2):149, Dec. 2021. doi: 10.3847/1538-4357/ac2e93.

J. Sick, S. Courteau, J.-C. Cuillandre, J. Dalcanton, R. de Jong, M. McDonald, D. Simard, and R. B. Tully. The Stellar Mass of M31 as inferred by the Andromeda Optical & Infrared Disk Survey. In M. Cappellari and S. Courteau, editors, *Galaxy Masses as Constraints of Formation Models*, volume 311, pages 82–85, Apr. 2015. doi: 10.1017/S1743921315003440.

D. Sijacki, M. Vogelsberger, S. Genel, V. Springel, P. Torrey, G. F. Snyder, D. Nelson, and L. Hernquist. The Illustris simulation: the evolving population of black holes across cosmic time. *MNRAS*, 452(1):575–596, Sept. 2015. doi: 10.1093/mnras/stv1340.

G. F. Snyder, J. M. Lotz, V. Rodriguez-Gomez, R. d. S. Guimarães, P. Torrey, and L. Hernquist. Massive close pairs measure rapid galaxy assembly in mergers at high redshift. *MNRAS*, 468(1):207–216, June 2017. doi: 10.1093/mnras/stx487.

G. F. Snyder, V. Rodriguez-Gomez, J. M. Lotz, P. Torrey, A. C. N. Quirk, L. Hernquist, M. Vogelsberger, and P. E. Freeman. Automated distant galaxy merger classifications from Space Telescope images using the Illustris simulation. *MNRAS*, 486(3):3702–3720, July 2019. doi: 10.1093/mnras/stz1059.

G. F. Snyder, T. Peña, L. Y. A. Yung, C. Rose, J. Kartaltepe, and H. Ferguson. Mock galaxy surveys for HST and JWST from the IllustrisTNG simulations. *MNRAS*, 518(4):6318–6324, Feb. 2023. doi: 10.1093/mnras/stac3397.

S. T. Sohn, J. Anderson, and R. P. van der Marel. The M31 Velocity Vector. I. Hubble Space Telescope Proper-motion Measurements. *ApJ*, 753(1):7, July 2012. doi: 10.1088/0004-637x/753/1/7.

S. T. Sohn, E. Patel, G. Besla, R. P. van der Marel, J. S. Bullock, L. E. Strigari, G. van de Ven, M. G. Walker, and A. Bellini. Space Motions of the Dwarf Spheroidal Galaxies Draco and Sculptor Based on HST Proper Motions with a ~10 yr Time Baseline. *ApJ*, 849:93, Nov. 2017. doi: 10.3847/1538-4357/aa917b.

S. T. Sohn, E. Patel, M. A. Fardal, G. Besla, R. P. van der Marel, M. Geha, and P. Guhathakurta. HST Proper Motions of NGC 147 and NGC 185: Orbital Histories and Tests of a Dynamically Coherent Andromeda Satellite Plane. *ApJ*, 901(1):43, Sept. 2020. doi: 10.3847/1538-4357/abaf49.

D. Spergel, N. Gehrels, C. Baltay, D. Bennett, J. Breckinridge, M. Donahue, A. Dressler, B. S. Gaudi, T. Greene, O. Guyon, C. Hirata, J. Kalirai, N. J. Kasdin, B. Macintosh, W. Moos, S. Perlmutter, M. Postman, B. Rauscher, J. Rhodes, Y. Wang, D. Weinberg, D. Benford, M. Hudson, W. S. Jeong, Y. Mellier, W. Traub, T. Yamada, P. Capak, J. Colbert, D. Masters, M. Penny, D. Savransky, D. Stern, N. Zimmerman, R. Barry, L. Bartusek, K. Carpenter, E. Cheng, D. Content, F. Dekens, R. Demers, K. Grady, C. Jackson, G. Kuan, J. Kruk, M. Melton, B. Nemati, B. Parvin, I. Poberezhskiy, C. Peddie, J. Ruffa, J. K. Wallace, A. Whipple, E. Wollack, and F. Zhao. Wide-Field InfrarRed Survey Telescope-Astrophysics Focused Telescope Assets WFIRST-AFTA 2015 Report. *arXiv e-prints*, art. arXiv:1503.03757, Mar. 2015. doi: 10.48550/arXiv.1503.03757.

V. Springel. E pur si muove: Galilean-invariant cosmological hydrodynamical simulations on a moving mesh. *MNRAS*, 401:791–851, Jan. 2010. doi: 10.1111/j.1365-2966.2009.15715.x.

V. Springel, S. D. M. White, G. Tormen, and G. Kauffmann. Populating a cluster of galaxies - I. Results at [formmu2]z=0. *MNRAS*, 328:726–750, Dec. 2001a. doi: 10.1046/j.1365-8711.2001.04912.x.

V. Springel, N. Yoshida, and S. D. M. White. GADGET: a code for collisionless and gasdynamical cosmological simulations. *New Astron.*, 6:79–117, Apr. 2001b. doi: 10.1016/s1384-1076(01)00042-2.

V. Springel, R. Pakmor, A. Pillepich, R. Weinberger, D. Nelson, L. Hernquist, M. Vogelsberger, S. Genel, P. Torrey, F. Marinacci, and J. Naiman. First results from the IllustrisTNG simulations: matter and galaxy clustering. *MNRAS*, 475(1):676–698, Mar. 2018. doi: 10.1093/mnras/stx3304.

K. R. Stewart, J. S. Bullock, E. J. Barton, and R. H. Wechsler. Galaxy Mergers and Dark Matter Halo Mergers in ΛCDM: Mass, Redshift, and Mass-Ratio Dependence. *ApJ*, 702 (2):1005–1015, Sept. 2009. doi: 10.1088/0004-637x/702/2/1005.

S. Stierwalt, G. Besla, D. Patton, K. Johnson, N. Kallivayalil, M. Putman, G. Privon, and G. Ross. TiNy Titans: The Role of Dwarf-Dwarf Interactions in Low-mass Galaxy Evolution. *ApJ*, 805(1):2, May 2015. doi: 10.1088/0004-637x/805/1/2.

A. Tamm, E. Tempel, P. Tenjes, O. Tihhonova, and T. Tuvikene. Stellar mass map and dark matter distribution in M 31. *A&A*, 546:A4, Oct. 2012. doi: 10.1051/0004-6361/201220065.

G. Theureau, M. O. Hanski, N. Coudreau, N. Hallet, and J. M. Martin. Kinematics of the Local Universe. XIII. 21-cm line measurements of 452 galaxies with the Nançay radiotelescope, JHK Tully-Fisher relation, and preliminary maps of the peculiar velocity field. *A&A*, 465(1):71–85, Apr. 2007. doi: 10.1051/0004-6361:20066187.

E. J. Tollerud, M. Boylan-Kolchin, E. J. Barton, J. S. Bullock, and C. Q. Trinh. Small-scale Structure in the Sloan Digital Sky Survey and ΛCDM: Isolated ~L $_*$ Galaxies with Bright Satellites. *ApJ*, 738:102, Sept. 2011. doi: 10.1088/0004-637x/738/1/102.

E. Tolstoy, V. Hill, and M. Tosi. Star-Formation Histories, Abundances, and Kinematics of Dwarf Galaxies in the Local Group. *ARA&A*, 47(1):371–425, Sept. 2009. doi: 10.1146/annurev-astro-082708-101650.

E. Treister, P. Natarajan, D. B. Sanders, C. M. Urry, K. Schawinski, and J. Kartaltepe. Major Galaxy Mergers and the Growth of Supermassive Black Holes in Quasars. *Science*, 328(5978):600, Apr. 2010. doi: 10.1126/science.1184246.

R. P. van der Marel and P. Guhathakurta. M31 Transverse Velocity and Local Group Mass from Satellite Kinematics. *ApJ*, 678(1):187-199, May 2008. doi: 10.1086/533430.

R. P. van der Marel, M. Fardal, G. Besla, R. L. Beaton, S. T. Sohn, J. Anderson, T. Brown, and P. Guhathakurta. The M31 Velocity Vector. II. Radial Orbit toward the Milky Way and Implied Local Group Mass. *ApJ*, 753(1):8, July 2012a. doi: 10.1088/0004-637x/753/1/8.

R. P. van der Marel, G. Besla, T. J. Cox, S. T. Sohn, and J. Anderson. The M31 Velocity Vector. III. Future Milky Way M31-M33 Orbital Evolution, Merging, and Fate of the Sun. *ApJ*, 753:9, July 2012b. doi: 10.1088/0004-637x/753/1/9.

R. P. van der Marel, M. A. Fardal, S. T. Sohn, E. Patel, G. Besla, A. del Pino, J. Sahlmann, and L. L. Watkins. First Gaia Dynamics of the Andromeda System: DR2 Proper Motions, Orbits, and Rotation of M31 and M33. *ApJ*, 872(1):24, Feb. 2019. doi: 10.3847/1538-4357/ab001b.

E. Ventou, T. Contini, N. Bouché, B. Epinat, J. Brinchmann, H. Inami, J. Richard, I. Schroetter, G. Soucail, M. Steinmetz, and P. M. Weilbacher. New criteria for the selection of galaxy close pairs from cosmological simulations: evolution of the major and minor merger fraction in MUSE deep fields. *A&A*, 631:A87, Nov. 2019. doi: 10.1051/0004-6361/201935597.

C. Vera-Ciro and A. Helmi. Constraints on the Shape of the Milky Way Dark Matter Halo from the Sagittarius Stream. *ApJ*, 773(1):L4, Aug. 2013. doi: 10.1088/2041-8205/773/1/L4.

P. Villanueva-Domingo, F. Villaescusa-Navarro, S. Genel, D. Anglés-Alcázar, L. Hernquist, F. Marinacci, D. N. Spergel, M. Vogelsberger, and D. Narayanan. Weighing the Milky Way and Andromeda with Artificial Intelligence. *arXiv e-prints*, art. arXiv:2111.14874, Nov. 2021.

M. Vogelsberger, S. Genel, V. Springel, P. Torrey, D. Sijacki, D. Xu, G. Snyder, S. Bird, D. Nelson, and L. Hernquist. Properties of galaxies reproduced by a hydrodynamic simulation. *Nature*, 509:177–182, May 2014a. doi: 10.1038/nature13316.

M. Vogelsberger, S. Genel, V. Springel, P. Torrey, D. Sijacki, D. Xu, G. Snyder, D. Nelson, and L. Hernquist. Introducing the Illustris Project: simulating the coevolution of dark and visible matter in the Universe. *MNRAS*, 444:1518–1547, Oct. 2014b. doi: 10.1093/mnras/stu1536.

J. Wang, F. Hammer, and Y. Yang. Milky Way total mass derived by rotation curve and globular cluster kinematics from Gaia EDR3. *MNRAS*, 510(2):2242–2260, Feb. 2022. doi: 10.1093/mnras/stab3258.

L. Wang, W. J. Pearson, and V. Rodriguez-Gomez. Towards a consistent framework of comparing galaxy mergers in observations and simulations. *A&A*, 644:A87, Dec. 2020. doi: 10.1051/0004-6361/202038084.

J. T. Warfield, N. Kallivayalil, P. Zivick, T. Fritz, H. Richstein, S. T. Sohn, A. del Pino, A. Savino, and D. R. Weisz. HUBPUG: proper motions for local group dwarfs observed with HST utilizing Gaia as a reference frame. *MNRAS*, 519(1):1189–1200, Feb. 2023. doi: 10.1093/mnras/stac3647.

L. L. Watkins, N. W. Evans, and J. H. An. The masses of the Milky Way and Andromeda galaxies. *MNRAS*, 406(1):264–278, July 2010. ISSN 0035-8711. doi: 10.1111/j.1365-2966.2010.16708.x. URL https://doi.org/10.1111/j.1365-2966.2010.16708.x.

C. C. Williams, E. Curtis-Lake, K. N. Hainline, J. Chevallard, B. E. Robertson, S. Charlot, R. Endsley, D. P. Stark, C. N. A. Willmer, S. Alberts, R. Amorin, S. Arribas, S. Baum, A. Bunker, S. Carniani, S. Crandall, E. Egami, D. J. Eisenstein, P. Ferruit, B. Husemann, M. V. Maseda, R. Maiolino, T. D. Rawle, M. Rieke, R. Smit, S. Tacchella, and C. J. Willott. The JWST Extragalactic Mock Catalog: Modeling Galaxy Populations from the UV through the Near-IR over 13 Billion Years of Cosmic History. *ApJS*, 236(2):33, June 2018. doi: 10.3847/1538-4365/aabcbb.

S. Wuyts, N. M. Förster Schreiber, R. Genzel, Y. Guo, G. Barro, E. F. Bell, A. Dekel, S. M. Faber, H. C. Ferguson, M. Giavalisco, N. A. Grogin, N. P. Hathi, K.-H. Huang, D. D. Kocevski, A. M. Koekemoer, D. C. Koo, J. Lotz, D. Lutz, E. McGrath, J. A. Newman, D. Rosario, A. Saintonge, L. J. Tacconi, B. J. Weiner, and A. van der Wel. Smooth(er) Stellar Mass Maps in CANDELS: Constraints on the Longevity of Clumps in High-redshift Star-forming Galaxies. *ApJ*, 753(2):114, July 2012. doi: 10.1088/0004-637X/753/2/114.

S. Wuyts, N. M. Förster Schreiber, E. J. Nelson, P. G. van Dokkum, G. Brammer, Y.-Y. Chang, S. M. Faber, H. C. Ferguson, M. Franx, M. Fumagalli, R. Genzel, N. A. Grogin, D. D. Kocevski, A. M. Koekemoer, B. Lundgren, D. Lutz, E. J. McGrath, I. Momcheva, D. Rosario, R. E. Skelton, L. J. Tacconi, A. van der Wel, and K. E. Whitaker. A CANDELS-3D-HST synergy: Resolved Star Formation Patterns at 0.7 ¡ z ¡ 1.5. *ApJ*, 779(2):135, Dec. 2013. doi: 10.1088/0004-637x/779/2/135.

M. Zhai, Q. Guo, G. Zhao, Q. Gu, and A. Liu. Local Group Analogs in ΛCDM Cosmological Simulations. *ApJ*, 890(1):27, Feb. 2020. doi: 10.3847/1538-4357/ab6986.